A Structural Health Monitoring Concept on Ultrasonic Based Assessment of Aged Structures with Isotropic and Anisotropic Material Properties

Dissertation
zur Erlangung des Grades
des Doktors der Ingenieurwissenschaften
der Naturwissenschaftlich-Technischen Fakultät
der Universität des Saarlandes

von

Ramanan Sridaran Venkat

Saarbrücken
2018

Tag des Kolloquiums:	19.10.2018
Dekan:	Prof. Dr. rer. nat. Guido Kickelbick
Berichterstatter:	Prof. Dr.-Ing. Christian Boller
	Prof. Dr.-Ing. Claus-Peter Fritzen
Vorsitzender:	Prof. Dr.-Ing. Dirk Bähre
Akad. Mitarbeiter:	Dr. Hongyu Gao

Declaration

This dissertation is being submitted for the degree of Doctor of Engineering at Saarland university, Saarbrücken. I hereby declare that this thesis and the work reported herein was composed and originated entirely from me under the guidance of Professor Dr.-Ing Christian Boller, Chair of NDT and Quality Assurance (LZFPQ). The Information derived from the published and unpublished work of others has been acknowledged in the text and references are given in the list of sources.

Ramanan Sridaran Venkat,
Saarland University

Zusammenfassung

Ultraschall ist eine in der klassischen zerstörungsfreien Prüfung (ZfP) weit verbreitete Technik, bei der vielfältig Fortschritte hinsichtlich Signalverarbeitung, Auflösungsvermögen, Visualisierung und vermutlich weiterer Dinge erzielt wurden. Mit der Einführung des Phased Array sowie fortgeschrittener Rechner- und Signalverarbeitungstechnik ist auch die Charakterisierung anisotroper Werkstoffe erleichtert worden. Parallel dazu hat sich das Gebiet der Zustandsüberwachung (Structural Health Monitoring (SHM)) als Forschungsfeld entwickelt, dies im Hinblick auf die Automatisierung der ZfP und der erweiterten Nutzung des Potenzials der Schadenstoleranz bzw. des Leichtbaus von Bauteilen. Geführte Wellen auf der Basis des Ultraschalls sind im Bereich des SHM ein derzeit breit untersuchtes Forschungsfeld und es ist somit wert zu ermitteln, inwieweit sich auf geführte Wellen beziehende Techniken aus der ZfP auf SHM-Anwendungen übertragen werden können. Reverse Phase Matching (RPM) in Verbindung mit anisotropen Werkstoffeigenschaften und Ray Tracing sind eine in diesem Sinne interessante, sich fügende und verfolgungswerte Kombination, um möglicherweise über die Betrachtung inhärenter nicht-linearer Werkstoffantworten auf der Basis einer numerischen Simulation (FEM) ein optimales Sensornetzwerk für SHM zu bestimmen, womit das Potenzial eines Faserverbundwerkstoffs wie CFK besser genutzt werden kann. Ein hierzu gewählter Ansatz wird am Beispiel einer gealterten CFK-Struktur im Hinblick auf deren Schädigungszustand erläutert, für den dann diesbezüglich am Ende ein SHM-System konfiguriert werden kann. Abschließend wird eine Systematik vorgestellt, über die in der ZfP generiertes Wissen mit einem ‘SHM-Werkzeugkasten’ so verknüpft wird, dass längerfristig eine Weiterentwicklung von SHM-Systemen ermöglicht wird.

.

Abstract

Ultrasound is a technique widely applied in classical NDT where a lot of progress has been made in terms of signal processing, resolution, visualisation, and possibly more. With the introduction of the phased array technique, advanced computation and sensor signal processing also the characterisation of anisotropic materials has been facilitated. In parallel SHM has emerged as a field of research very much looking into the automation of NDT in view of taking enhanced advantage of an engineering structure's damage tolerance and hence light weight potential. Ultrasonic guided waves are a field very much explored currently within the context of SHM and as such it is worth to determine what of the guided wave related techniques developed in NDT may be inheritable for SHM applications. Reverse Phase Matching (RPM) referred to anisotropic material properties and ray tracing are an interesting combination to be pursued in terms of finding an optimum sensor configuration for SHM through numerical simulation based on FEM, allowing to take better advantage of a polymer based composite materials potential such as CFRP by taking advantage of those materials' inherent non-linear responses. The approach to be taken is illustrated with respect to an example, explaining on how to assess an ageing CFRP component in terms of its damage condition and an SHM system to be configured in the end. Finally a systematic is presented on how knowledge generated in NDT can be linked into a 'SHM-toolbox' to be used for the advancement of SHM systems to be developed in the longer term.

Acknowledgement

My foremost and earnest gratitude to my supervisor Prof. Dr.-Ing Christian Boller, head of the chair of non-destructive testing (LZfPQ), Saarland University for his supervision, guidance, and continuous motivation during and after my research periods. Being the director of our chair, it is not always easy to have a room for discussions and getting some feedbacks but instead most of the discussions happened more frequently and feedback e-mails in the wee hours have shown his determination towards his work, which eventually helped me to shape my thesis in an appropriate way. His vast experience in the fields of both Structural Health Monitoring (SHM) and NDT made me to realize that the results of the thesis would certainly play a major role in SHM of ageing composites in the coming future. I thank Prof. Dr.-Ing Claus-Peter Fritzen from University of Siegen for accepting to review my thesis.

I would like to express my sincere thanks to Dr.-Ing. Andrey Bulavinov, Saarbrücken for his valuable suggestions during initial stages of my thesis. I express my gratitude to Prof. Dr. Qiu Lei from the Nanjing University of Aeronautics and Astronautics (NUAA), Mr. Mirko Steckel from IMA (Dresden), and Prof. Dr. Roy Mahapatra from the Indian Institute of Science (IISc, Bengaluru) for providing experimental opportunities. I appreciate Mr. Soumendu Bagchi for the work and discussions regarding non-linear vibration problems. I express lot of thanks to my former colleague Prof. Dr.-Ing. Peter Starke for continuous motivation. It is important to mention a vote of thanks to my friend and well-wisher Dr. Vivek Rathod for valuable discussions in and out of the research. Besides, I thank Dr.-Ing. Sergey Pudovikov and Dr.-Ing. Meisam Sheikh Amiri for their support and encouragement. I appreciate Prof. Michael Kröning, Prof. Randolf Hanke, Mr. Reddy and Mr. Madhusudan for giving me an initial opportunity to interact with the Fraunhofer Institute of NDT (IZFP). I thank Mrs. Theiner, former secretary of Fraunhofer Institute of NDT (IZFP) and former department head and secretary Dr. Altpeter and Mrs. Bettinger for providing me a nice working environment at the Fraunhofer Institute.

It is a very important time to mention thanks to my family members especially my beloved wife Suganthi who has always been a great moral support. She made sure that I didn't lose any determination towards my goal. There is a great need for me to express thanks to my parents, elder brother and grandma for their prayers and support.

"*I dedicate this work to my beloved wife Suganthi, my little daughter Shria, my parents Mr. Sridaran, Mrs. Alamelu and my elder brother Gana. Finally, my Grandma who is not with me anymore*"

Contents

LIST OF FIGURES 10
LIST OF TABLES 15
LIST OF ABBREVIATIONS AND MEANINGS 16
Chapter 1
Introduction, Motivation and Objectives 19
1.1 Ageing of Structures 19
1.2 Ultrasonic Non-destructive Testing 23
1.3 Structural Health Monitoring (SHM) of Aircraft Structures 25
1.4 Uncertainties in Establishing a Health Monitoring Concept for Ageing Structures 27
1.4.1 Anisotropy 27
1.4.2 Probability of Detection 28
1.4.3 Damage Conditions of Ageing Structures 28
1.5 Role of SHM in Life Cycle Management 29
Chapter 2
Classical Acoustics and their Development 31
2.1 A few Fundamentals 31
2.2 Acoustic Wave Generation Including Phased Array 35
2.3 Ray Tracing 37
2.4 Synthetic Aperture Focussing Technique (SAFT) 39
2.5 Sampling Phased Array (SPA) or Full Matrix Capture (FMC) 44
2.5.1 The General Principle 44
2.5.2 Reconstruction for Isotropic Medium for SPA Data 46
2.5.3 Advantages of SPA 49
2.6 Fundamentals of Anisotropy and Determination of Elastic Constants in Anisotropic Media 49
2.6.1 Wave Propagation in Anisotropic Medium 49
2.6.2 Backwall Reflection Method 55
2.7 Reverse Phase Matching (RPM) 57
2.7.1 The Principle of RPM 57
2.7.2 Implementation of RPM for Transversely Isotropic Medium through Ray Tracing 58
2.8 Hardware 59

2.8.1 Hardware Platform 59
2.8.2 Measurement Procedure for SPA 61
2.9 Experimental Validation 62
Chapter 3
Non-linear Acoustics for Damage Assessment 65
3.1 Contact Acoustic Nonlinearity (CAN) 66
3.1.1 Central Frequency Shift 67
3.1.2 Higher Harmonic Generation 68
3.1.3 Waveform Distortions 70
3.2 VHCF Experimental Setup 72
3.3 Numerical Simulation of Composite Laminates Subjected to Three-Point Bending 76
3.4 Analysis of Experimental Data Using Signal Processing Methods 79
3.4.1 Fast Fourier Transformation (FFT) 79
3.4.2 Short Time Fourier Transformation (STFT) 81
3.4.3 Distortion Factor 82
3.4.4 Damage Index Measures 83
3.5 Analysis of Simulated and Experimental Results 85
3.6 Inverse Approach of Characterising Damages Using Simulation 87
Chapter 4
Guided Waves and their Relation to Structural Health Monitoring 89
4.1 Fundamentals of Guided Waves 89
4.2 Structural Health Monitoring Based on Guided Waves 92
4.3 Guided Waves in the Context of Structural Numerical Simulation 96
4.3.1 Generic Plate 96
4.3.2 Stiffened Panel 97
4.3.3 The Structural Simulation Process 98
4.3.4 Guided Wave Simulation Using FEM 103
4.3.5 Input Signal or Excitation Signal 107
4.3.6 Boundary Conditions 108
4.4 Numerical Simulation Results 108
4.4.1 Selection of Actuators and Sensors 108
4.4.2 Stress and Fatigue Analysis 109
4.4.3 Guided Wave Propagation 111
4.5 Differential Imaging as Means for Damage Information Monitoring 113
4.6 Experimental Validation of Simulation 123

Chapter 5
Configuration of a SHM Toolbox to Solve Structural Ageing Problems 127
5.1 SHM within the Structural Design Process 127
5.2 SHM Toolbox Using Acoustic Methods 129
5.3 Approach to Handle Ageing Composite Structures 133
5.3.1 Numerical Search for Material Characterisation (Steps 1 to 3) 134
5.3.2 Ray Tracing for Time Efficient Wave Simulation (Step 4) 138
5.3.3 Simulation of Structural Non-linear Behaviour (Steps 5 to 7) 138
5.3.4 Simulation of Structural Behaviour in Terms of Damage Tolerance and Guided Wave Propagation (Step 8) 139
5.3.5 Differential Imaging and Experimental Validation (Steps 9 and 10) 140
5.4 Guided Wave Dispersion Diagrams as an Alternative to Assess Ageing Structures 142
Chapter 6
Conclusion and Future Work 145
6.1 Conclusions 145
6.2 Future Work 146
Bibliography 149

LIST OF FIGURES

Figure 1.1 Separated wing of Grumman G73T aircraft (www.skybrary.aero) 21
Figure 1.2 Debris of Boeing 747-200 (www.skybrary.aero) 21
Figure 1.3 Reduction in residual strength due to ageing (Harris, 2003) 23
Figure 1.4 Reduction in stress wave factor due to ageing (Harris, 2003) 23
Figure 1.5 Phased array ultrasonic inspection of welds 24
Figure 1.6 Trade-off between detectable crack size and inspection interval 27
Figure 1.7 Life cycle of a structure 30

Figure 2.1 Snell's Law of reflection and transmission for a solid/solid interface at an oblique angle 32
Figure 2.2 Ultrasonic excitation signal 33
Figure 2.3 Formation of pulse from superposition of continuous wave forms (Bray & Stanley, 1996) 34
Figure 2.4 Methods of acoustic wave generation and reception a) Pulse-echo method; b) Pitch-catch method; and c) Through-transmission method 36
Figure 2.5 Phased array excitation and reception 37
Figure 2.6 Ray tracing in single layered media 38
Figure 2.7 Travel time distribution for isotropic and anisotropic medium for the center element of a phased array transducer 38
Figure 2.8 Flowchart for ray tracing in a two layered medium 39
Figure 2.9 Synthetic Aperture Focusing Technique (SAFT) principle 41
Figure 2.10 Data acquisition in SAFT 42
Figure 2.11 SAFT reconstruction for single element transducer 43
Figure 2.12 SAFT reconstruction for phased array transducer 43
Figure 2.13 Excitation and reception sequences in SPA 45
Figure 2.14 SAFT reconstruction for isotropic medium 47
Figure 2.15 Comparison of sector scan images of CPA and SPA (Bulavinov, 2008) 48
Figure 2.16 A-scan signal characteristics of CPA and SPA (Bulavinov, 2008) 48
Figure 2.17 Direction of wave vector and energy vector in uni-directional laminate 50

Figure 2.18 Representation of the slowness curve for Young's modulus in a unidirectional composite 51
Figure 2.19 Wave propagation in symmetry direction 52
Figure 2.20 Wave propagation in non-symmetry direction 52
Figure 2.21 Effect of anisotropy in wave propagation (Kriz & Liu, 2007) 52
Figure 2.22 Backwall reflection method for measuring velocities experimentally 56
Figure 2.23 Ray tracing between all the elements and sender 57
Figure 2.24 Implementation of Reverse Phase Matching method in SPA 59
Figure 2.25 SPA system (Bulavinov, et al., 2008) 59
Figure 2.26 Architecture of SPA system (Bulavinov, et al., 2008) 60
Figure 2.27 SPA electronics along with immersion tank and scanning systems 61
Figure 2.28 Time gain compensation curve 62
Figure 2.29 Test sample with location of flat bottom hole 63
Figure 2.30 Test sample with PA transducer 63
Figure 2.31 S- scan comparison on the same gain level for the CFRP Test sample of (a) SPA without anisotropic correction; (b) RPM; and (c) CPA 64

Figure 3.1 Closing and opening action of crack due to loading 67
Figure 3.2 Illustration of the nonlinear acoustic vibro-modulation 67
Figure 3.3 (a) Shift in fundamental frequency for the undamaged; and (b) Damaged CFRP- Nonlinear Elastic Wave Spectroscopy (Meo & Zumpano, 2005) 68
Figure 3.4 (a) Nonlinearity vs. thermal ageing; and (b) Nonlinearity vs. FATT (Frouin, Matikas, Na, & Sathish, 1999) 70
Figure 3.5 Classification of the damage features according to the information condensation 71
Figure 3.6 (a) Velocity response signals for pristine; and (b) Velocity response signals on damaged specimen (Ooijevaar, 2014.) 71
Figure 3.7 (a) Acceleration response signals on pristine; and (b) Acceleration response signals on damaged specimen (Ooijevaar, 2014.) 72
Figure 3.8 Three-point bending VHCF for CFRP (Backe, et al., 2012) 73
Figure 3.9 Temperature distribution during pulse-pause state during VHCF (Backe et al., 2012) 74

Figure 3.10 CFRP specimen used for non-linear analysis 74
Figure 3.11 CT image of pristine composite specimen analysed (Sridaran Venkat, Starke, & Boller, 2018) 75
Figure 3.12 Ultrasonic scans taken from the top and bottom side of the specimen (Sridaran Venkat, Starke, & Boller, 2018)..... 76
Figure 3.13 a) Model geometry and load conditions; and b) Meshed geometry from FEM simulation 76
Figure 3.14 FEM simulation (a) Original state; (b) Opening of the crack; and (c) Closing of the crack 78
Figure 3.15 (a) Time domain signals of experiment and simulation for undamaged; and (b) Time domain signals of experiment and simulation for damaged specimen..... 79
Figure 3.16 Frequency spectrum for a pristine condition of the experimental data at N=10^8 cycles 80
Figure 3.17 Comparison of the frequency spectrum for pristine and damaged condition of the experimental data..... 80
Figure 3.18 (a) STFT of 10^6 cycles; and (b) STFT of 10^8 cycles of experimental data 81
Figure 3.19 Distortion factor of the experimental data (Rabe, et al., 2012)..... 82
Figure 3.20 (a) Central frequency shift; (b) Energy coefficients of the frequency spectrum; (c) Correlation coefficient; (d) Differential harmonics of frequency spectrum; and (e) Total distortion factor of the time domain signal..... 84
Figure 3.21 Comparison of LDV and load sensor data for the damage index: (a) Equation 3.21 (b) Equation 3.22; and (c) Equation 3.23 85
Figure 3.22 Frequency spectrum for various crack sizes when the delamination is at the center of the specimen as shown in Fig. 3.13..... 86
Figure 3.23 Comparison of frequency spectra between simulation and experiment 86
Figure 3.24 (a) Curve fitting for various crack sizes at different positions using MATLAB; and (b) Surface plot for the size and location of the delamination 87
Figure 3.25 Damage quantification through inversion using simulation..... 88

Figure 4.1 Mode shapes of fundamental: (a) Symmetrical; and (b) Anti-symmetrical modes 90
Figure 4.2 Phase velocity dispersion curve for aluminum plate of 3 mm thickness 91

Figure 4.3 Group dispersion curve for aluminum plate of 3 mm thickness..... 91
Figure 4.4 Elements in active SHM 92
Figure 4.5 Elements in passive SHM 93
Figure 4.6 Pitch catch and pulse echo methods in acoustic based SHM..... 96
Figure 4.7 Generic plate for stress analysis and guided wave simulation..... 97
Figure 4.8 Stiffened panel for guided wave analysis 98
Figure 4.9 Sequence of simulation tools in SHM architecture 98
Figure 4.10 Global-local FEM approach using PWAS patches..... 101
Figure 4.11 CAFA approach..... 101
Figure 4.12 Various hybrid methods for ultrasonic NDE simulations 102
Figure 4.13 FEM process flow 103
Figure 4.14 Triangular elements with 3 and 6 nodes, rectangular elements with 4 and 8 nodes and box element with 8 and 20 nodes (Sheehan, 2016)..... 103
Figure 4.15 Displacement field in 2D for a plate geometry using COMSOL Multiphysics 106
Figure 4.16 Guided wave multi-physics model in COMSOL..... 107
Figure 4.17 Hanning window tone burst excitation 108
Figure 4.18 Stress simulations using: a) ANSYS FEM; and b) COMSOL Multiphyscis tools 110
Figure 4.19 Strain simulation using FEM: a) ANSYS; and b) COMSOL Multiphysics 110
Figure 4.20 Stiffened panel with crack and their corresponding: a) Stress concentration zones; and b) Probability of damage accumulation (Balajee Ravi, et al., 2016)..... 111
Figure 4.21 Guided wave propagation in the generic plate at various time intervals for the geometry having no crack and crack after: a) 30 μs; and b) 40 μs..... 111
Figure 4.22 Guided wave propagation in generic plate in three dimension 112
Figure 4.23 Guided wave propagation in stiffened panel having no stringers in the geometry after various time intervals from signal initiation: a) 30 μs, b) 45 μs, c) 65 μs; and d)105 μs..... 112
Figure 4.24 Windowing in damage detection algorithm (Malinowski, Wandowski, & Ostachowicz, 2012)..... 114
Figure 4.25 Differential images for the generic plate with a crack length of 15 mm at the central hole 118

Figure 4.26 Differential images for the generic plate of crack length 25 mm at the centre hole 118
Figure 4.27 Differential images for the generic plate of crack length 35 mm at the centre hole 118
Figure 4.28 Differential images for stiffened panel for a crack length of 51 mm starting at the middle rivet line at various times 119
Figure 4.29 Actuator and sensor positions on generic plate 119
Figure 4.30 Actuator and sensor positions in the simulated model for stiffened panel 120
Figure 4.31 Received signals at sensors a) S6 and; b) S10 of Fig. 4.29 120
Figure 4.32 Sensor signals for stiffened panel at a) S1 position and; b) S4 position of Fig. 4.30 120
Figure 4.33 Various sensor positions for the calculation of RMSD 121
Figure 4.34 RMSD for various sensor positions 122
Figure 4.35 Differential signal of sensor S6 for various crack sizes 122
Figure 4.36 a) Experimental setup; b) Comparison of simulation and experiment for sensor 6; and c) Comparison of simulation and experiment for sensor 10 124
Figure 4.37 a) Experimental setup; b) Specimen; and c) Crack cut at the panel 124
Figure 4.38 Sensors and actuator positions for calculating the correlation output on stiffened panel 125
Figure 4.39 Correlation output as a measure of damage index for various sensor positions (Balajee Ravi, et al., 2016) 125

Figure 5.1 Design process chain for structural assessment 127
Figure 5.2 SHM toolbox structure from its highest level 128
Figure 5.3 Relationship between SHM Toolbox and acoustic methods described in the thesis 130
Figure 5.4 Structure of SHM toolbox for acoustics based SHM system design 131
Figure 5.5 Options and techniques to be considered regarding sensor signal data handling 132
Figure 5.6 Integration of various NDT methods in the thesis 133
Figure 5.7 Flowchart of numerical search algorithm 136

Figure 5.8 Resultant images of the numerical search algorithm 137
Figure 5.9 Group angle versus velocity distribution for a 64-element PA transducer .. 138
Figure 5.10 a) Composite plate; and b) Elasticity matrix as obtained using iteration .. 139
Figure 5.11 Wave propagation in CFRP plate at various time steps for undamaged cases: a), b) and c); For the crack at the center d), e) and f) 140
Figure 5.12 Differential images at: a) 10 µs; b) 20 µs; and c) 40 µs 141
Figure 5.13 Received signals of sensor position S1 141
Figure 5.14 Received signals of sensor position S2 141
Figure 5.15 Differential signals: S1 (red) position and S2 (blue) position 142
Figure 5.16 Reduction of Young's modulus due to thermal ageing of aluminium (Rojas, 2011) 143
Figure 5.17 Difference in group velocities of dispersion diagrams due to ageing calculated using the CIVA-GWT module: a) Dispersion curve for reduced E-modulus; and b) Dispersion curve for actual Young's modulus (prior to ageing). 143

Figure 6.1 Combination of diagnostics and prognostics toolboxes 146

LIST OF TABLES

Table 2.1 Storing of velocities w.r.t. sender-receivers using backwall reflection 56
Table 2.2 Example for parameters to be calculated represented in vector form 58
Table 2.3 CFRP material properties 62
Table 2.4 Phased array transducer parameters 64

Table 4.1 Properties of piezoelectric materials 95
Table 4.2 Properties and dimensions of the generic plate 96
Table 4.3 Properties of the stiffened panel 97
Table 4.4 FEM parameters for guided wave simulation 106
Table 4.5 Piezoelectric properties for simulation 109

LIST OF ABBREVIATIONS AND MEANINGS

ABAQUS	Finite element analysis software
A-scan	1D time domain signal
AFGROW	Air Force Growth-tool for calculating fatigue crack growth
ANN	Artificial Neural Networks
CAD/CAE	Computer Aided Designing/ Computer Aided Engineering
CAFA	Combined Analytical Finite Element Approach
CAN	Contact Acoustic Non-linearity
CFRP	Carbon Fiber-Reinforced Polymer
CIVA	Name of NDE simulation tool
COMSOL	FEM based simulation tool
CT	Computed Tomography
CPA	Conventional Phased Array
EXTENDE	Name of the company that sells CIVA software
FEA	Finite Element Analysis
FEM	Finite Element Method
FFT	Fast Fourier Transformation
FMC	Full Matrix Capture
GECDM	Gradient Elastic Constants Descent Method
GFRP	Glass Fiber Reinforced Polymer
GW	Guided Waves
IN-DEUS	Integration of Non-destructive Evaluation based Ultrasonic Simulation
LDV	Laser Doppler Vibrometry
LUT	Look Up Table
MATLAB	Mathematical tool for computing

MSC-Fatigue	Simulation tool that performs fatigue damage calculation
NDE	Non-destructive Evaluation
NDT	Non-destructive Testing
PA	Phased Array
PAUT	Phased Array Ultrasonic Testing
POD	Probability of Detection
PPS	Polyphenylenesulfide
PWAS	Piezoelectric Wafer Acoustic Sensors
RMSD	Root Mean Square Standard Deviation
RPM	Reverse Phase Matching
RT-SFEM	Ray Tracing Spectral Finite Element Method
SAFE	Semi-Analytical Finite Element
SAFT	Synthetic Aperture Focusing Technique
S-scan	Image as a result from sectorial scanning in PAUT
SHM	Structural Health Monitoring
SLDV	Scanning Laser Doppler Vibrometry
SPA	Sampling Phased Array
STFT	Short Time Fourier Transformation
TFM	Total Focusing Method
TI	Transversely Isotropic medium
UT	Ultrasonic Testing
VHCF	Very High Cycle Fatigue
WFR	Wave Form Revealer

Chapter 1

Introduction, Motivation and Objectives

1.1 Ageing of Structures

Engineering structures made from metallic materials such as steel alloys, aluminium alloys etc., and composite materials such as Carbon Fiber-Reinforced Polymers (CFRP), Glass Fiber-Reinforced Polymers (GFRP) etc., which are used in various applications such as aerospace, wind energy, bridges and others undergo various ageing phenomena. Also civil infrastructures built using concrete undergo ageing. Ageing is either a slow or a rapid process of partial or total loss of the performance of the material properties to achieve the required function for which they were constructed. The performance and function of engineering structures are very much essential for public safety but ageing of the structures may adversely affect their ability to withstand the future operating conditions, extreme environmental challenges or accidents, and can increase the risk to public safety if not controlled. To manage the effects of ageing there are many developments in inspection/testing, and maintenance techniques to ensure continuous safety, functional, and economic operation of the structures. Damage tolerance and safe life design philosophies are applied and appropriate inspection methods and inspection intervals are developed to identify the effects of accidental, environmental or fatigue damage.

Specifically, in this thesis, problems related with ageing of aircraft structures are going to be discussed. The maintenance issues with respect to ageing aircraft structures generally arising either from fatigue or corrosion, with corrosion sometimes initiating fatigue effects in metallic structures. Metallic materials are being replaced with non-metallic composites in recent years. One of the main advantages of this is that their functional performance is not affected by the corrosive environment. Composites are materials resulting from the combination of two or more materials constituents with significantly different physical or chemical properties to produce a material with characteristics different from the individual material constituents. Carbon fiber reinforced polymers (CFRP) is a well-known composite material being a mixture of two phases; 1. fibers and 2. polymers. Fibers are known as the reinforcing phase made of carbon, aramid or glass etc., where

the properties of fibers are high strength, high stiffness and low density, whereas polymers are usually referred to as the matrix phase or continuous phase that helps to bind the fibers together and acts as a load bearing medium with its primary role to give a shape to the structure being usually brittle in nature. The main advantage of composite materials in general is that one can tailor their mechanical properties according to the service requirement. High strength to weight ratio of composite materials has led to the exponential growth in the usage of those materials in the aerospace industries, leading to weight and fuel consumption reduction which in turn has resulted in reducing operating costs. The aircraft manufacturer Boeing calculates that the high use of CFRP means that weight savings of more than 20% can be achieved when compared to more conventional aluminium designs (Onishi, 2012).

In 2013, Airbus achieved a milestone with their new aircraft A350 by using 50% of the structure made out of composites. Another important cause of ageing is structural fatigue, which results in cracks that propagate because the geometry of the crack produces a very high stress concentration at the ends. According to a report (www.skybrary.aero) fatigue cracks have been found to arise in three main ways; 1. in internal load-bearing airframe structural components which can develop stress 'hot spots'; 2. in load-bearing skins of large aircraft in which the skin itself carries a significant structural load; 3. from fastener holes where localised stress concentration can initiate premature cracking. In a study from (Goldman, 2002) published by the FAA it has been reported that 7.1% of general aviation accidents were related to maintenance problems and 13–27% out of these were fatal across the period spanning 1988–1997. Structural fatigue has produced several ageing aircraft losses in the past.

Investigations on various aircraft accidents help to understand the causes of failures. One such accident due to structural fatigue occurred on a 58-year old Grumman G73T Turbo Mallard plane. The investigation revealed that the right wing separated from the fuselage because of multiple pre-existing fatigue fractures, which reduced the residual strength of the wing structure. The separated wing is shown in Fig. 1.1. The airplane was crashed into a shipping channel near to the port of Miami, Florida. All 20 people who were onboard were killed in the accident. A similar incident occurred due to structural fatigue on 25th May 2002 where a China Airlines Boeing 747-200 broke up in mid-air over Penghu Island Taiwan. The structural failure was as a result of an improper repair carried out in

1980, which had not been detected by subsequent inspections. The debris of the airplane is shown in Fig. 1.2.

Figure 1.1 Separated wing of Grumman G73T aircraft (www.skybrary.aero)

Figure 1.2 Debris of Boeing 747-200 (www.skybrary.aero)

In 1985 in Gunma Japan, a Boeing 747 SR-100 experienced a loss of control and eventually crashed. The investigation report said that the aircraft's pressure bulkhead was damaged in 1978 and the repair was not performed according to the Boeing's approved repair method. As a result, the strength of the bulkhead was reduced and the unidentified fatigue cracks during the maintenance and inspection propagated at the spliced portion of the bulkhead's web to the extent that it became unable to endure the cabin pressure during flight and eventually ruptured. Many such failure investigations have been reported in the literature listed in (www.skybrary.aero).

It is essential to address questions regarding structural integrity and airworthiness for ageing aircraft structures. Most of the ageing studies in the past focussed on metallic

structures but with the increasing usage of composites as primary aircraft structures, the ageing problem should be studied in detail. Tomblin and Salah (Tomblin & Salah, 2010) studied the ageing effect of the horizontal stabiliser made of graphite-epoxy of a Boeing-737 after 18 years of service, which was equivalent to 48000 flight hours in the specific case. According to this paper (Tomblin & Salah, 2010), non-destructive inspection had been performed to identify the induced defects during manufacture or service defects such as cracks, delaminations, damages, repair and bond integrity and also to identify the possible changes in mechanical properties and resin chemistry. In their approach, the material degradation due to heat, humidity, ultraviolet (UV) radiation, oxidation, etc. have also been investigated for composite structures. In addition to the above procedures, bearing conditions around holes and fasteners were investigated as well.

The investigated composite structure according to (Tomblin & Salah, 2010) showed no obvious signs of ageing to the naked eye such as pitting corrosion would be seen on a metallic structure after a similar service life. However, the physical tests showed that there were increased moisture levels in the structure due to ageing. Mechanical testing on coupons extracted from the structure was performed to investigate any degradation in the mechanical properties of the composite material. Visual inspection was performed using optical methods to detect porosity /micro cracking and any evidence of ageing in the structure. The images from the optical system showed the evidence of porosity embedded in the laminate. To fully consider the effect of ageing aircraft structures, appropriate inspection intervals were developed to study the effect of service and accidental damages. Fatigue cracks have also been studied by (Tomblin & Salah, 2010) and (Salah & Tomblin, 2010) and it was noted that fatigue cracks have been found to arise in internal loading membrane, load bearing skins and fastener holes on the horizontal stabilizer of a decommissioned Boeing 737-200 aircraft.

There have been various studies on predicting the fatigue life in polymer composites by means of studying the parameters such as change in modulus, degradation of residual strength and actual damage mechanisms (Harris, 2003). Fig. 1.3 shows the reduction in the residual strength of CFRP material subjected to variable loading conditions. As the number of cycles increases, the strength of the composite materials are adversely affected by repeated loadings as damage accumulates in the material and results in the reduction of residual strength as shown in Fig. 1.3. In a similar way there is a reduction in stress

wave factor, which is a measure of attenuation of ultrasonic waves as they propagate through the CFRP material during the fatigue loading cycles and is shown in Fig. 1.4. The stress wave factor is defined as the root mean square of the power spectral density of the acousto-ultrasonic signal and a reduction of stress wave factor is a strong indication of the presence of damage inside the material (Talreja & Duke, 1988).

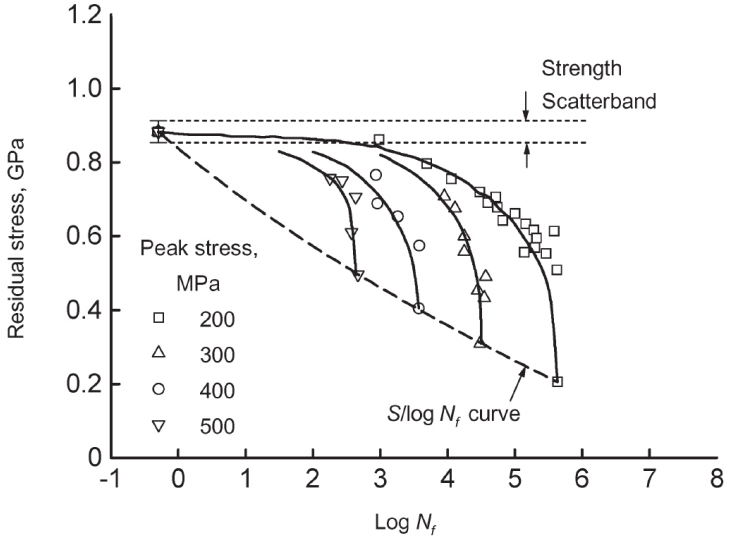

Figure 1.3 Reduction in residual strength due to ageing (Harris, 2003)

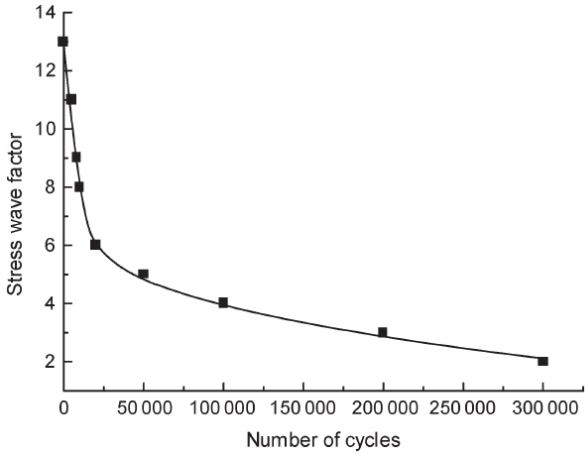

Figure 1.4 Reduction in stress wave factor due to ageing (Harris, 2003)

1.2 Ultrasonic Non-destructive Testing

Ultrasonic non-destructive testing is one of the most efficient methods of inspecting structural composite parts. As a part of the periodic inspection, this method is applied on critical and non-critical aircraft parts to detect subsurface defects such as impact

damages, delamination and matrix cracks. The conventional ultrasonic inspection uses the pulse-echo technique in which a single element piezoelectric transducer is used for transmitting and receiving ultrasonic waves in the test material. If one needs to scan a larger area, an automatic scanning system can be applied where the transducer is moved on a large component by a scanning system controlled by the user. In the last 10-15 years, phased array ultrasonic transducers have been widely applied. Phased array ultrasonic testing (PAUT) uses an array of single transducer elements, which can be triggered at slightly different times in phase and amplitude to produce wave fronts suitable for inspection. A single crystal probe with limited movement and single beam angle has a higher probability of missing mis-oriented cracks. Unlike single element transducers PAUT can perform angular or sectorial scanning that can detect mis-oriented flaws being located randomly away from the beam axis. This in turn reduces the number of inspection units required for any automated system and offers greater flexibility in varying the angle of inspection and focusing the beam in the region of the interest.

Fig. 1.5 shown below is a typical weld inspection as demonstrated by both conventional and phased array ultrasonic transducers. The single crystal transducer needs to be moved manually from one position to another in order to cover the inspection area, whereas the phased array transducer can use sectorial scanning which can steer the ultrasonic beam in the inspection area without physically moving the transducer.

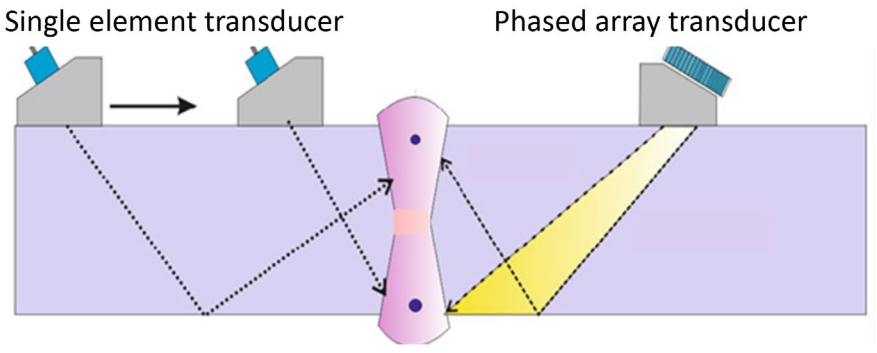

Figure 1.5 Phased array ultrasonic inspection of welds

Usually single element transducers are moved manually by an operator or mechanically by a scanner to cover a large inspection area. During the scanning, the probability of flaw detection highly depends on the data acquisition system. Phased array transducers reduce

the number of scanning movements by performing electronic scanning without compromising the coverage area of the inspection.

The Sampling Phased Array (SPA) or Full Matrix Capture (FMC) approach is an advanced signal processing and image reconstruction method that uses phased array transducers. The difference exists with the conventional/normal phased array principle in terms of data acquisition and data processing. The unique feature of getting accessed to all the signals from the individual elements in the phased array transducer could allow one to perform high speed inspection and efficient quantitative imaging using SAFT (Synthetic Aperture Focusing Technique). Unlike SPA/FMC, the information of the individual elements is lost in PAUT due to phase summation. By the SPA principle, one saves all the sender and receiver elements signals in an information matrix and later an appropriate algorithm is applied to reconstruct the data available in the information matrix to be represented as an image. One such reconstruction algorithm is called Reverse Phase Matching (RPM), which has been developed by the author and others (Sridaran Venkat, Bulavinov, Pudovikov, & Boller, 2010) at Fraunhofer IZFP for inspecting CFRP and other anisotropic materials such as austenitic welds (Pudovikov, 2010). For any anisotropic medium to reconstruct the data from the phased array transducer more appropriately, RPM requires computation of slowness curves of the medium, which is obtained through the stiffness matrix in terms of elastic constants. RPM offers a twofold advantage, i.e. 1. characterization of flaws in CFRP structures by taking anisotropy into account and 2. estimation of the elastic properties obtained through iterative reconstruction of images. Application of RPM for characterising various defects in CFRP has been widely mentioned in literature (Bulavinov, et al., 2008) and (Sridaran Venkat, Bulavinov, Pudovikov, & Boller, 2010) whereas the estimation of the elastic properties of an unknown austenitic weld using RPM has been developed by Pudovikov et al. and has been referred to as GEDCM (Gradient Elastic Descent Constant Method) (Pudovikov, 2013).

1.3 Structural Health Monitoring (SHM) of Aircraft Structures

Any engineering structures can be designed either safe life or damage tolerant. In the former case, as soon as the fatigue limit is reached, the structure is withdrawn from the service, although some useful life of the structure may remain available. In this approach, structural failure is assumed when the cracks are first formed and does not explicitly

consider the possibility for crack growth. The maximum allowable service life is calculated by dividing the mean service life of the components by a factor of safety in the range of 2 to 4 (Grandt, 2003). This design principle considers a crack as the nucleation process and the factor of safety represents the "scatter or uncertainties" during the fatigue process, as well as during fatigue testing. In (Grandt, 2003) some of the failure cases of the U.S. Air Force's safe-life designed aircraft were addressed. The aircraft *KC-135* was initially designed for 13,000 flight hours but unstable cracks in the lower wing skins resulted in only 8,500 service hours.

Damage tolerant design assumes the structure to contain initial cracks being detected through routinely monitoring to avoid that a critical limit of the crack is reached. Within this approach, slow-crack growth and fail-safe design methods are used for demonstrating single path and multi-path loads to guarantee that the structure does not fail during the service life. The difference in fatigue life between safe life and damage tolerant design can be substantial and can easily exceed a factor of two when compared to the safe life design or an exceedance in allowable stresses.

Crack growth must be regularly detected and the damage tolerant design requires a monitoring approach using any approved type of NDT/NDE methods. The trade-off between the detectable crack size and the inspection interval is shown in Fig. 1.6 for a skin-stringer panel. A relatively short inspection intervals is adopted if there is a low possibility of an inspection system to detect small cracks or incipient damages. However, such cracks are likely to be hidden around fasteners or inaccessible areas and most of the time it requires disassembly of the individual components to get access for the inspection, such that aircraft have to be taken out of service which increases operating costs. Many metallic and composite aircraft structures are ageing and are sensitive to pre-existent damages which may put the structure under risk if no specific measures are taken. Those measures could be to get sensing devices integrated onto the structures, which in general terms is referred to as a Structural Health Monitoring (SHM) system. Such a system is the principal integration of sensing and actuating devices onto or into a structure to allow loading and damaging conditions of the structure to be recorded, analysed, localised and finally predicted in a way that NDT becomes an integral part of the structure and the material (Boller, Chang, & Fujino, 2009). Given the recent growth in ultrasonic transducers, data acquisition, and data representation, acoustics based SHM systems are gaining

popularity in aviation industries such as being based on guided waves (GW) widely acknowledged in the aerospace industries due to the following main advantages:

Guided waves are long-range ultrasonic waves, which can cover a large inspection area.

Like conventional ultrasonic bulk waves, they are sensitive to small cracks.

Guided waves can be easily generated using low cost, small piezoelectric transducers of various configurations and sizes and they can be embedded into or attached onto the structures.

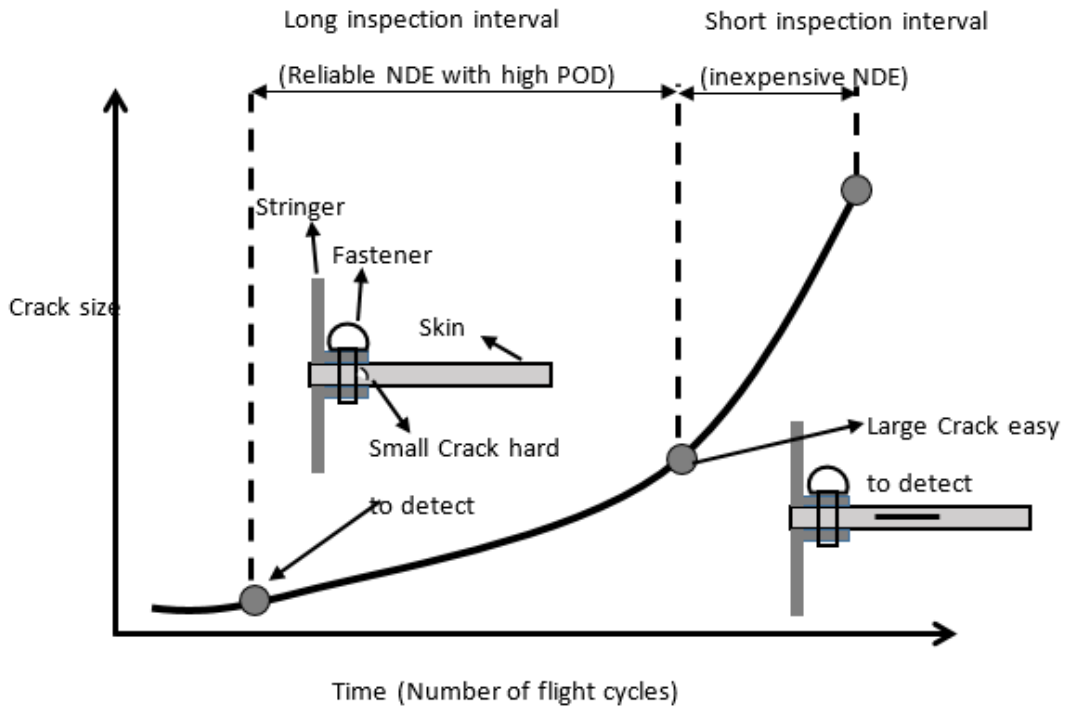

Figure 1.6 Trade-off between detectable crack size and inspection interval

1.4 Uncertainties in Establishing a Health Monitoring Concept for Ageing Structures

1.4.1 Anisotropy

Unlike metallic structures, CFRP is an anisotropic material whose properties are not the same in all the directions. In the interpretation and evaluation of discontinuities, the effect of unaccounted anisotropy can cause a decrease in Probability of Detection (POD). Wave propagation and the resultant interferences are different when compared to the isotropic case, leading to changes in the energy velocity direction and as a result, this can cause

errors in identifying the location and sizing of the defects. Usually, the severity of the anisotropy is defined by elastic constants and for a laminated composite it is even more important to know the laminate properties like orientation and thickness of each layer. Material ageing in the long term affects the strength properties and elastic constants. Although these properties are available before the components are put in service, the actual properties due to ageing remain as an uncertainty as there are no in-situ NDT methods available till date to characterise the materials during service.

The complexity of a structure's geometry or shape and its size is also one of the concerns during the inspection. A large fuselage structure of an Airbus A350 contains curved CFRP panels of several metres that have stringers made of corner joints, T-joints and irregular profiles etc., such that ultrasonic signal/image interpretation from the complex geometries are one of the major concerns in addition to the inspection of the large component in a reasonable time. Usually, point by point scanning of a whole structure results in higher maintenance cost.

1.4.2 Probability of Detection

Even though the SHM community is much excited about the recent developments in the guided wave-based approach there are certain areas, which require thorough investigations before such a guided wave system is deployed onto the structure. Detecting the allowable damage is an important task of any guided wave-based system for a damage tolerant designed structure and the requirement for POD of such a system should be fairly high. A typical SHM system involves an actuator-sensor network to reliably detect the growing damage. An uncertainty arises here as to how actuators and sensors in a GW-based SHM system should be configured such that tolerable damages can be monitored with a high level of POD and hence reliability. The configuration includes best possible positions of the actuators and sensors for a given damage size.

1.4.3 Damage Conditions of Ageing Structures

For a composite material subjected to service over longer terms damages such as delaminations, formation of matrix cracks etc., and accidental damages such as impacts caused due to bird strikes (visible or barely visible impact damages) can occur and reduce the residual strength of the structures. In addition to this, process-induced damages such as

fiber mis-orientations, fiber waviness and disbonds can occur due to the improper manufacturing methods, which can grow during the service life of the structural components in case of being unobserved.

NDT methods are applied during the maintenance and inspection process of components to locate and characterise the size of the damages but when these damages are present in service an uncertainty may arise in understanding how these damages may behave under loading conditions. Generally, NDT methods are well established to characterise damages during the off-line maintenance inspection process. As a part of a maintenance program, identified damages are repaired and the structure is put into service again. However, the nature and the severity of the damages may be uncertain and may occur again, where cases have been demonstrated resulting from lack of structural integrity understanding or even improper repair. The former has been the result in the case of China Airlines Boeing 747-200 in 2002 and the latter of the Japan Airlines Boeing 747-100 in 1985 respectively.

1.5 Role of SHM in Life Cycle Management

The life cycle of a structure is shown in Fig. 1.7 consisting of three main categories: Design, operations and recycling. Having the knowledge of the operating loads that the structure will have to withstand, geometric modelling is very much essential to perform stress/strain analysis in order to identify the hot spots or critical areas in terms of stresses and strains applied, which need to be monitored during the service. Due to the damages likely to occur in those hot spot areas, fatigue analysis has to be performed to understand how these damages will grow further until critical fracture happens defining the end of a structure's service life.

One can also extend the design phase shown in Fig. 1.7 towards realisation of inspection and monitoring systems to detect the damages in those critical areas. Once the structure is put into service, maintenance and inspection becomes a critical part within the process chain. NDT plays a major role in the maintenance and inspection program and it is carried out in predefined intervals where the particular structural component is intermediately withdrawn from the service when a damage is detected by NDT. Interestingly, the uncertainties discussed in the last section can cause problems in the routine maintenance

process if a particular damage grows faster before being detected in the subsequent inspection intervals such as mentioned before within the context of the mis-repairs. SHM offers tremendous advantages in this situation as it involves continuous monitoring of structures using actuators and sensors.

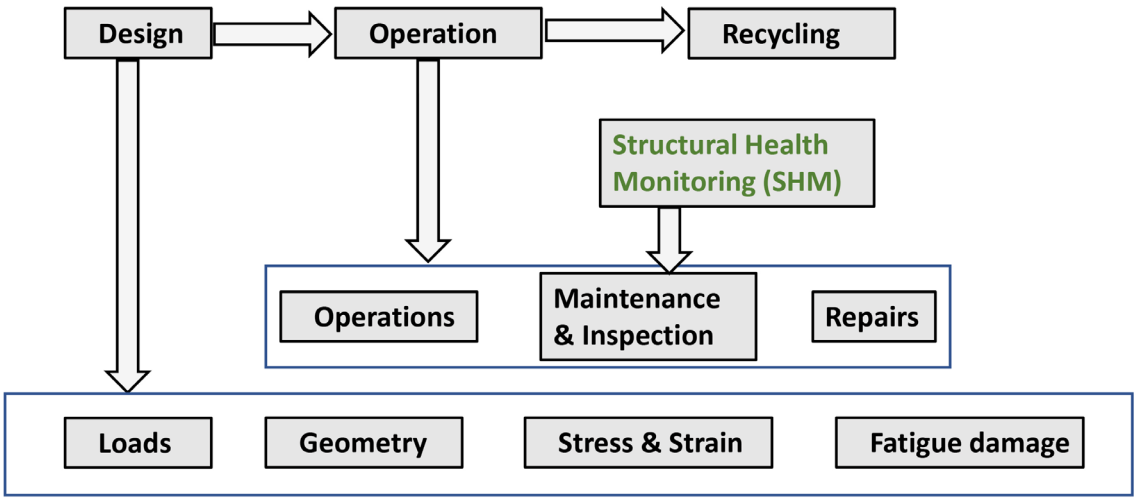

Figure 1.7 Life cycle of a structure

In principle, SHM offers a condition-based maintenance option in the place of a traditional scheduled maintenance. Once the damages are detected and located, the repair has to be performed as per the procedure given by the manufacturer. SHM not only offers a condition-based maintenance concept but also provides a possibility to extend the service life of a structure through the possibility to introduce the damage tolerance design principle in case this has not been applied so far.

Chapter 2

Classical Acoustics and their Development

2.1 A few Fundamentals

Acoustic waves are generated as a point source and are able to travel in any direction of a three-dimensional space as long as those waves are travelling through a material with a material density being > 0. Following the Huygens' principle every point on a wave front is a point source of a new wave. Due to the Huygens-Fresnel principle different waves are allowed to interfere and a wave front being an accumulation of wave point sources again generates a wave front. Material can be modelled from a mechanics point of view as a mass-spring-damper system in 3D space. Such a system depends on the material's density as well as elasticity including the stress being applied. In a virtually infinite volume two types of waves are able to develop: longitudinal waves and transverse waves. A material's capability to carry an acoustic energy and hence an acoustic wave is characterised by the material's acoustic impedance, which is the product of the material's density and the speed of the wave formulated as

$$z = \rho \cdot c \tag{2.1}$$

where ρ is the density and c is the speed of the wave respectively. It already becomes obvious that the speed of an acoustic wave must depend on a material's stiffness as well as on a possible stress being applied and that those parameters can play a further role within an acoustics-based analysis. When an acoustic wave travels from a medium 1 with impedance 1 into a medium 2 with impedance 2 and the two impedances are different then a portion of the incident wave is reflected in medium 1 while another is transmitted into medium 2. Further to this if a longitudinal wave is the incident wave then a conversion to a transverse wave may be possible for the reflected as well as for the transmitted wave. The law being applicable here is Snell's Law where the principle is shown in Fig. 2.1 and which can be mathematically formulated as follows:

$$\frac{\sin\theta_1}{V_{L_1}} = \frac{\sin\theta_2}{V_{L_2}} = \frac{\sin\theta_3}{V_{S_1}} = \frac{\sin\theta_4}{V_{S_2}} \tag{2.2}$$

where,

V_{L_1}- Longitudinal wave velocity in medium-1.

V_{L_2}- Longitudinal wave velocity in medium-2.

V_{S_1}- Shear wave velocity in medium-1.

V_{S_2}- Shear wave velocity in medium-2.

θ_1- Incidence angle in medium-1

θ_2- Angle of transmitted longitudinal wave in medium-2

θ_3- Angle of reflected shear wave in medium-1

θ_4- Angle of transmitted shear wave in medium-2

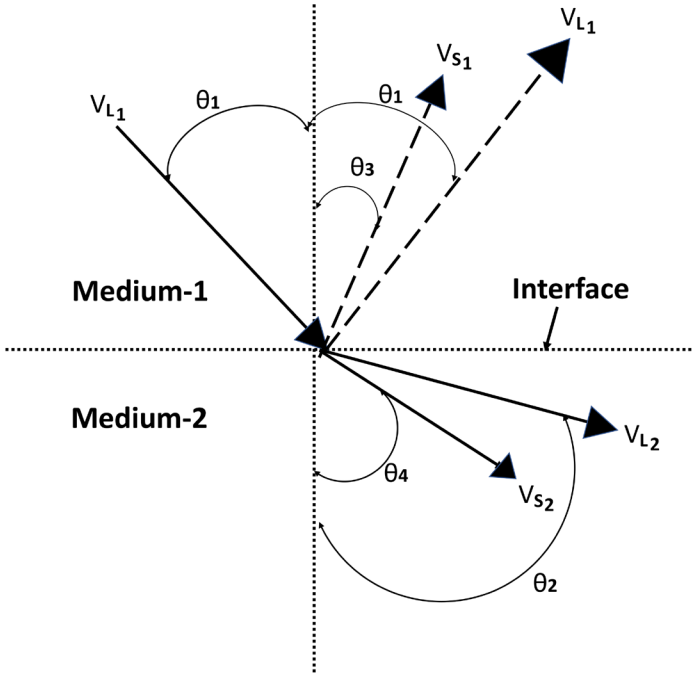

Figure 2.1 Snell's Law of reflection and transmission for a solid/solid interface at an oblique angle

One can use the Equation 2.2 to calculate the angle of the wave transmitted into the medium 2 for any given incidence angle. At normal incidence, a normal longitudinal wave would be excited in medium 1 traveling at a speed of V_{L_1} and reflected into medium 1 would be a longitudinal wave traveling at the same speed as the incident wave. As the incidence angle (θ_1) is increased from zero, according to Snell's law the transmitted longitudinal wave at speed V_{L_2} leads to the transmitted shear wave at the speed of V_{S_2}. Further increase in θ_1 leads to θ_2 reaching 90° to the interface, the corresponding

incidence angle being known as the first critical angle. In this condition, the longitudinal wave is traveling just below the surface of the material interface. As the angle is further increased, the longitudinal wave disappears leaving only shear waves in the medium 2. When angle of the transmitted shear waves (θ_4) in medium 2 reaches 90° to the interface, the angle corresponding to the incidence angle is referred to as the second critical angle. There are different 'critical' angles beyond which a type of wave does not make sense anymore according to Snell's Law and where the type of wave indeed disappears. When such a critical angle is achieved then a surface wave may be generated which is principally also generated when a wave transmission happens between two media of a different acoustic impedance. The most prominent example is surface waves on water where the difference in acoustic impedance between water and air is significant and surface waves on water can therefore be well observed. A typical ultrasonic pulse is represented as a time domain signal as shown in Fig. 2.2, which may contain a number of frequencies with varying phases and amplitudes.

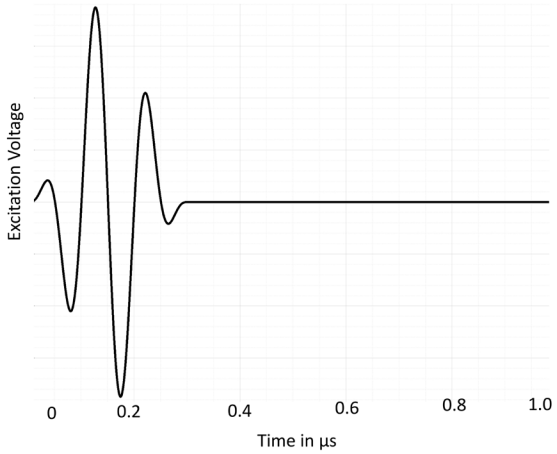

Figure 2.2 Ultrasonic excitation signal

For example, assume that the two waves A and B, having different frequencies ω_A and ω_B as shown in Fig. 2.3, simultanaeously exist in a test specimen. Superposition of two waves results in the pulse shape shown in the bottom of Fig. 2.3. If the speeds of each of the waves are identical, the pulse is undistorted. On the other hand, distortion will occur if there are differences in their travel speeds. The distortion of pulse is termed as pulse dispersion in ultrasonic inspections. The main sources of pulse dispersion are attenuation and wave guide effects (guided waves in plate). Pulse dispersion is described by defining phase (Cp) and group speeds (Cg). The phase speed is the rate of travel of a

point of constant phase in a pulse, and the group speed is the travel speed of the entire pulse as shown in Fig. 2.3 at the bottom. For a nondispersive case, the phase speeds of the pulse A and pulse B will be equal and the group speed of the entire pulse will be equal to the phase speeds. For a dispersive case, phase speeds of pulse A and pulse B are not the same and the group will travel at different speed as that of a phase speed.

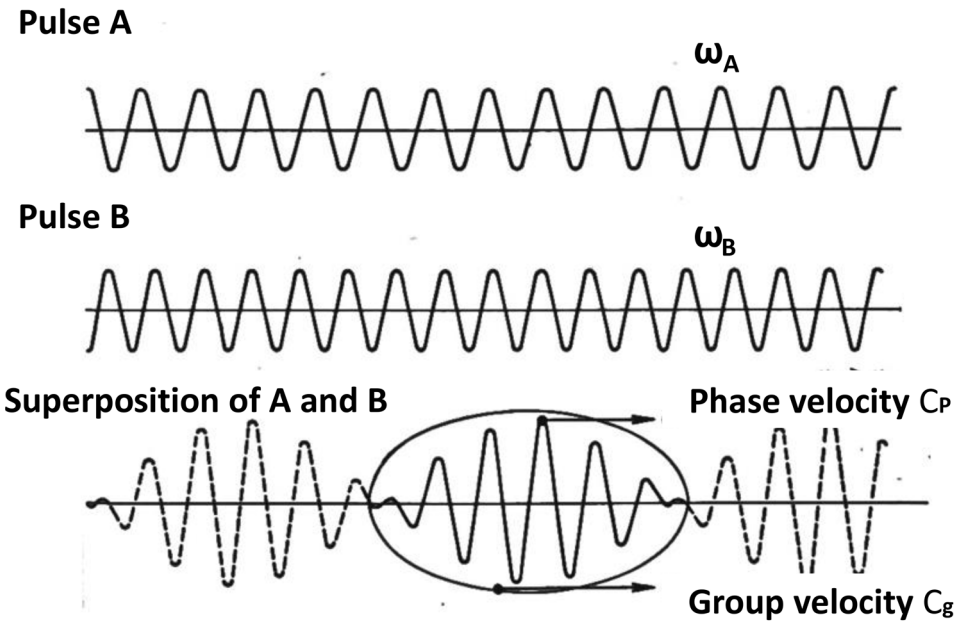

Figure 2.3 Formation of pulse from superposition of continuous wave forms (Bray & Stanley, 1996)

Let k_1 and k_2 to be considered as the wave numbers of pulses A and B, ω_1 and ω_2 to be their frequencies and t is time at given point. Displacements of pulse A and pulse B can be written as follows:

$$u_1 = A\cos(k_1 x - \omega_1 t) \qquad 2.3$$

$$u_2 = A\cos(k_2 x - \omega_2 t) \qquad 2.4$$

The total displacement can be written as

$$u_{total} = 2A\cos\left\{\frac{1}{2}(k_2 - k_1)x - \frac{1}{2}(\omega_2 - \omega_1)t\right\} * \cos\left\{\frac{1}{2}(k_2 + k_1)x - \frac{1}{2}(\omega_2 + \omega_1)t\right\} \qquad 2.5$$

Noting that the cosines are an even function and the following substitutions can be made:

$\Delta\omega = \omega_2 - \omega_1$, $\Delta k = k_2 - k_1$; $\frac{1}{2}(\omega_2 + \omega_1) = \omega_{Average}$, $\frac{1}{2}(k_2 + k_1) = k_{average}$

Hence,

$$u_{total} = 2\,A\cos\underbrace{\left(\frac{1}{2}\Delta kx - \frac{1}{2}\Delta\omega t\right)}_{\text{Low frequency term}} * \underbrace{\cos(kx - \omega t)}_{\text{High frequency term}} \tag{2.6}$$

Here group velocity is

$$C_g = \frac{\Delta\omega}{\Delta k} \tag{2.7}$$

which in the limit becomes $C_g = \frac{d\omega}{dk}$. The high frequency term has also a propagation velocity being the phase velocity

$$C_p = \frac{\omega}{k} \tag{2.8}$$

One can further write the phase and group relations as (Rose, 2014)

$$C_g = \frac{d(kC_p)}{dk} = C_p + k\frac{dC_p}{dk} \tag{2.9}$$

Further details related to the principles of acoustic waves travelling can be found in general textbooks such as (Bray & Stanley, 1996), (Shull, 2002), (Auld, 1973), (Achenbach, 1987) and (Rose, 2014).

2.2 Acoustic Wave Generation Including Phased Array

Most conventional ultrasonic testing techniques use single-crystal probes with divergent beams. Fig. 2.4(a) shows a pulse echo method that uses the piezoelectric transducer for sending and receiving the ultrasonic waves. When an acoustic signal is sent by a transducer and received by another transducer it is known as the pitch-catch method as shown in Fig. 2.4(b) or when signals received by another transducer on the opposite side it is called as through-transmission method as shown in Fig. 2.4(c).

When a conventional transducer is cut into many identical elements, specifically the one operating in the pulse-echo mode, each element will have a width much smaller than its length. Each single small crystal may be considered as a line source of cylindrical waves. The individual wave fronts of the small crystals will interfere, generating the overall wave front.

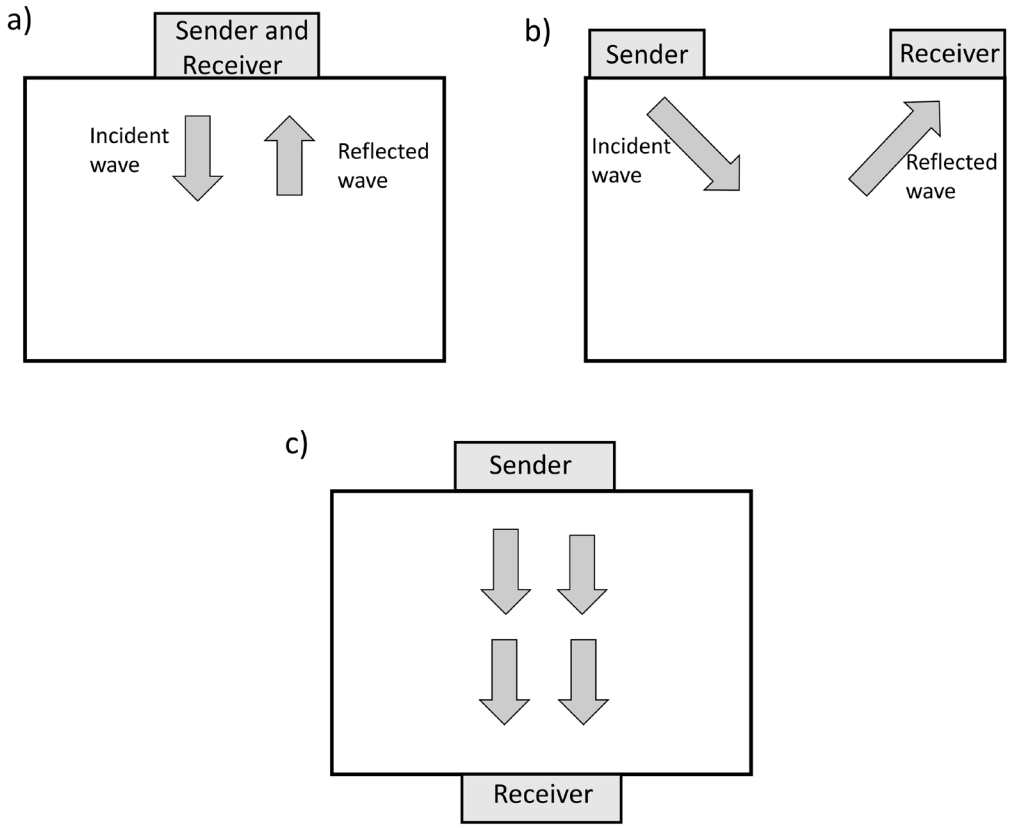

Figure 2.4 Methods of acoustic wave generation and reception a) Pulse-echo method; b) Pitch-catch method; and c) Through-transmission method

The small wave front can be time-delayed and synchronised for phase and amplitude in a way to create an ultrasonic focused beam with steering capability. To generate an ultrasonic beam in phase and with a constructive interference, the individual elements are pulsed at slightly different times, which is called, time delayed triggering. During reception of signals the individual elements are time shifted and summed up. The resulting sum is a single A-scan that emphasises the response from the desired focal point. The principle is explained in Fig. 2.5. During the transmission or triggering cycle the acquisition unit sends a trigger signal to the phased array unit which converts the signal into a high-voltage pulse with a pre-programmed pulse width and time delay. Each element receives one pulse only. This creates a beam with a specific angle and is focused at a specific depth. When the signals are received, they are time-shifted and then reunited to form a single pulse that is sent to the acquisition instrument.

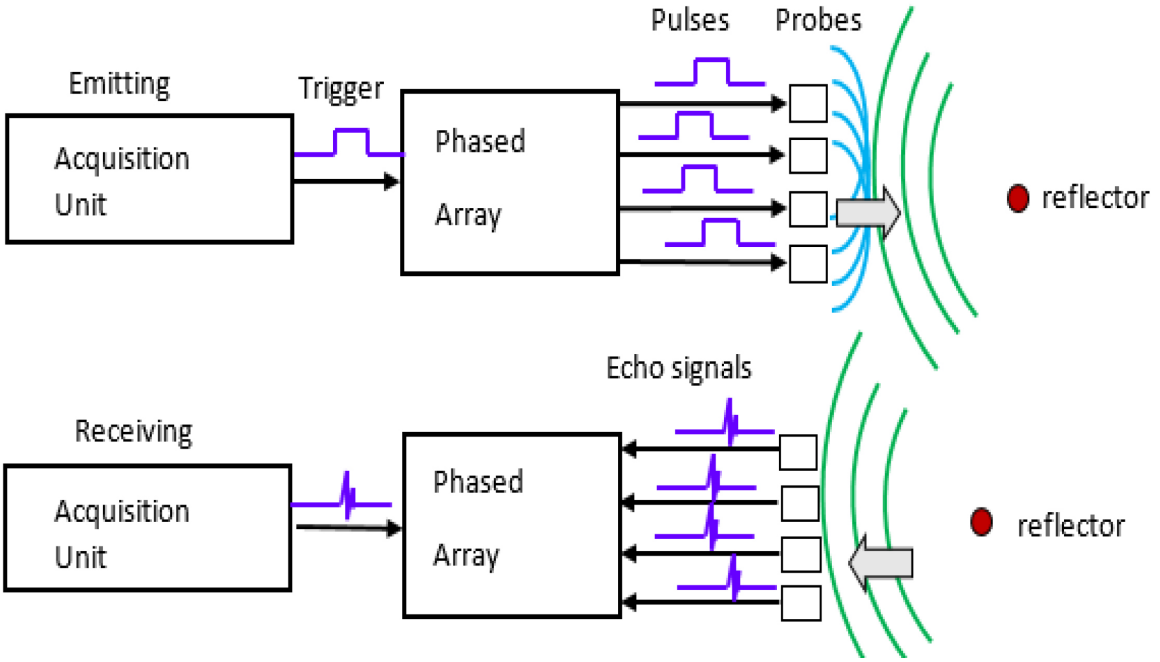

Figure 2.5 Phased array excitation and reception

2.3 Ray Tracing

2.3.1 Ray Tracing for Single Layered Media

Ultrasonic wave propagation in isotropic and anisotropic media using ray tracing has been reported in (Kolkoori, Hoehne, Prager, Rethmeier, & Kreutzbruck, 2014), (Ogilvy, 1986), (Schmitz & Walte, 1999), (Spies, 2004), (Pudovikov, 2013) and (Slawinski, 1996). Ray tracing can be performed by travel time computation, which has been reported in (Sadri & Riahi, 2010).

Fig. 2.6 shows the ray tracing of a single ray that propagates from a single element of a phased array transducer into the inspection volume. The inspection volume is discretized into the number of pixels whose resolution is defined before the ray tracing iteration begins. By knowing the elastic properties of the medium, the ray is moved by a step Δd_1 for the given ray direction. Thus, the single ray which is discretized is allowed to move in the direction for a given ray angle until the thickness of the specimen is reached. The travel time step Δt is computed for every discrete step Δd_1 according to Equation 2.10.

$$\Delta t = \frac{\Delta d_1}{Velocity(\phi)} \qquad 2.10$$

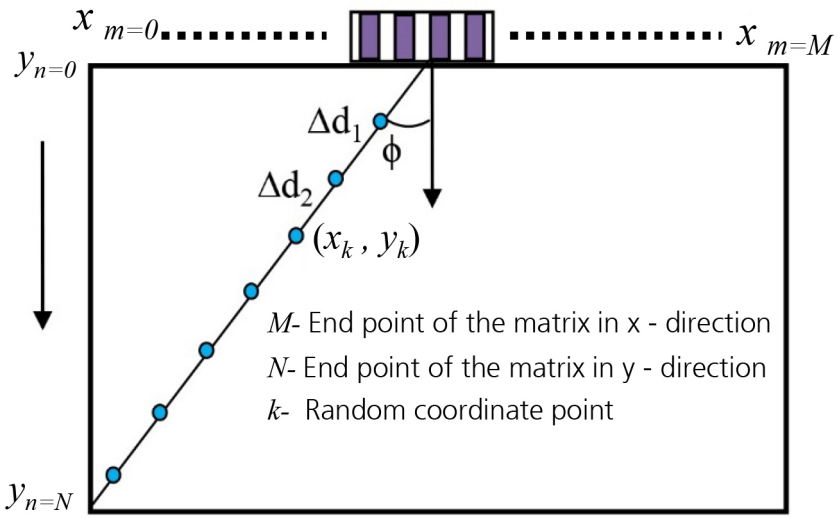

Figure 2.6 Ray tracing in single layered media

For an anisotropic medium, velocity is the function of angle of propagation ($Velocity(\phi)$). Whereas Δd_1 is the distance, and x_m is the position of the element in the transducer as given in the Equation 2.11.

$$\Delta d_1 = \sqrt{(x_m - x_k)^2 + {y_k}^2} \qquad 2.11$$

The difference in the travel time distributions for an isotropic and an anisotropic medium for the center element of the transducer computed through ray tracing is shown in Fig. 2.7.

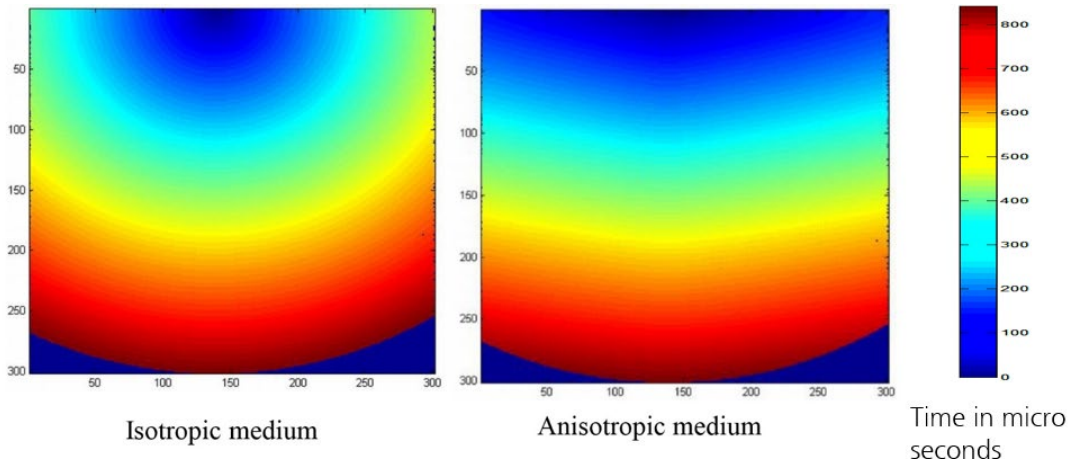

Figure 2.7 Travel time distribution for isotropic and anisotropic medium for the center element of a phased array transducer

The ray tracing result can be affected by the following parameters:

1. Resolutions in directions M and N as shown in Fig. 2.6
2. Elastic constants and density of the medium,
3. Angle range for propagation angles,
4. Angular step,
5. Thickness of the test specimen,
6. Sampling frequency of the signal.

2.3.2 Ray Tracing for two Layered Medium

Fig. 2.8 shown below explains how to compute ray tracing for a two-layered medium.

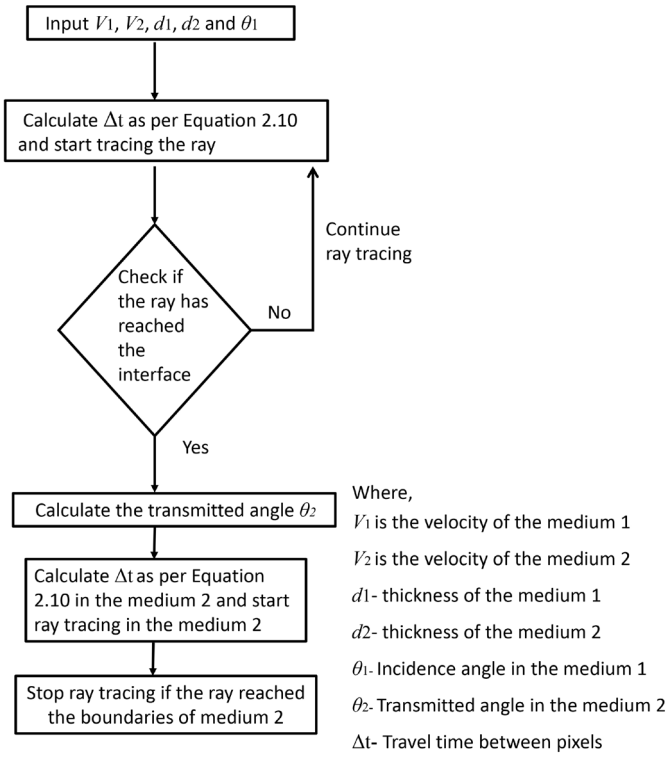

Figure 2.8 Flowchart for ray tracing in a two layered medium

2.4 Synthetic Aperture Focussing Technique (SAFT)

SAFT is referred to as the Synthetic Aperture Focusing Technique (Doctor, 1986) and (Spies & Jager, 2003) and it is a process in which the focal properties of a large aperture of focused transducers is synthetically generated from the data collected over a large area using a small transducer with a divergence sound field. The processing required to focus this collection of data has been called beam forming, coherent summation or synthetic

aperture processing. The SAFT technique was developed to improve the resolution along the track direction for side-looking radar (Fitch, 1988). The idea is to record data from the sequence of pulses from a single moving real aperture and then, with suitable computation, to combine the signals, such that the output can be treated as a much larger aperture. In conventional phased array ultrasonic testing the depth of the near field is given by $\frac{D^2}{4\lambda}$ where D is the diameter of the transducer and λ is the wavelength. Naturally one can focus in this field as the beam field converges in the near field and diverges in the far field being recommended for characterising the defect sizes in this region. When the size of the aperture increases, the near field depth also increases but it is impractical to have a big transducer in order to inspect high thickness of the component under test. One way of doing this and getting around the problem is to use a small aperture and record the beam field at each single step throughout the entire length of the specimen. During processing of stored signals, the single point in the reconstructed image is the sum of the beam fields as seen by the transducer when it is moved along the length of the specimen. This means synthesising the transducer so that each point in the test object is focused synthetically. This in brief can be described as SAFT (Seydel, 1982) and (Schmitz, Müller, & Schäfer, 1992).

SAFT in ultrasonic non-destructive evaluation plays an important role in numerous industrial fields to assure quality and integrity of metallic components, which are relevant for the safety of the product. To calculate the safety of such components the knowledge of fracture mechanics is very essential. The conventional ultrasonic testing methods only use the maximum amplitude and its time of flight to describe the defects, resulting in so called reference reflectors, which have only a poor approximation to the real reflectors' sizes. In most cases the size is undervalued, which results in registration of a high number of small defects, being not critical for the stability of the components but causing higher repair costs. Hence techniques should be developed to evaluate the accurate size and position of the defects. In this context SAFT has been successfully applied for many years in order to quantitatively determine the location, shape, size and orientation of the defects. The advantage of SAFT is to improve the signal to noise ratio, to evaluate size, location and orientation of a defect. SAFT can be done in both time and frequency domain. Here the implementation of SAFT in the time domain will be explained. The conventional time

domain SAFT algorithm performs synthetic focusing by means of coherent summations of responses from point scatterers and along hyperbolas. These hyperbolas simply express the distances or time-delays from transducer positions in the synthetic aperture to the observation points. Here the transducer is mechanically scanned along the x-axis and at each sampling position x_m . The distance between the transducer position and the observation point is given by distance R as shown in Fig. 2.9. To specifically achieve a focus at an observation point, the SAFT algorithm time shifts and performs a summation of the received signals measured at the transducer position x_m for all m positions in the synthetic aperture.

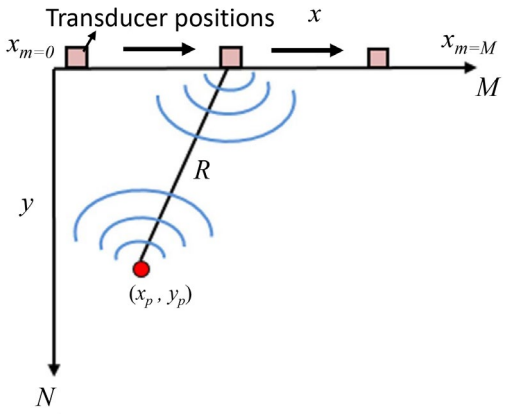

Figure 2.9 Synthetic Aperture Focusing Technique (SAFT) principle

The time shifts, which aim to compensate for differences in the pulse traveling time are simply calculated using the Pythagorean theorem and the operation is commonly expressed in the following continuous form

$$Time\ shifts\ = \frac{2\sqrt{(x_m - x_p)^2 + {y_p}^2}}{C} \qquad 2.12$$

where C is the velocity of the wave in the medium. The beam field at an observation point in a reconstructed image is obtained by the summation of all the beam fields acquired by the transducer at each m position along with the calculated time shifts from the Equation 2.12. The conventional SAFT data acquisition is shown in Fig. 2.10. During data acquisition the aperture is scanned for all probe positions and the complete unprocessed signals coming back out of the specimen are picked up and stored, i.e. for each probe position (x, y) inside the scanned aperture, with the complete received ultrasonic

signals being stored as input-data for the SAFT algorithm. Thus, for each probe position the received time-dependent amplitude values with the interval from t_0 to t_{max} are picked up. Because of the wide beam opening angle of the probe the returning echoes from different reflectors may be received and stored simultaneously and not only separated by time but also superimposing each other. Usually the data will be obtained using a computer-controlled manipulator and the complete ultrasonic A-scan signals are stored.

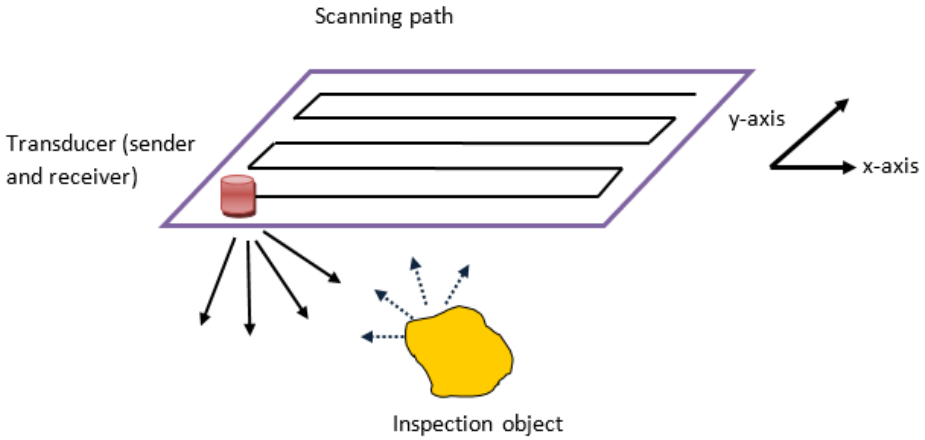

Figure 2.10 Data acquisition in SAFT

The reconstruction area is chosen as a plane parallel to the scanned line-aperture and perpendicular to the surface to form a B-scan image. This is explained in Fig. 2.11 for every discrete pixel-point inside this plane where the time of flight from the actual probe position to this point and back is calculated and the amplitude data belonging to this time of flight and probe-position is added to the amplitude value already stored at the coordinates of the pixel point. This is done for all pixels inside the probe beam opening angle and all probe positions.

This procedure results in constructive interference for all pixel points where ultrasound is reflected from the defect's surface and destructive interference points anywhere else in the reconstruction area. Thus, the reconstructed amplitude distribution will show high amplitude values on the defects' surface and low values (noise levels) elsewhere.
The principle of the reconstruction procedure is: The reconstruction plane is divided into small areas representing pixels, with the received signals being added into the pixels according to their time of flight and divergence angle. Thus, the time corrected summation of the A-scan signals essentially works as an averaging method providing signal-to-noise

ratio enhancements. The difference resulting from SAFT for a phased array transducer is shown in Fig. 2.12.

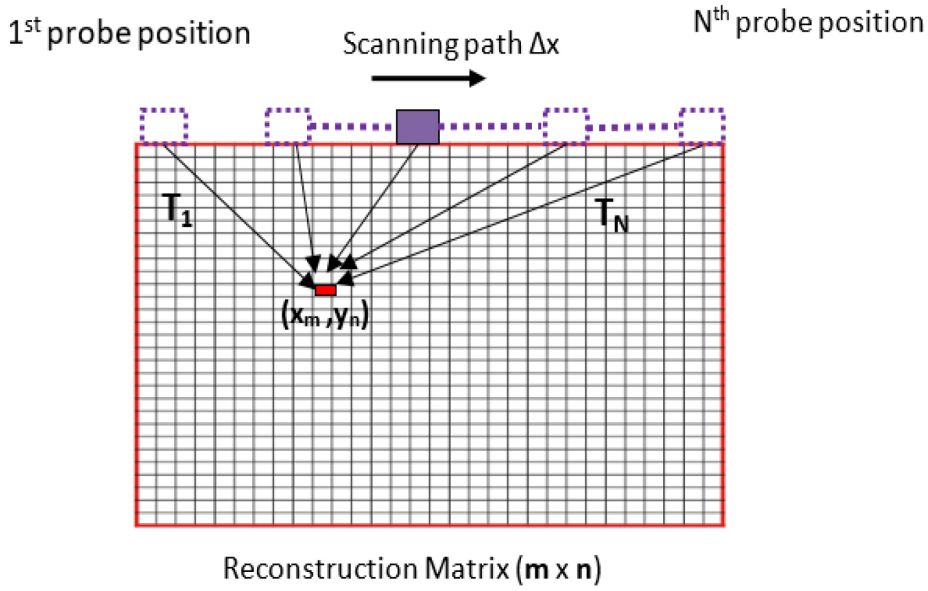

Figure 2.11 SAFT reconstruction for single element transducer

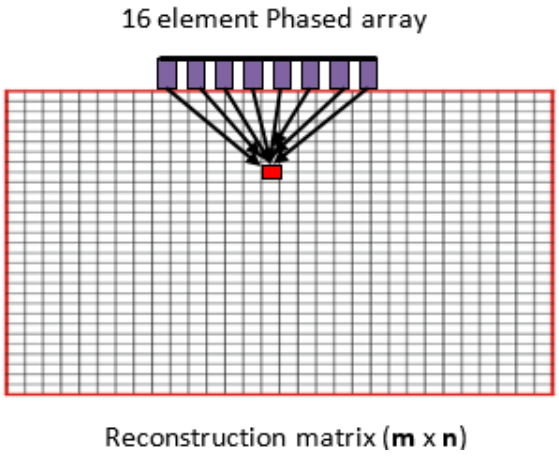

Figure 2.12 SAFT reconstruction for phased array transducer

More of its implementation for a single element transducer can be referred to in (Schmitz, Müller, & Schäfer). For the conventional SAFT, the probe has to be moved in order to synthesise the transducer, whereas in a phased array ultrasonic system, this is achieved by taking advantage of the axial position of the individual transducer elements of the phased array transducer. However, when the same phased array transducer is moved as like that of the traditional SAFT, the aperture will be synthesised further.

2.5 Sampling Phased Array (SPA) or Full Matrix Capture (FMC)

2.5.1 The General Principle

Many signal and image processing methods have been developed in the recent past. Among those the Sampling Phased Array (SPA) technique developed by the Fraunhofer Institute for Non Destructive Testing (IZFP, Germany) offers many advantages for very wide applications with respect to quantitative non-destructive evaluation (QNDE) (Bulavinov, et al., 2008). While conventional phased array requires several shots at different angles to cover an entire cross section in SPA the same can be achieved with a single insonification (single shot). The returning ultrasonic echo signals from a single shot by one transducer element are captured by every one of the transducer elements Fig. 2.13. The signals received are later used to reconstruct one or more arbitrary angles and/or focus depths. The reconstruction of the data is greatly enhanced through the application of SAFT, which eliminates noise and enhances sensitivity.

One shot or one inspection cycle in SPA means one of the elements in the phased array acts as a sender and all the other elements including the sender act as receivers. The A-scan information of this particular shot in terms of sender-receiver combination is stored as an information matrix as shown in the Fig. 2.13 on the right side. This is called a 1xN shot. In a similar fashion, when all the remaining elements repeat the above process this constitutes a N x N shot where N is the number of elements in the phased array transducer. The information matrix thus obtained after N x N shots has all the A-scan information of each sender to receiver combination. They are stored as unprocessed A-scans without the application of the time delay. In contrast this A-scan information of sender-receiver combination of each shot or each inspection cycle of the conventional phased array (CPA) is lost due to time correction and subsequent phase summation. One of the advantages of SPA is a very wide transmitter beam directivity owing to a small array element size ($d \sim \lambda/2$), which can be approximated by the beam directivity of the point source which means that in every single transmitting act a very big volume of inspecting object can be insonified. The received signal contains information about the reflectors lying under the different insonification angles. By appropriate phasing on the receiver side one can obtain arbitrary receiver beam directivity.

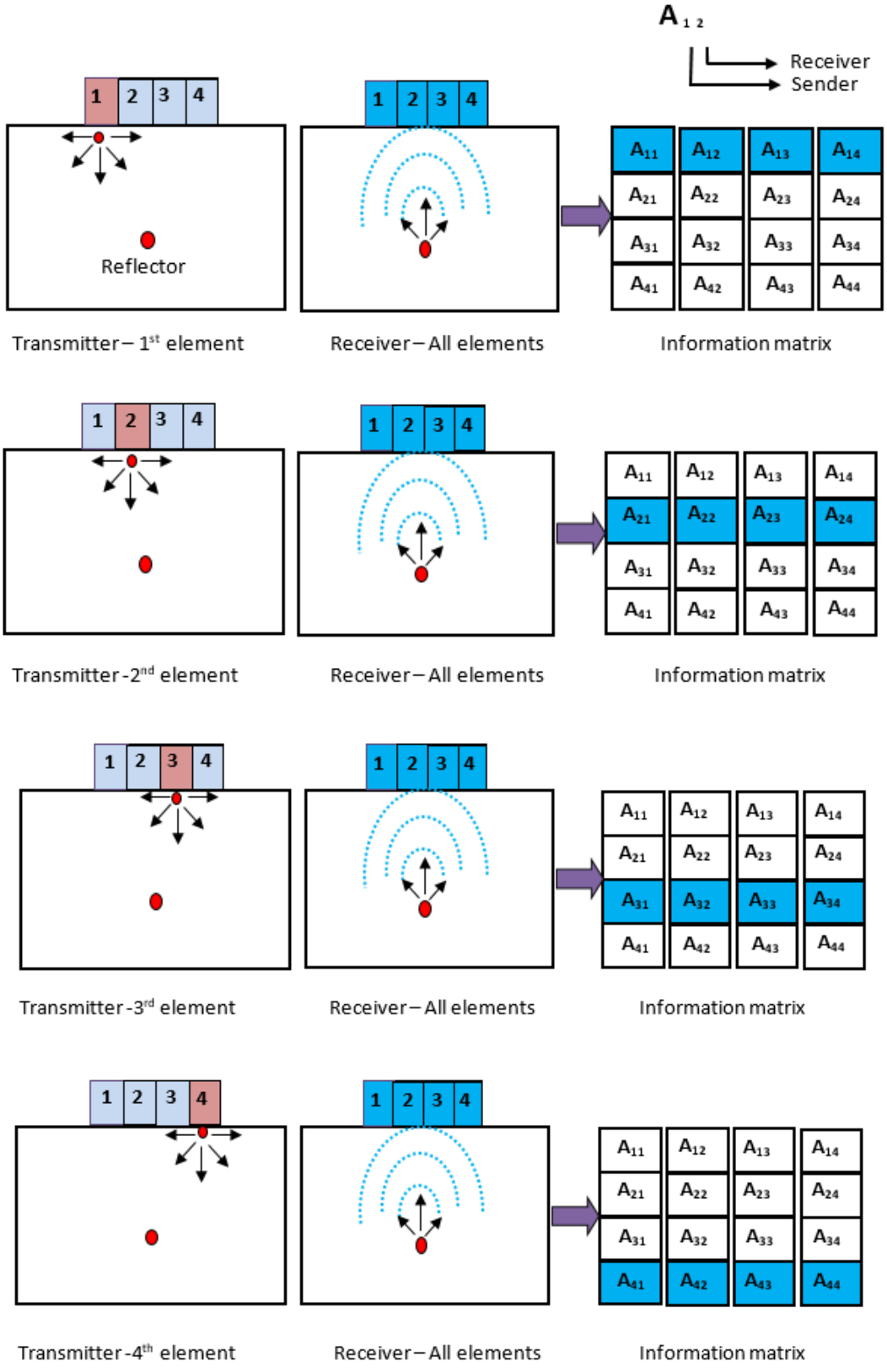

Figure 2.13 Excitation and reception sequences in SPA

The principle of conventional phased array consists of applying the time delays during the transmission and time correction during the reception.

Fast data acquisition, data storage and data processing capabilities permit the analysis of individual time-signals received from the information matrix of the phased array. This can be achieved if only one transducer element is programmed to transmit the sound into the material and all other elements are set to receive and store all the returned signals. The delay during the transmission can be written in conventional phased array form as follows:

$$t_n = n\frac{d}{c}\sin\theta + t_0 \qquad 2.13$$

where t_n is the delay for the n^{th} element of the array and

n is the index number of the element,

c is the sound velocity in the material,

θ is the insonification angle, and

d is the inter-element distance.

t_0 is an additive term constant for all array elements to avoid negative delay values.

The time delays for the receiving signals are not the same but they are symmetric to the transmitting act. The receiver delay for a conventional phased array element is written as follows (Papadakis, 1986):

$$t_n = \frac{F}{c}\left\{1 - \left[1 + \left(\frac{nd}{F}\right)^2 - 2\frac{nd}{F}\sin\theta\right]^{\frac{1}{2}}\right\} + t_0 \qquad 2.14$$

F is the focal distance in the Equation 2.14. In the case of SPA, the transmitter delays are absent, because firing of the elements occurs sequentially. Nevertheless, one can imagine that transmission, reception and propagation processes occur simultaneously, without affecting each other.

2.5.2 Reconstruction for Isotropic Medium for SPA Data

The area where the image of the test specimen will be projected is divided into a number of pixels, which is called the reconstruction matrix. The travel time between each element position and the pixel in the reconstruction matrix is calculated using the distance formula and the velocity of the medium. These time values are stored for each element in the form of a so-called Look Up Table (LUT). During the reconstruction of the data, LUT is used for computing the delay and the summation of the amplitude values being

performed for the single pixel point from the sender-receiver data as shown in Fig. 2.14. The picture to be shown is the reconstructed image of the sector scan for an isotropic medium.

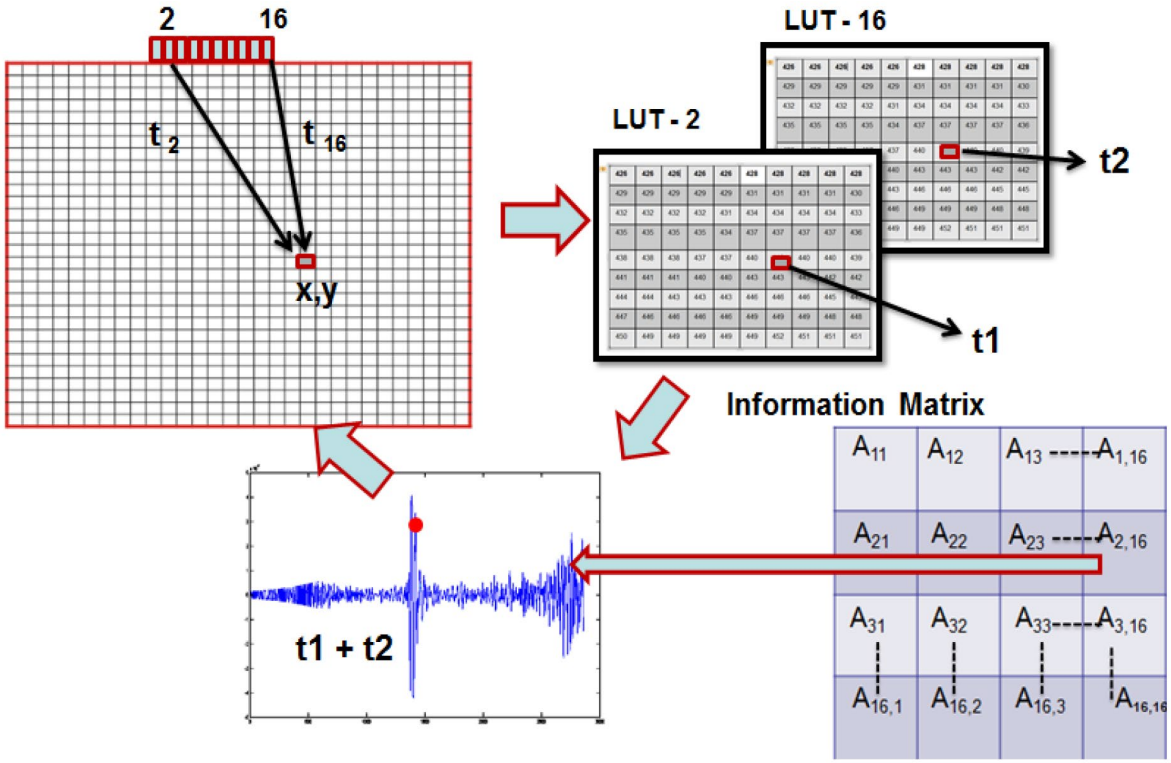

Figure 2.14 SAFT reconstruction for isotropic medium

The test specimen has side-drilled holes located at different depths. SAFT reconstruction is performed on the data acquired through SPA. The comparison of the S-scan images for both conventional PA and SPA are shown in Fig. 2.15. This shows the differences in the reconstructed image between SPA and the conventional PA. The test specimen has side-drilled holes at different depths and at different angles. One can also see the images of conventional phased array without focusing at 5 mm depth. In contrast, SPA focuses synthetically on all depths through SAFT reconstruction. Signal characteristics of sampling phased array and conventional phased array have been studied (Bulavinov, 2008). Fig. 2.16 shows that the A-scan signal characteristics of SPA and CPA are the same, which means validation of the SPA technique and the application of current rules for test standards are possible for industrial inspection.

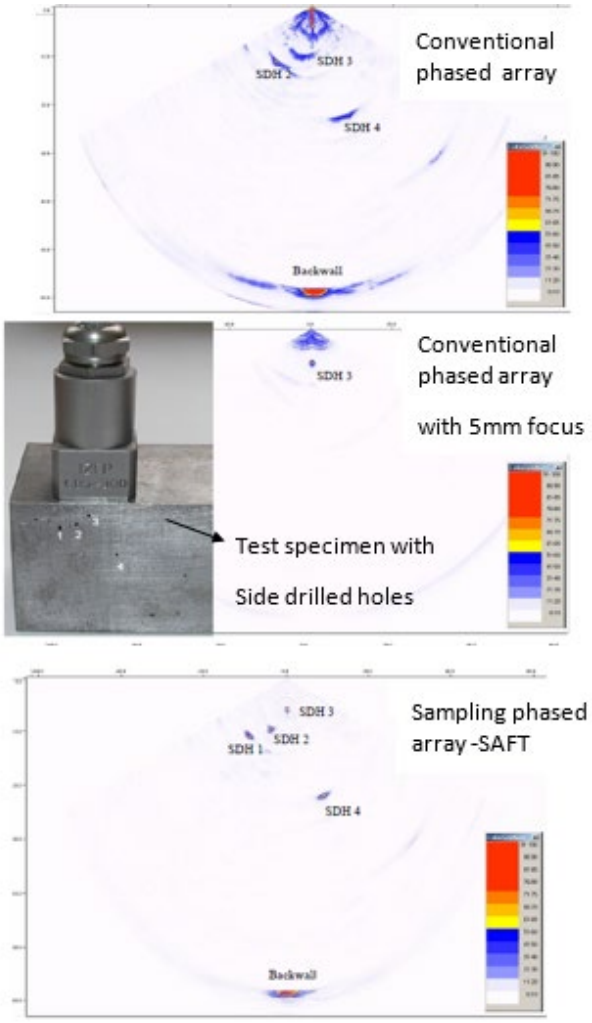

Figure 2.15 Comparison of sector scan images of CPA and SPA (Bulavinov, 2008)

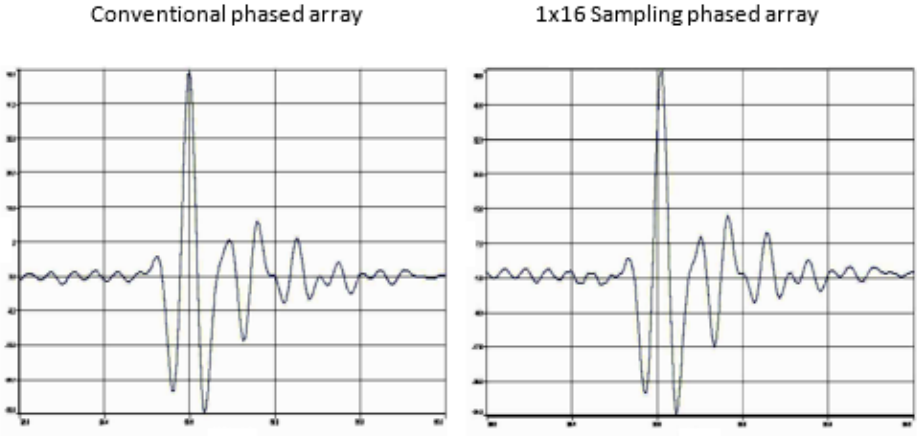

Figure 2.16 A-scan signal characteristics of CPA and SPA (Bulavinov, 2008)

2.5.3 Advantages of SPA

The SPA technique offers a variety of technical advantages, some of which are discussed below.

1. SPA principally employs the transmitter-receiver mode, where the dead-zone (or near-surface) in the test material is significantly reduced. Additionally, the virtual sound field displays all reflectors with optimised focusing.
2. Reverse Phase Matching (RPM) is an additional feature available in SPA for inspection of anisotropic materials, which will be explained in the next section.
3. SPA uses SAFT for image reconstruction, which synthetically focuses all points in the image reconstruction matrix. It is therefore possible to make an appropriate sizing of the defect.

The most important feature is the inspection speed when compared to conventional phased array. Even though the phased array system reduces the number of inspection units required for inspection the speed remains the same. In general, the time-delayed triggering and time-corrected receiving constitutes one shot or one cycle with respect to one inspection angle. If one wants to do sectorial scanning where the beam is steered at different angles, then there may be more shots or cycles required to do this. For example sectorial scanning from -60° to 60° for a 1° step size constitutes 121 shots or 121 inspection cycles, whereas for SPA this information is obtained in one single sample or N samples, where N is the number of elements in the PA transducer thus saving time by a factor of 120 cycles (Bulavinov, et al., 2008) and (Bulavinov, Pinchuk, Reddy, & Walte, 2010).

2.6 Fundamentals of Anisotropy and Determination of Elastic Constants in Anisotropic Media

2.6.1 Wave Propagation in Anisotropic Medium

Propagation of acoustic waves in anisotropic media has been studied for many years. When the elastic properties of a material vary with the direction the material is called anisotropic. The anisotropy can be due to a specific grain structure with respect to austenitic welds or multiple orientation of fibers in case of CFRP. As a result of this anisotropy, basic aspects of wave propagation and wave interference phenomena are different when

compared to the isotropic case, leading to changes in energy velocity, beam skewing, beam splitting, unsymmetrical field profile, side lobe formations, focusing and divergence (Balasubramaniam, 2000) and (Rose, 2004). The main aspect of anisotropy with respect to ultrasonic inspection is the beam skewing, which happens when the wave travels at an angle with respect to the wave front. Due to the variations in the energy velocities, errors can come about in reflector location and sizing. In terms of quantitative imaging, the difference in beam focusing will result in image artefacts and image distortions in the reconstructed image. Sometimes planar defects look like volumetric and vice versa because of the unusual wave superposition. Unless proper anisotropic corrections are made, the ultrasonic imaging will produce a series of errors. The result of anisotropic behaviour in ultrasonic imaging can be well understood from (Spies, 2004), (Spies & Jager, 2003) and (Balasubramaniam, 2000).

To demonstrate the beam skewing phenomenon, as shown in Fig. 2.17, the ultrasonic transducer is placed on a test surface that produces ultrasonic waves traveling in the direction directly ahead of the transducer called the wave front normal. Due to the anisotropic character of the material and the alignment of the material with respect to the transducer, the actual energy flux direction can be at some angle other than normal to the test probe. The variation in acoustic properties with direction in anisotropic media can be represented geometrically in a variety of ways. These representations remain useful in illustrating various aspects of wave propagation in anisotropic media. Kriz and Liu (Kriz & Liu, 2007) have extensively studied the use of representation surfaces to describe the mechanical behaviour of fiber-reinforced structures.

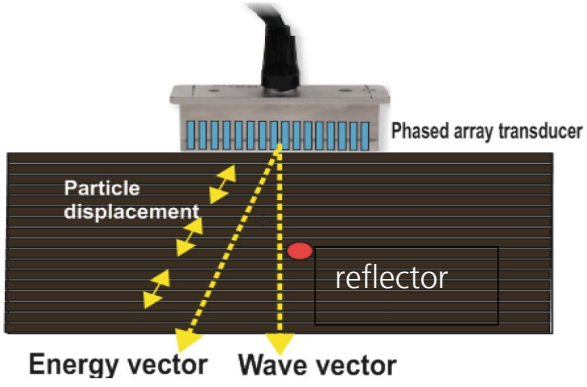

Figure 2.17 Direction of wave vector and energy vector in uni-directional laminate

The directional dependence of elastic properties can be easily visualised with such techniques. The variation of Young's modulus with direction in a uni-directionally reinforced composite is shown in Fig. 2.18 as a function of the fiber volume fraction (V_f). Here the x_3 axis represents the direction of fiber reinforcement and θ represents the angle between the tensile axis and the fiber direction. One can calculate Young's modulus for any given θ and V_f from the composite micro mechanics theory. To construct such curves, one begins with one particular value of θ and calculates the value of Young's modulus in this direction determined from θ. It can be noted from the figure that the section for a zero-fiber volume fraction is circular as the resin itself shows an isotropic behaviour.

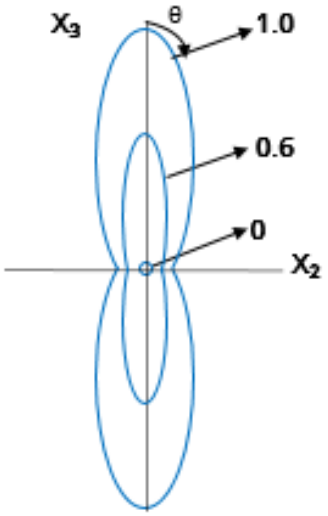

Figure 2.18 Representation of the slowness curve for Young's modulus in a unidirectional composite

However, when additional fibers are added to the material, the stiffness increases, particularly in the fiber reinforcement direction. Similar plots may be developed for the other important material parameters such as shear modulus and Poisson's ratio. For the wave propagation, one can proceed in the same fashion to develop the curves that can be used to characterise the directional dependence of acoustic properties.

Differences in the wave propagation in isotropic media (or anisotropic media in certain symmetry directions) and anisotropic media in non-symmetry directions are shown in Fig.s 2.19 and 2.20.

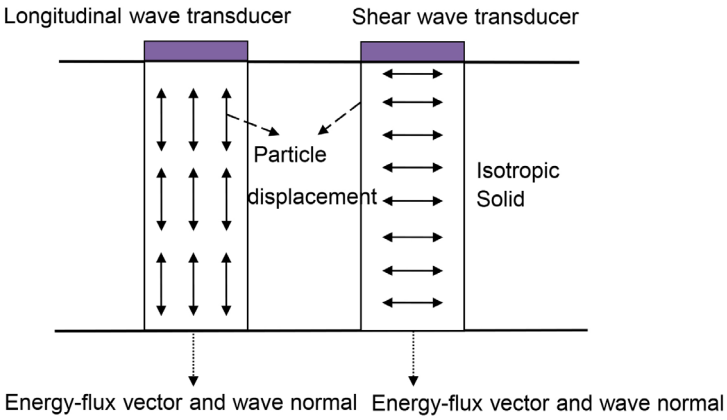

Figure 2.19 Wave propagation in symmetry direction

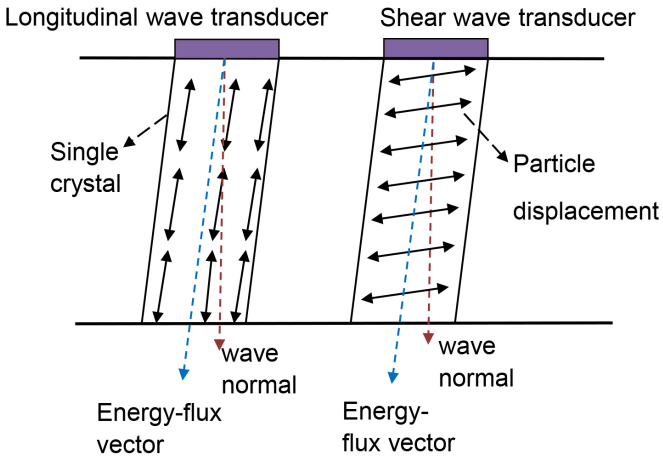

Figure 2.20 Wave propagation in non-symmetry direction

Fig. 2.21 demonstrates the problems of anisotropy regarding detectability and location. This figure shows a snapshot of a simulation for a CFRP material, which exhibits a high degree of anisotropy because fibers are oriented in a 50° direction.

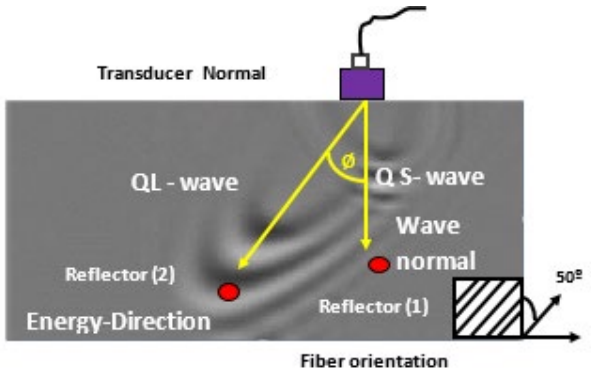

Figure 2.21 Effect of anisotropy in wave propagation (Kriz & Liu, 2007)

Two interesting possibilities can occur during ultrasonic testing for detection and location of the reflector as shown in the same figure. The ultrasonic transducer beam is normal to the reflector (1). Usually, for the isotropic case, there should be a strong reflection from the reflector (1) and location may not be a problem whereas for the anisotropic case the energy travels in the direction of the orientation of fibers so it will fail to detect the reflector even though the transducer lies normal to it. The reflector (2) which lies in the direction of the energy vector can be detected with the transducer lying in the same position with respect to the above point but it can be located wrongly as the transducer is normal to reflector (1) but not to reflector (2). In Fig. 2.21 Ø is called the skewing angle. In order to understand this behaviour of wave propagation, many authors have performed modelling for further understanding. An interesting work associated with anisotropic behaviour for weld material has been presented by (Ogilvy, 2000), (Chinta, Mayer, & Langenberg, 2012), (Connolly, Lowe, Rokhlin, & Temple, 2008), (Kim, Song, & Kang, 2011), (Kolkoori, et al., 2013) and (Kramer, 1989) where a theoretical ray-tracing models were discussed. A numerical integration of Green's function model was discussed by (Balasubraminam, 2000) which provides flexibility in modelling and is computationally easy to study the ultrasonic bulk wave propagation in anisotropic media. Ultrasonic imaging can produce a series of errors with respect to anisotropic materials producing multiple images and distorted images, all as a result of the phenomena discussed in the above paragraphs in case anisotropy is not considered adequately. Anisotropic wave propagation can also be understood by constructing phase and group velocities (Rose, 2004).

The characteristic wave equation in anisotropic media has been presented by several authors (Helbig, 1994), (Gopalakrishnan, 2011), (Rose, 2004), (Gao, 2007), (Giurgiutiu, 2015), (Nayfeh, 1995), (Rokhlin, Chimenti, & Nagy, 2011), (Bing & Greenhalgh, 2004) and (Bing & Min-Yu, 1999). The basic form of the wave equation in anisotropic media is derived from the Christoffel equation assuming various symmetries in the material, where phase velocities and group velocities can be obtained by solving the eigenvalue problem and the eigenvector represents the direction of wave propagation and the eigenvalue the velocities respectively. In the case of an anisotropic medium, three velocities from the different wave types are possible: 1. Longitudinal wave, 2. Shear wave vertical and 3. Shear wave horizontal.

In an anisotropic medium phase velocity and group velocity are direction dependent and the two are generally moving in different directions. In a transversely isotropic homogeneous medium (TI), velocity of propagation depends on the direction of propagation measured from the symmetry axis. The elastic wave equation can be used to find the phase velocity as a function of the phase angle. This can be related to the group direction (ray direction) and group velocity as shown below (Helbig, 1994) :

$$V^2\big(\phi(\theta)\big) = v^2(\theta) + \left(\frac{dv}{d\theta}\right)^2 \qquad 2.15$$

and

$$\tan\phi = \frac{\tan\theta + \frac{1}{v}\frac{dv}{d\theta}}{1 - \frac{\tan\theta}{v}\frac{dv}{d\theta}} \qquad 2.16$$

where V and ϕ are magnitude of group velocity and group angle respectively. These equations are taken from the Pythagorean theorem: the ray velocity is the vector sum of motion perpendicular to the wave front and motion parallel to the wave front. In general, there are three different velocities corresponding to three different modes. The phase angle θ is the angle between wave front normal and the axis of symmetry, while group or ray angle ϕ is the angle between ray (energy flow) direction and the axis of symmetry. In isotropic systems (Bulavinov, et al., 2008) every direction is an infinite fold axis of symmetry and hence elastic properties are independent of direction.

The exact expressions for phase velocities of three modes are given in Equations 2.17 to 2.19 as according to (Helbig, 1994), (Postma, 1955) and (Stopin, 2000).

$$\rho v^2{}_P = \frac{1}{2}[C_{33} + C_{44} + (C_{11} - C_{33})\sin^2\theta + D(\theta)] \qquad 2.17$$

$$\rho v^2{}_{SV} = \frac{1}{2}[C_{33} + C_{44} + (C_{11} - C_{33})\sin^2\theta - D(\theta)] \qquad 2.18$$

$$\rho v^2{}_{SH=}\, C_{66}\sin^2\theta + C_{44}\cos^2\theta \qquad 2.19$$

where ρ is the density of the medium, C_{ij} are the elements of the stiffness matrix and $D(\theta)$ is given by:

$$D(\theta) = \{(C_{33} - C_{44})^2 + 2[2(C_{13} + C_{44})^2 - (C_{33} - C_{44})(C_{11} + C_{33} - 2C_{44})]sin^2\theta + [(C_{11} + C_{33} - 2C_{44})^2 - 4(C_{13} + C_{44})^2]sin^4\theta\}^{1/2} \qquad 2.20$$

2.6.2 Backwall Reflection Method

Li et al. (Li, Pain, Wilcox, & Drinkwater, 2013) and Drinkwater et al. (Drinkwater & Wilcox, 2006) developed a more pragmatic approach for directly measuring the group velocity as a function of group angle and adopted two experimental approaches: the backwall reflection and through-transmission methods. In this current work, the backwall reflection technique is used to get the plot of the group angle versus group velocities for the unknown material properties of the CFRP specimen. The initial results look promising and can be applicable for all the test samples whose elastic constants are unknown. For successful application of this method the component of interest must be a flat composite laminate with front and back faces that are parallel to each other. Under this assumption, the ultrasonic group velocity in any through-thickness plane is always symmetric with respect to the surface normal direction.

Fig. 2.22 shows the test sample and a 0.6 mm pitch 64-element PA transducer. Fig. 2.23 shows the ray tracing model for measuring the velocities through SPA data acquisition. This backwall reflection technique uses the 64-element PA transducer in direct contact with the CFRP sample to be inspected. During data acquisition the information from the 1 x N shot is useful for obtaining the group velocities. The angle of propagation between the sender (which is the first element here) and all the remaining elements is measured as follows:

Let $x_{i,0}$ be the coordinates of the sender and $x_{j,0}$ the coordinates of the receivers.

$\left\{\frac{1}{2}(x_i + x_j), d\right\}$ is the backwall reflection point at thickness d of the CFRP sample. Therefore, the angle of propagation of the backwall reflection rays with respect to the z direction can be given as follows:

$$\theta_i = \theta_j = \tan^{-1}\frac{|x_i - x_j|}{2d} \qquad 2.21$$

Thus, the angle of propagation θ_i can be calculated for the sender and the receivers. This is stored in the form of a vector.

The velocities with respect to this propagation angle can be calculated from the travel times stored for the sender and receiver combination in the information matrix. Let the travel time between sender and receivers be t_{ij}, then the velocity is:

$$V_{ij} = \frac{\sqrt{(x_i - x_j)^2 + 4d^2}}{t_{ij}} \qquad 2.22$$

Hence, for each propagation angle the velocity is calculated and stored in the form of a vector. The results are filled as shown in the following Table 2.1:

Sender-Receiver	Angle of propagation θ_{ij}	Travel time	Velocity
1-2	-	-	-
1-3	-	-	-
⋮			
1-64	-	-	-

Table 2.1 Storing of velocities w.r.t. sender-receivers using backwall reflection

The maximum angle of propagation for a 64-element PA transducer with 0.6 mm pitch is 36.5^0 for a 25.4 mm thick CFRP sample. The number of propagation angles depends on the thickness of the sample. The lower the thickness the higher is the angle of propagation measured for a similar transducer configuration.

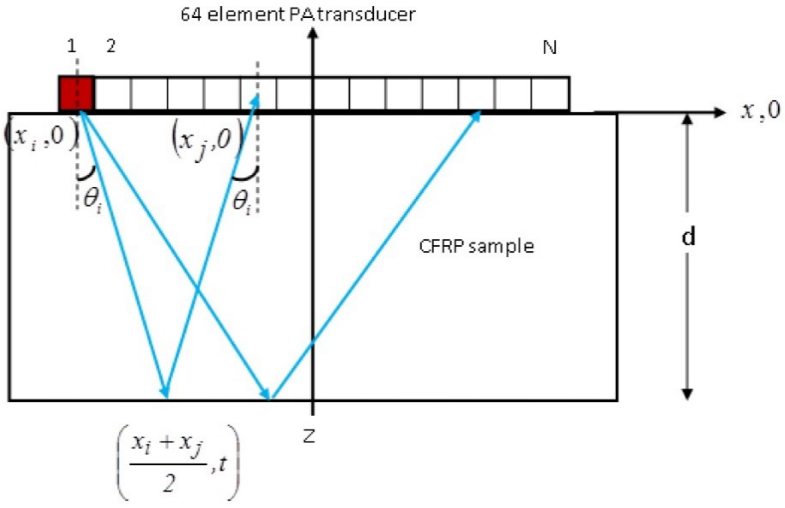

Figure 2.22 Backwall reflection method for measuring velocities experimentally

A ray tracing routine has been written in MATLAB for calculating the propagation angles and the corresponding velocities. Once the velocities for all different propagations are calculated they are interpolated for each angular step using a cubic interpolation, which is done using the MATLAB tool.

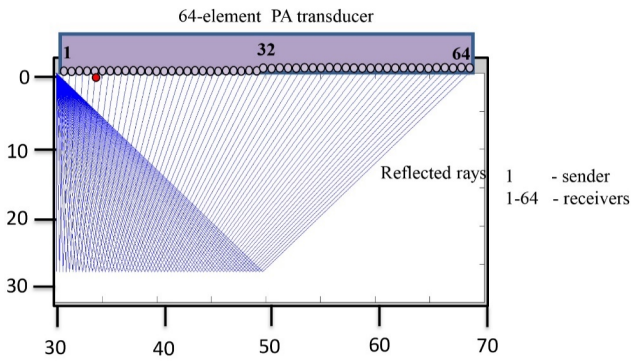

Figure 2.23 Ray tracing between all the elements and sender

2.7 Reverse Phase Matching (RPM)

2.7.1 The Principle of RPM

The hardware platform of the SPA method allows one to use the acquired data stored in the form of the information matrix (Bulavinov, et al., 2008), (Sridaran Venkat, Bulavinov, Pudovikov, & Boller, 2010). Travel time computation is the important step in the reconstruction process in which the travel time between a point in the inspection volume and the transducer element is computed as explained in the previous section 2.5.2. The elementary wave phase information, which is accessible with SPA through the information matrix, can be adjusted as per the anisotropic property of the material. The travel time associated with this anisotropic medium basically derived from the stiffness matrix is calculated with the help of the ray tracing method. This technique is called "Reverse Phase Matching" (RPM).

The hardware in the SPA method gives the user the possibility to access all the individual A-scans that are acquired during the inspection. For example, a working sequence of a 16-element phased array transducer in the SPA method will result in 256 A-scans (16 x 16). The phase information of these A-scans can be adjusted in such a way that the anisotropy of the CFRP material is considered for SAFT image reconstruction. Due to symmetrical properties, the number of elastic constants is reduced to 21 independent elastic constants for the anisotropic medium but it is even reduced to five independent elastic constants for the case of a transversely isotropic medium.

2.7.2 Implementation of RPM for Transversely Isotropic Medium through Ray Tracing

The behaviour of anisotropic media simulated through wave propagation considering ray tracing has been reported in various publications. A three-dimensional computerised ray tracing model for example has been described in (Schmitz & Walte, 1999) and (Ogilvy, 1986) for analysing the effects of beam profile distortion and ray path bending in austenitic welds. Basically, these ray tracing tools are useful in identifying the regions of sound propagation. To model ultrasonic waves in an anisotropic material through ray tracing one needs to solve the anisotropic elastic wave equation (Rose , 2004) and assume the plane wave solution to the wave equation. Hence, for any given phase velocity direction there are three solutions corresponding to the three different modes. For each of these modes there is an associated group velocity, which in general - unlike in an isotropic region - is not equal or parallel to the phase velocity. The associated group velocity direction and magnitude can then be calculated from the known phase velocity direction. For a given set of elastic constants and phase angle one uses an exact expression (Equations 2.17 to 2.19) for finding the phase velocity as described in the section 2.6.1. Once the phase velocity is known, the group velocity can be calculated using (Equation 2.15). Once the phase velocity, group angle and group velocity are computed, they are tabulated in the following vector form:

Phase angle (θ)	Elastic constants	Phase velocity	Group angle (Ø)	Group Velocity
0°	C_{11}, C_{13}, C_{33}, C_{44}, C_{66}	-	-	
90°		-	-	
⋮				
360°		-	-	

Table 2.2 Example for parameters to be calculated represented in vector form

The principle of the RPM algorithm is shown as a flow chart in Fig. 2.24. The algorithm takes the input of elastic constants measured through the backwall reflection method of the anisotropic medium and computes group velocities for the respective group angles. The travel time is computed using the group velocities mentioned in the Table 2.2 through the ray tracing and thus stored in the form of LUT. During the SAFT reconstruction, the

data from the information matrix is picked up for the corresponding travel time in the LUT and the final output is presented as a sectorial scan image.

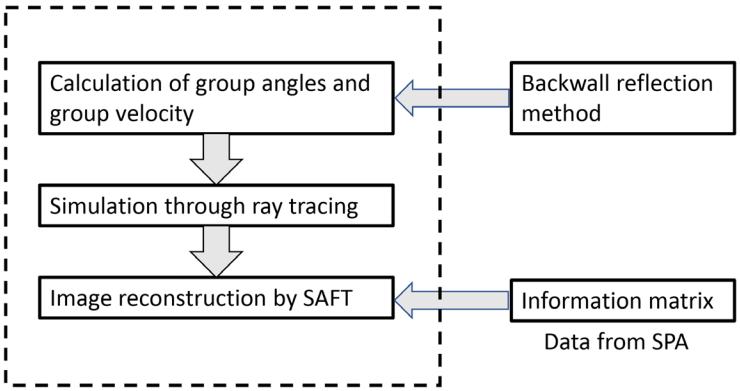

Figure 2.24 Implementation of Reverse Phase Matching method in SPA

2.8 Hardware

2.8.1 Hardware Platform

The SPA hardware is shown in Fig. 2.25. There is a slot for connecting the phased array transducer into the hardware. The architecture inside the hardware is shown in Fig. 2.26, the whole unit consists of the following:

1. Ultrasonic frontend electronics
2. Multiplexer module
3. Coordinate interface connected with manipulator
4. Serial optical interface
5. Personal computer

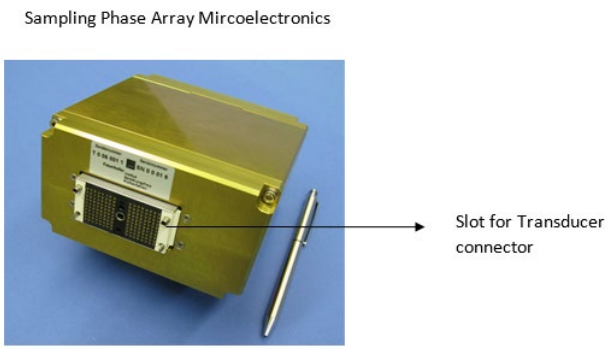

Figure 2.25 SPA system (Bulavinov, et al., 2008)

The front-end electronics has the following modules:

1. Coordinate interface

2. Manipulator

3. Optus 64 channel micro-electronics.

The test and analysis station has the following modules:

4. Optical link

5. PC module

6. Ultrasonic – client

7. US (Ultrasonic) data analysis.

The main function of the manipulator is to control the transducer movement which is in x, y and the z axes respectively. The positional information of the transducer from the manipulator is sent to the PC through the coordinate interface. The data for each shot of SPA information, which is acquired during the transducer movement, is sent back to the PC through an optical interface, which transfers data at the rate of 1.6 GBits/s. The software through which the manipulator parameters and ultrasonic parameters are controlled is installed in the computer. When the data is acquired, it is displayed as a reconstructed image using the interface software for the purpose of analysing the acquired image and can be converted for analysing the data both in the online and in the offline modes.

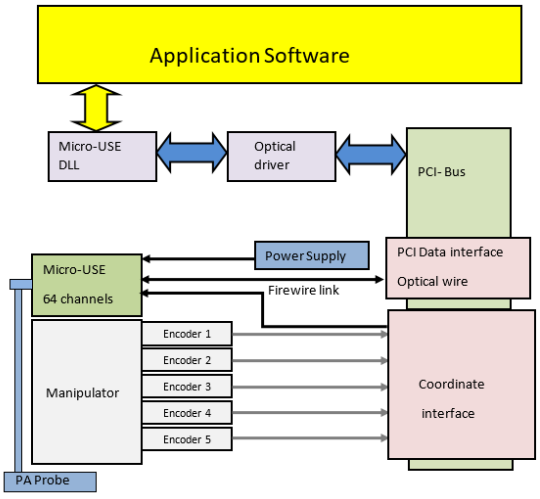

Figure 2.26 Architecture of SPA system (Bulavinov, et al., 2008)

The hardware module along with the immersion testing tank is shown in Fig. 2.27.

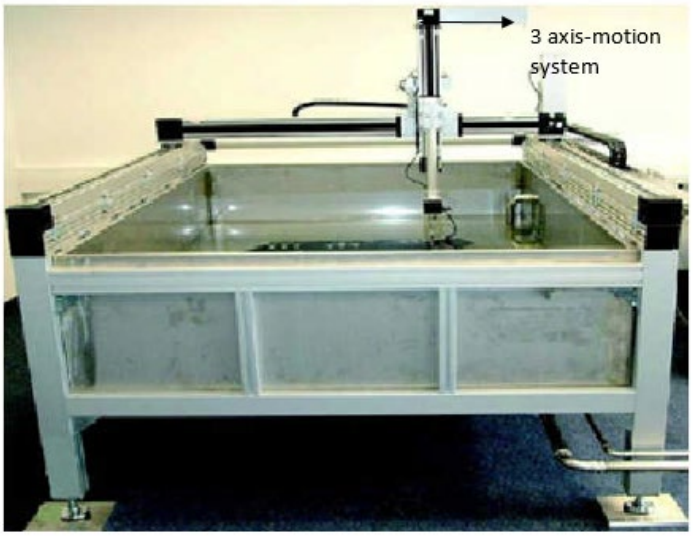

Figure 2.27 SPA electronics along with immersion tank and scanning systems

The main module in the frontend electronics is called Optus, which is a 64-channel ultrasonic system. The function of the multiplexer arises when the number of elements is more than the number of channels.

2.8.2 Measurement Procedure for SPA

The SPA measurement procedure is sequenced as follows:

1. The samples are dimensionally checked and loaded into the immersion tank with suitable supports.
2. Selection of transducer and frequency: Most of the samples are ranging from 3 to 20 mm in thickness so a high frequency of 5 MHz and 16- element phased array transducer having 0.60 mm pitch is selected for the experiment.
3. Calibration and range setting are done on the specimen with known thickness and known material properties.
4. TGC (Time Gain Correction): The sound attenuates with increasing depth and so one needs to compensate for its loss due to attenuation, which is achieved by plotting TGC. There is an option available in the user interface software for plotting TGC. Their corresponding values are then entered back to the user interface software. Fig. 2.28 shows the TGC curve obtained from a CFRP test sample (calibration sample), which has different thicknesses.

5. Selection of view: In general B-scan (cross-sectional), C-scan (top) and 3D views are chosen for viewing the acquired data.
6. Selection of resolution: Resolution of all three axes x, y and z is selected based on the range of inspection and computer memory consumption.
7. If the immersion method is used, the water path distance needs to be selected. Once all the details are entered, a suitable scanning speed is selected for both x-axis (scanning axis) and the y-axis (index axis).

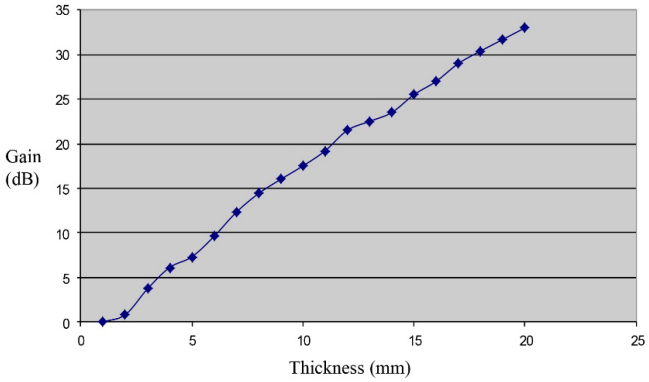

Figure 2.28 Time gain compensation curve

2.9 Experimental Validation

The CFRP specimen is assumed to be a unidirectional laminate having 5 independent elastic constants and has a flat bottom hole as a reference reflector as shown in Fig. 2.29. The elastic constants are calculated either by backwall reflection method or by using the numerical search algorithm which will be discussed in Chapter 5. The elastic constants and properties are shown in the table below:

Elastic constants	Value in GPa	Other properties
C_{11}	158.1	**Density** 1600 g/cm^3
C_{22}	7.0	
C_{33}	13.0	**Thickness** 25.0 mm
C_{44}	3.0	
C_{55}	6.8	**Reflector** FBH- Ø1 x 3 mm deep

Table 2.3 CFRP material properties

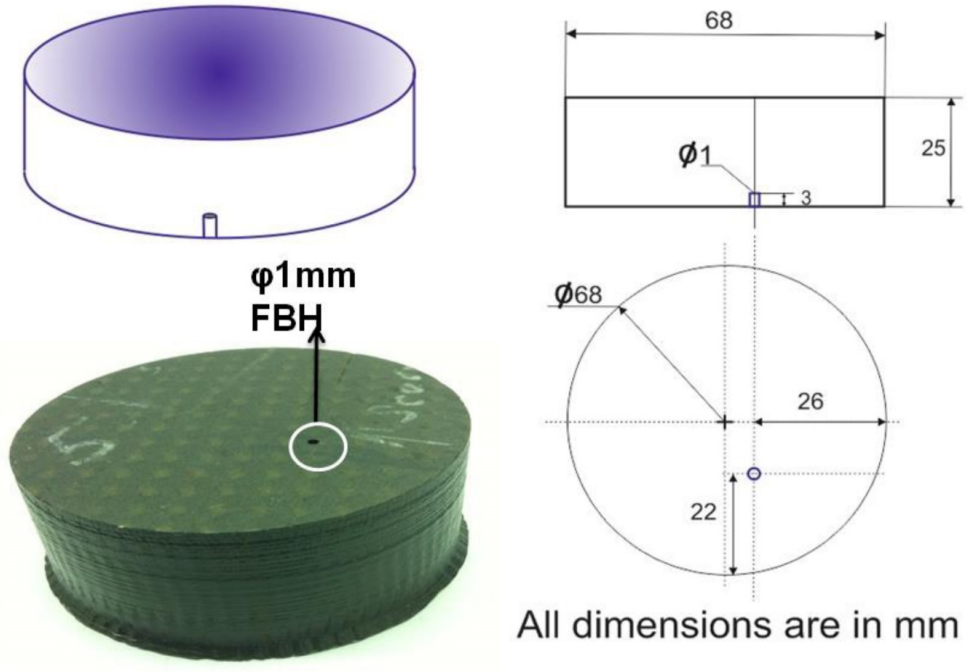

Figure 2.29 Test sample with location of flat bottom hole

The test sample along with the 16-element phased array transducer is shown in Fig. 2.30. The dimensions of the transducer are shown in Table 2.4.

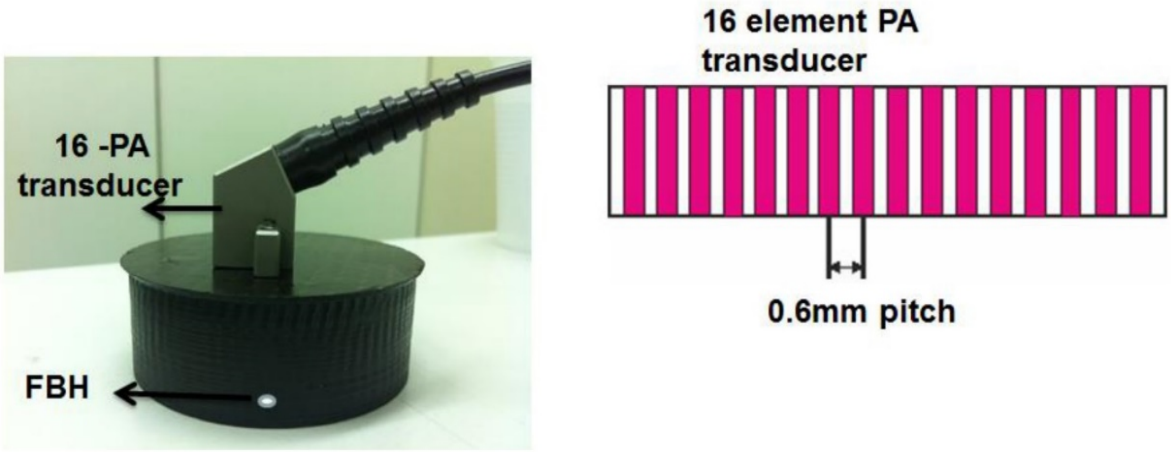

Figure 2.30 Test sample with PA transducer

Transducer parameters	Value
Number of elements	16
Pitch	0.60 mm
Active aperture	9.6 mm
Wedge	No wedge
Manufacturer	Olympus

Table 2.4 Phased array transducer parameters

The images reconstructed as sectorial scans are shown in Fig. 2.31 (a, b and c). The difference between the reconstructed images for the anisotropic medium with and without phase corrections (anisotropic corrections) is shown in Fig. 2.31. However, the accuracy of the result depends on the estimated elastic coefficients of that medium. One must therefore have the prior knowledge of the stiffness matrix before the ray tracing simulation is done. If this knowledge of stiffness matrix is not known, then the elastic constants have to be obtained through experimental methods or any other means (numerical search algorithm).

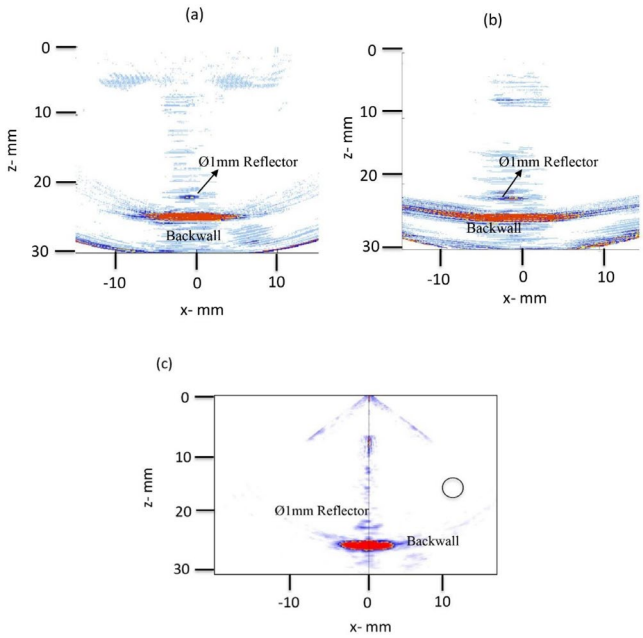

Figure 2.31 S- scan comparison on the same gain level for the CFRP Test sample of (a) SPA without anisotropic correction; (b) RPM; and (c) CPA

Chapter 3

Non-linear Acoustics for Damage Assessment

So far, it has been described how to characterise the damages in anisotropic materials in off-line or under no-load conditions using SPA and RPM. Another option in characterising materials and structures regarding their damage condition is to take advantage of their vibrational behaviour. Vibrations based health monitoring methods are interesting topics and have been discussed for many decades. An overview of the various vibrational-based methods for structural health monitoring is well described in (Fritzen, 2005), (Fritzen, 2005(a)) and (Guechaichia, 2011). Model based damage detection to know the location and the extent of the damage from the measured vibrational test data is described in (Fritzen, 1998). One can broadly classify the SHM methods as global and local SHM (Gopalakrishnan, 2011). This classification is based on the wavelength of the test signals with respect to defect size, as well as to the overall dimensions of the structure to be monitored. Local methods use high frequency ultrasonic waves whose wavelength should be less than the smallest size of the defect to be detected within the structure. What has been discussed in the previous chapter regarding SPA is the local method. In contrast, global methods use lower frequency modes of the structure where the indication of damage can be related to the presence of a defect anywhere within the structure. A local reduction in stiffness affects the natural frequencies, and in principle can be detected by a single sensor mounted on the structure. Usually, in most of the vibrational studies, natural frequencies are used as damage indicators. The variation in the mode shapes can be compared with reference mode shapes to identify the presence of damages. In this chapter, non-linear based vibrational analysis is studied for a composite specimen under a three-point bending load. As the operating frequency has been up to 20 kHz, which is in the beginning of the ultrasonic range, it is called VHCF (Very High Cycle Fatigue). Under such a condition, acoustics based non-linear analysis can be considered and is therefore discussed in this chapter with the aid of FEM modelling, various frequency domain methods and damage index analysis. Towards the end of the chapter, an inverse approach developed to localise the damage will be presented.

3.1 Contact Acoustic Nonlinearity (CAN)

Early identification of damages is one of the important issues in structural integrity assessment. Most of the methods available in this field are based on linear analysis. A more realistic description of the damage requires the physical understanding of the effect of the damage on the dynamic behaviour of the structure. One such behaviour is being observed when the damage interacts with the acoustic wave field that exhibits complicated material (e.g. nonlinear elasticity) and geometrical nonlinear behaviour (e.g. contact and friction). When elastic waves with large amplitudes are incident to the imperfect interfaces of a damage such as due to contact and friction it is called contact acoustic nonlinearity (CAN). As a result, the most interesting and common nonlinear feature being generated is higher harmonics in the structural response. Other nonlinear features include sub-harmonics, waveform distortions, shift in the natural frequency, coherence functions and signal modulation etc.

Many non-classical non-linearity cases have been reported in various references (Solodov, Krohn, & Busse, 2002), (Frouin, Matikas, Na, & Sathish, 1999), (Helfen, 2014), (Ooijevaar, 2014.), (Rabe, et al., 2012), (Shen, 2013), (Meo & Zumpano, 2005), (Jhang, 2009) and (Cantrell & Yost, 2001). The acoustic vibro-modulation method has been used to demonstrate the non-linear behaviour of the opening and closing action of cracks as shown in Fig 3.1 as an example for CAN. This method is otherwise known as nonlinear wave modulation spectroscopy (NWMS) because it uses both low frequency and high frequency excitation to study the non-linear feature due to the presence of the opening/closing of cracks. In this method, a low frequency vibration is applied to the material, which can generate tension and compression forces in the material that eventually causes the cracks to open in the tension phase and close in the compression phase. In parallel a high frequency excitation, which is in the ultrasonic range is applied to the material. During the tension or dilatation phase the high frequency signal is decoupled as shown in Fig. 3.2 due to the opening of the crack. This phenomenon also reduces the amplitude of the signal but during compression, where the crack is closed and does not interrupt with the high frequency signals. Representation of the time domain signals to frequency domain indicates that two new frequency components exist due to the opening action of the

crack under vibration. The two other frequency components correspond to the input frequencies.

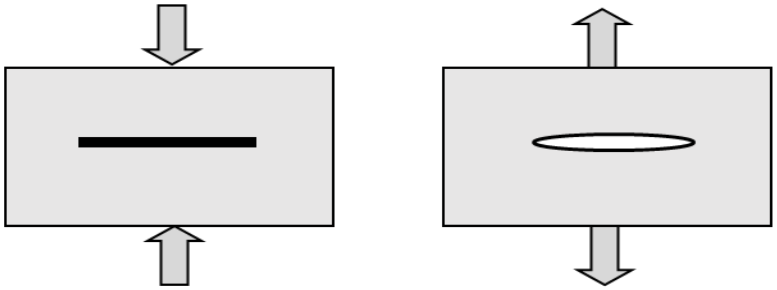

Figure 3.1 Closing and opening action of crack due to loading

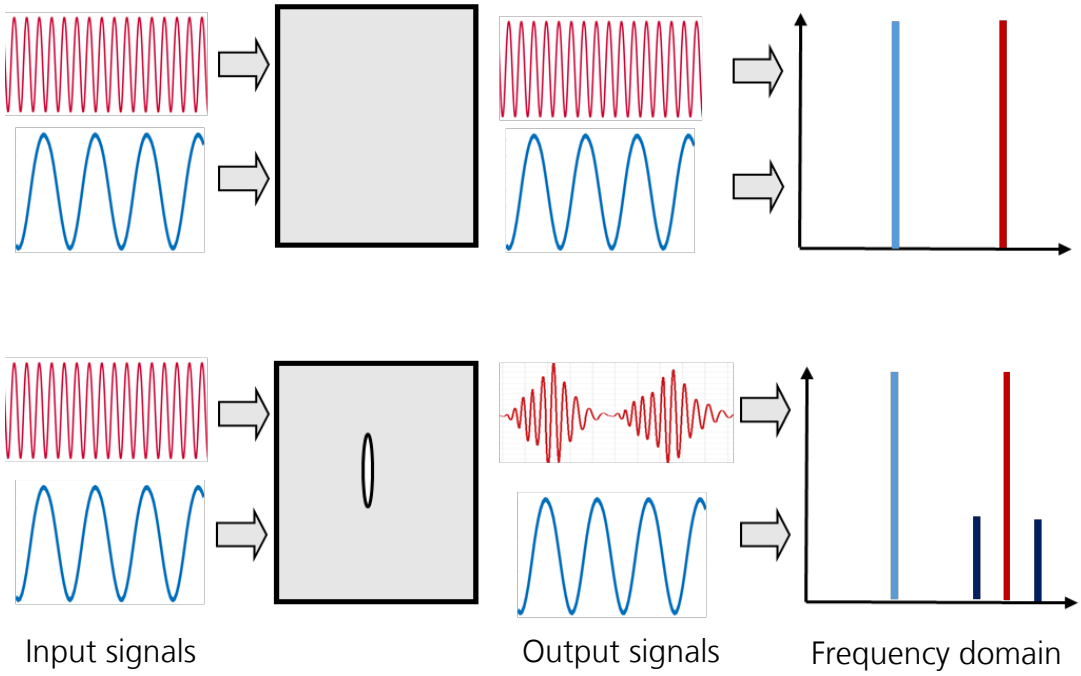

Figure 3.2 Illustration of the nonlinear acoustic vibro-modulation

3.1.1 Central Frequency Shift

(Meo & Zumpano, 2005) used the Nonlinear Elastic Wave Spectroscopy (NEWS) to study the effect of impact damage in CFRP composites. The performance of CFRP has been greatly influenced by impact damages and ageing phenomena. Impact damages may cause a significant amount of delamination even though the surface of the impact shows very minor indentation. Such a type of impact damage is called a BVID (Barely Visible Impact Damage) and can cause a greater amount of material degradation. If the damaged

structure is subjected to high compressive loading, buckling failure may occur. It is well understood that non-linear effects are having strong links with the micro-structural behaviour of the material and in any case such a nonlinear analysis accompanying elastic wave propagation can find those incipient damages much earlier than the linear analysis which depends on linear parameters such as propagation velocity, attenuation and elastic moduli. In one of the studies, the relative frequency shift as a function of load amplitude can be used to provide an indication of the presence of damage. Fig. 3.3 (a) shows the results of the reference specimen and Fig. 3.3 (b) shows the shift in driving frequencies due to the specimen being damaged.

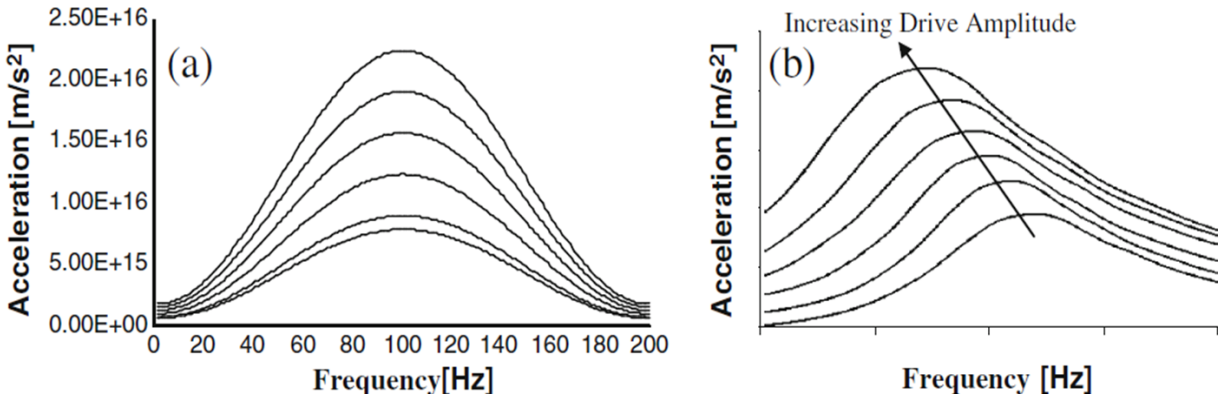

Figure 3.3 (a) Shift in fundamental frequency for the undamaged; and (b) Damaged CFRP- Nonlinear Elastic Wave Spectroscopy (Meo & Zumpano, 2005)

3.1.2 Higher Harmonic Generation

When the waveform of the incident wave is distorted by the nonlinear elastic response of the medium, higher harmonics are generated. The generation of the higher harmonic waves has been reported in (Frouin, Matikas, Na, & Sathish, 1999). Higher harmonics based on nonlinear ultrasonic analysis have been used for the estimation of the fracture toughness of CrMoV alloy grade steel. The basic principle of higher harmonic generation could be explained by means of nonlinear Hooke's law, which relates the stress-strain relationship by means of Young's modulus E and higher order nonlinear elastic coefficient β as follows:

$$\sigma = E\varepsilon(1 + \beta\varepsilon + \ldots) \qquad 3.1$$

Neglecting the attenuation effects the equation of motion of the longitudinal wave in the material can be represented by

$$\rho \frac{\partial^2 u}{\partial t^2} = \frac{\partial \sigma}{\partial x} \tag{3.2}$$

where ρ is the density of the solid, x is the propagation distance of the sound wave, u is the displacement and σ is the applied stress. With the help of Equations 3.1 and 3.2, one can obtain the relationship between strain and displacement and form the non-linear wave equation as given by:

$$\rho \frac{\partial^2 u}{\partial t^2} = E \frac{\partial^2 u}{\partial x^2} + 2E\beta \frac{\partial u}{\partial x} \frac{\partial^2 u}{\partial x^2} + .. \tag{3.3}$$

Perturbation is a theory applied to find the solution of the wave equation by assuming the displacement $u = u_0 + u'$, where u_0 and u' denote the initial wave and the first order perturbation solution respectively. If one sets u_0 to be a sinusoidal wave of single frequency, then:

$$u_0 = A_1 \cdot \cos(kx - \omega t) \tag{3.4}$$

The displacement u is then written as follows;

$$u = A_1 \cdot \cos(kx - \omega t) - A_2 \cdot \sin 2\,(kx - \omega t) \tag{3.5}$$

with

$$A_2 = \frac{\beta}{8} {A_1}^2 \cdot k^2 \cdot x \tag{3.6}$$

The second term in Equation 3.5 represents the second harmonic frequency component. As a result, one can explain how the second order harmonic waves of the amplitude A_2 occur through the propagation process of a nonlinear elastic solid. Equation 3.6 correlates the magnitude of the second harmonic frequency with the non-linear elastic coefficient β so if one can measure the magnitude of the coefficient, one can evaluate the degradation of the property due to ageing. From Equation 3.6 one can even define the ultrasonic nonlinearity parameter as follows:

$$\beta^* = \frac{\beta \cdot k^2 \cdot x}{8} = \frac{A_2}{{A_1}^2} \tag{3.7}$$

Many signal processing methods have been used to calculate the nonlinear parameter β^*. One such analysis has been illustrated for measuring β^* for increasing temperature of a CrMoV alloy steel. Fig. 3.4 (a) shows a good example of the dependence of the

nonlinear parameter on thermal ageing. The authors (Frouin, Matikas, Na, & Sathish, 1999) have extended their study to further calculate the correlation between the nonlinear parameter and the Fracture Appearance Transition Temperature (FATT) as can be seen from Fig. 3.4 (b). As the values in the x-axis are increased the FATT values in the y-axis also increase and then saturate.

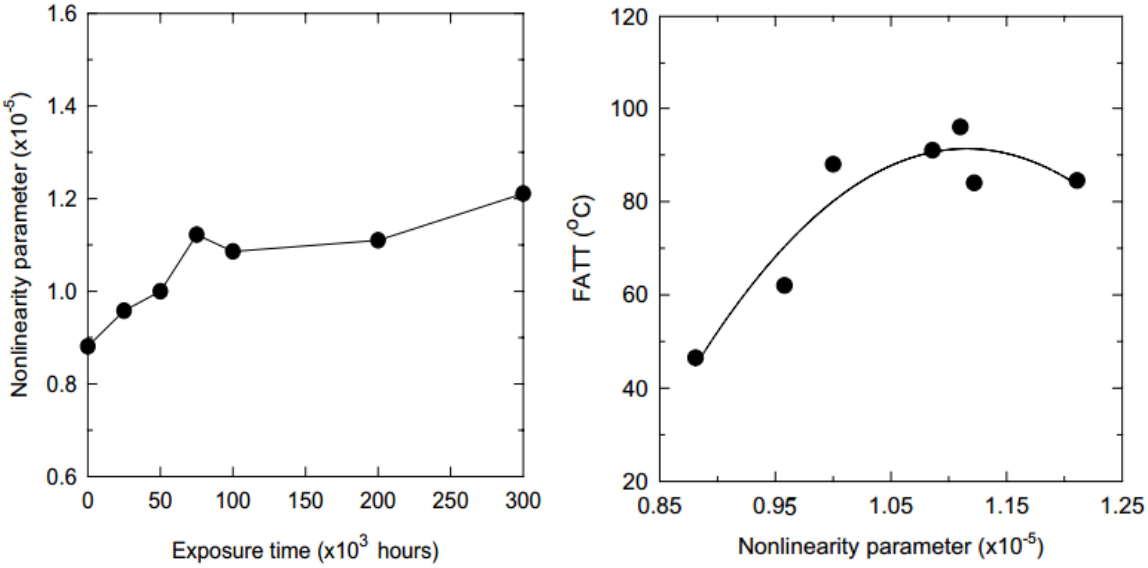

Figure 3.4 (a) Nonlinearity vs. thermal ageing; and (b) Nonlinearity vs. FATT (Frouin, Matikas, Na, & Sathish, 1999)

The relationship between physical parameters and the type of analysis to estimate the damage features (Ooijevaar, 2014.) is shown in Fig. 3.5. Nonlinearities and local change in the stiffness are closely integrated with the damage event and are defined as damage parameters. Usually those parameters are measured as force, velocity and displacement etc. over time and these variables are called the physical variables. Frequency domain and modal domain in the outer shell are the mathematical transformation of the physical parameters for useful analysis.

3.1.3 Waveform Distortions

Another interesting and relevant research study was published by (Ooijevaar, 2014.) on studying the nonlinear dynamic behaviour of a skin-stiffener structure due to impact damage where interaction between the damage and the dynamic deformation of the structure was analysed by applying a single tone harmonic excitation signal. A shaker had

been used to induce vibration into the structure with the excitation frequency matching the fourth bending mode and with five different excitation amplitudes. Velocity and acceleration responses were measured for a pristine and damaged structure as shown in Fig. 3.6.

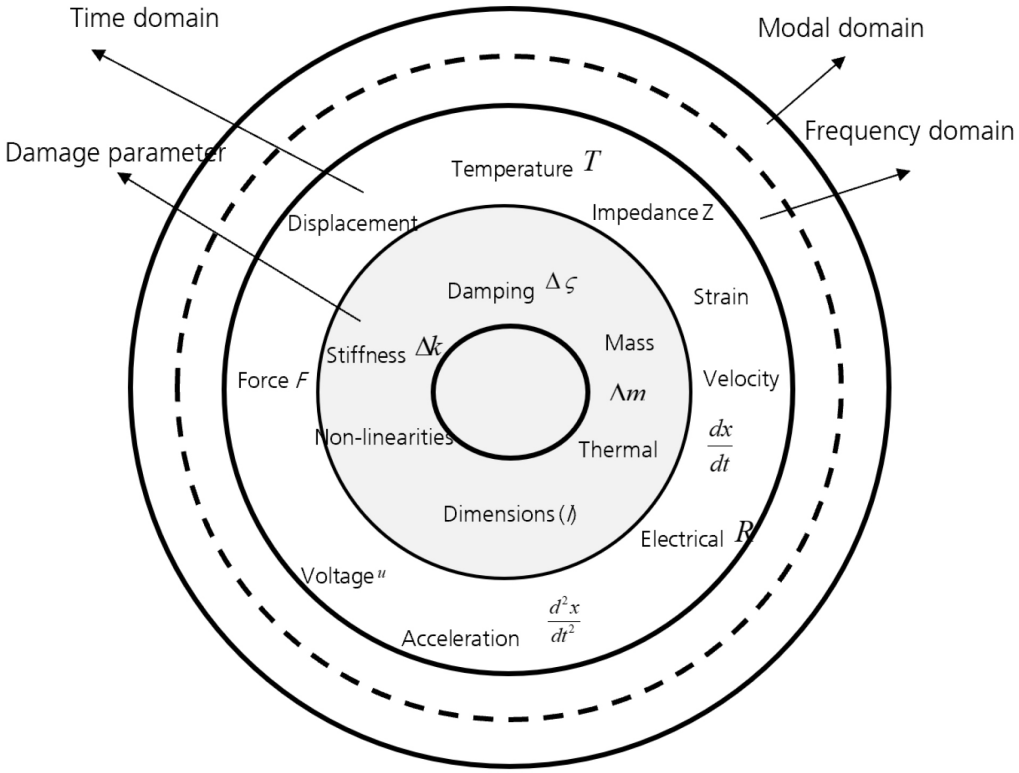

Figure 3.5 Classification of the damage features according to the information condensation

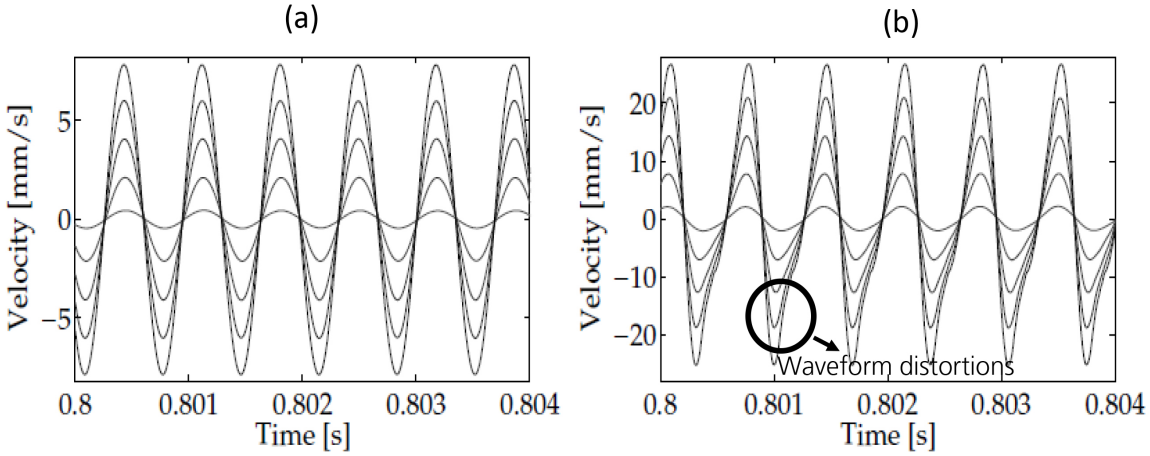

Figure 3.6 (a) Velocity response signals for pristine; and (b) Velocity response signals on damaged specimen (Ooijevaar, 2014.)

The measurement point is located near a skin-stiffener connection considered for monitoring. Fig. 3.6 (b) shows the waveform distortions for the damaged conditions but for the pristine conditions the harmonic oscillations are pure for all the five excitation amplitudes as shown in Fig. 3.6 (a). The more predominant results in the waveform distortions could be achieved by means of acceleration responses as shown in Fig. 3.7 below.

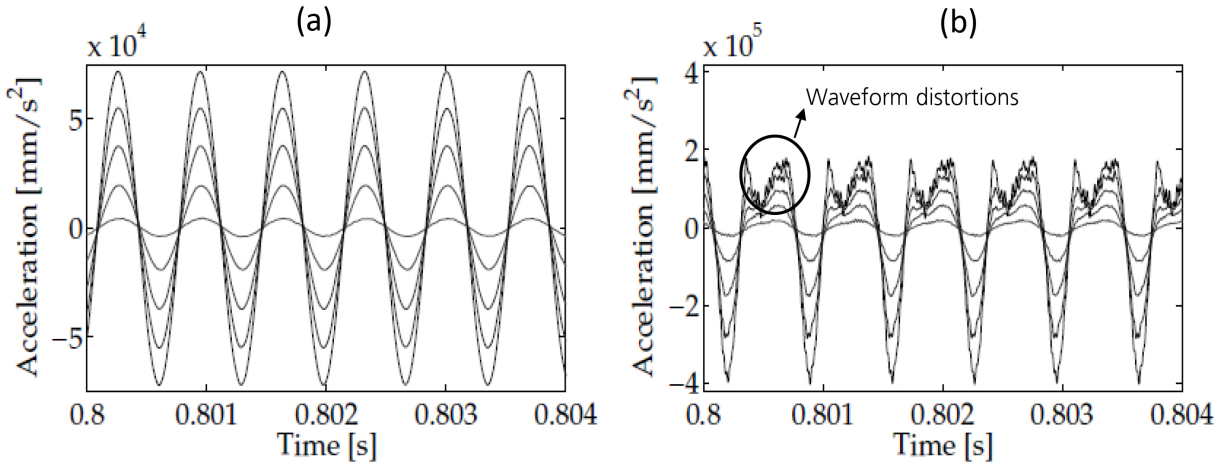

Figure 3.7 (a) Acceleration response signals on pristine; and (b) Acceleration response signals on damaged specimen (Ooijevaar, 2014.)

3.2 VHCF Experimental Setup

Very High Cycle Fatigue (VHCF) testing means that a component under fatigue loading is subjected to more than 10^7 cycles. In the entire lifespan, CFRP components can be subjected to variable loading conditions, which may go beyond 10^8 cycles. To understand the fatigue behaviour of CFRP materials under such service loading cycles, reference needs to be made to a laboratory level test where a VHCF test is run on a hydraulic driven traditional fatigue testing machine operating at a frequency of 5 Hz. Under such conditions, it would normally take approximately 6 to 7 years to get the test completed (Backe, et al., 2012), (Backe & Balle, 2016) and (Balle, 2013). In a collaborative project with the Institute of Materials Science and Engineering (WKK) at the University of Kaiserslautern a three-point bending apparatus has been built for demonstrating VHCF on CFRP components. The frequency range of 20 kHz has been chosen to facilitate both VHCF operation and then ultrasonic non-destructive evaluation under fatigue testing.

Non-destructive testing methods such as conventional ultrasonics, computer tomography and active thermography have been used to monitor the condition of the samples before and after the fatigue experiments. The nonlinear aspects of the damaging process have been identified using different signal processing methods such as Fast Fourier Transformation (FFT), Hilbert-Huang Transformation (HHT) and Short Time Fourier Transformation (STFT) under VHCF and correlated to the results with different NDT techniques (Helfen, 2014).

Fig. 3.8 shows the experimental setup of the ultrasonic fatigue testing system at WKK at the University of Kaiserslautern which comprises the loading device for the ultrasonic frequency of 20 kHz supported by two shoulders, an infrared camera, a laser vibrometry unit, a microphone and strain gauges near the shoulders for both online and offline monitoring of the CFRP under the VHCF regime.

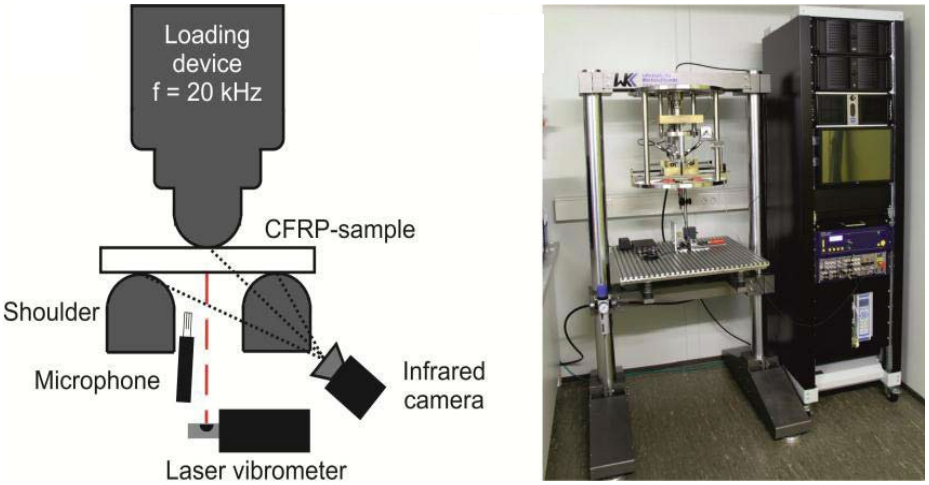

Figure 3.8 Three-point bending VHCF for CFRP (Backe, et al., 2012)

The strain distribution and the oscillation behaviour have been studied by using a 3D-Scanning Laser Doppler Vibrometer. The number of cycles defined in this VHCF regime is $N=10^9$ cycles. The experiments have been carried out in pulse and pause sequences to avoid excessive heat of the CFRP specimen under the cyclic loads. The infrared camera has been used to monitor the change in the temperature at the shoulders where the specimen is in contact with the loading device. The maximum increase of the specimen's surface temperature has been measured as 4° C during the ultrasonic pulses of 100 ms and has been measured for the undamaged specimens. The measured temperature was well below the glass transition temperature (Tg=90°C) of the CFRP-PPS material used.

The temperature distribution during the pulse-pause state was observed in the infrared camera as shown in Fig. 3.9. In addition to this the sample has been cooled with compressed air.

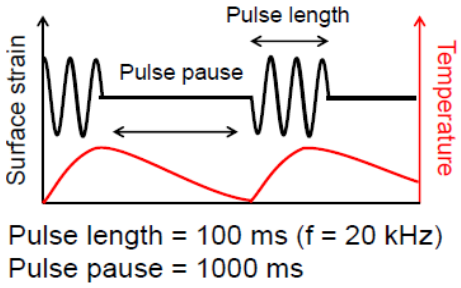

Figure 3.9 Temperature distribution during pulse-pause state during VHCF (Backe et al., 2012)

To control the sinusoidal oscillation as well as to measure the displacement amplitudes, a single spot LDV (Laser Doppler Vibrometry) has been used in every VHCF experiment for measuring the displacement amplitude from the surface vibration velocity of the sample. It measured the surface velocity quantitatively in one point of the CFRP sample to which the laser spot is focussed. A broadband microphone has been positioned between the shoulders to pick up the acoustical signal. The stiffness coefficients of the test sample as shown in Fig. 3.10 is given below:

$$\begin{pmatrix} c_{11} & c_{12} & c_{13} & 0 & 0 & 0 \\ c_{12} & c_{22} & c_{23} & 0 & 0 & 0 \\ c_{13} & c_{23} & c_{33} & 0 & 0 & 0 \\ 0 & 0 & 0 & c_{44} & 0 & 0 \\ 0 & 0 & 0 & 0 & c_{55} & 0 \\ 0 & 0 & 0 & 0 & 0 & c_{66} \end{pmatrix} \begin{pmatrix} 74.24 & 20.70 & 14.71 & 0 & 0 & 0 \\ 20.70 & 74.24 & 14.71 & 0 & 0 & 0 \\ 14.71 & 14.71 & 10.46 & 0 & 0 & 0 \\ 0 & 0 & 0 & 2.70 & 0 & 0 \\ 0 & 0 & 0 & 0 & 2.70 & 0 \\ 0 & 0 & 0 & 0 & 0 & 3.79 \end{pmatrix} [GPa]$$

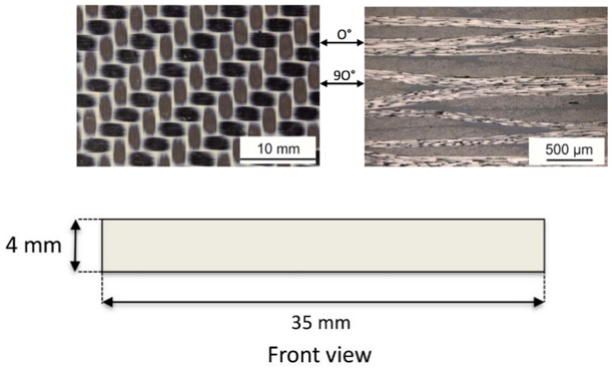

Figure 3.10 CFRP specimen used for non-linear analysis

Following the observations reported in (Backe & Balle, 2016) damages of the character of fiber-matrix-debonding and transversal cracking followed by micro, meta and macro delaminations have been observed which have been summarised under the expression of 'crack densities' and have been carefully analysed. Following this analysis it has been observed that fiber-matrix-debonding has been developed at the onset of fatigue loading while delaminations mainly emerged at 40% and beyond the specimen's fatigue life.

What damage is considered to be needs to be defined. Every material and specifically composite has voids or any other imperfections which are part of the material's pristine condition. To get a feeling of this behaviour some of the specimens were analysed using X-ray computed tomography with an X-ray energy of 60 kV and 150 µA as well as a voxel size of 9.5 µm without pre-filtering. 500 × 1600 × 1800 voxels of the field of view (FOV) comply with a volume of 4.800 × 15.200 × 17.100 µm (Sridaran Venkat, Starke, & Boller, 2018). Fig. 3.11 shows the results for the pristine and the damaged condition of a specimen. For the undamaged condition (Fig. 3.11 left) a large amount of micro-imperfections and micro-cracks can be observed, however, no delaminations, while for the damaged conditions delaminations have been identified (Fig. 3.11 right). Similar images (Fig. 3.12) have been obtained through ultrasonic scanning based on immersion testing with the Ø 25 mm transducer of 25 MHz centre frequency. It can be observed that different smaller delaminations seem to gradually merge having most likely started at different of the micro-imperfections observed in the pristine condition.

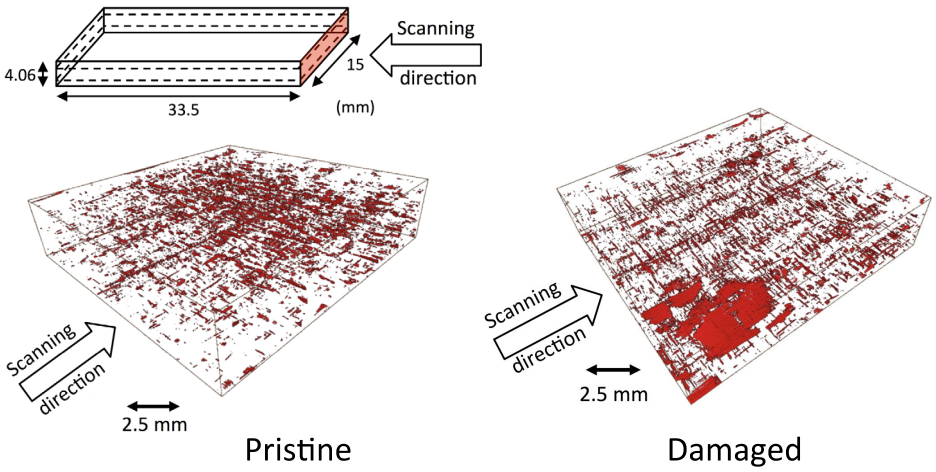

Figure 3.11 CT image of pristine composite specimen analysed (Sridaran Venkat, Starke, & Boller, 2018)

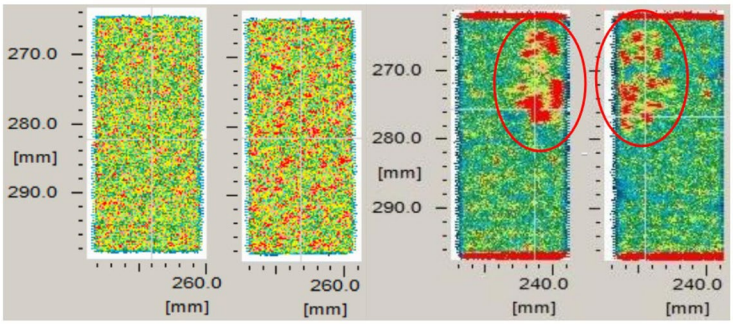

Figure 3.12 Ultrasonic scans taken from the top and bottom side of the specimen (Sridaran Venkat, Starke, & Boller, 2018)

3.3 Numerical Simulation of Composite Laminates Subjected to Three-Point Bending

FEM (Finite Element Method) simulations have been used for static and dynamic structural analysis for many decades. FEM discretizes the entire geometry into a number of elements connected by common nodes and solves for the variable displacement, while assuming proper interpolation or shape functions between the nodes. Micro level delamination imitated as breathing crack subjected to three-point bending load has been modelled using the FEM software COMSOL-Multiphysics (COMSOL-Multiphysics, 2016) that enhances the non-linear ultrasonic analysis. The 2D FEM model of the specimen under testing condition is given in Fig. 3.13 (a) and the meshed geometry is shown in Fig. 3.13 (b). The type of the mesh and its size strongly influence the solution. From the literature (Ghose & Balasubramaniam, 2011) it was found that a triangular mesh gives more accuracy for modelling delamination in composites.

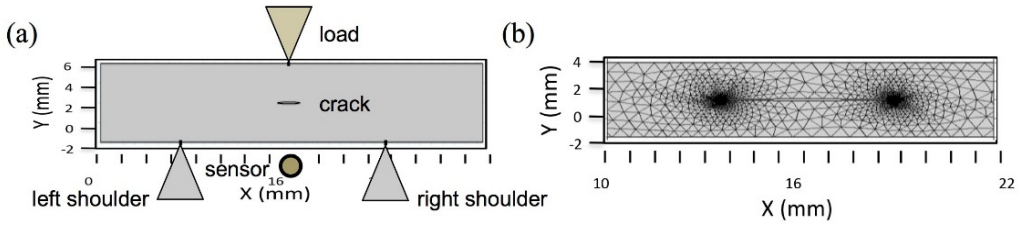

Figure 3.13 a) Model geometry and load conditions; and b) Meshed geometry from FEM simulation

In case of contact interfaces due to a breathing crack present in the model geometry as shown in Fig. 3.13 one introduces contact interactions between the elements (Shen, 2013). The contact problem between the interfaces is generally solved using the following two algorithms, which are built in COMSOL Multiphysics. These are:

1. Penalty method and
2. Augmented-Lagrangian algorithm (AL).

To simulate the breathing action in the delamination areas, a node to node contact between the interfaces has been defined such that the local stiffness matrix changes when the two interfaces come into contact (i.e. closing action under compressive loading).

The relationship between the strain and the displacement is obtained by the equation of motion (Equation 3.8):

$$\sigma_{i,j} + \rho f_i = \rho \ddot{u}_i \tag{3.8}$$

For the known elastic constants and by means of Hooke's law, the following constitutive relationship is established between strain and the displacements, and is implemented in the COMSOL structural mechanic's module (COMSOL-Multiphysics, 2016):

$$\varepsilon_{ij} = \frac{1}{2}\left(u_{i,j} + u_{j,i}\right) \tag{3.9}$$

where σ and ε are the Cauchy's stress and strain tensors, ρ is the density of the material and u is the displacement. The point load f is applied on the middle of the specimen, which is of the following form:

$$f = A \cdot \sin(\omega \cdot t) \tag{3.10}$$

where ω is the angular frequency, A is the amplitude of the load and t is the time. The prescribed displacements of u_x and u_y are defined at the shoulders to be zero to mean that they are fixed at their ends. A point probe, which is mentioned as a sensor point in Fig. 3.13(a) is defined to record the time history. A time dependent study in COMSOL FEM software was selected to solve the unknown displacement variable at every 2 μs interval. The delamination is modelled by using an ellipse "a" with the major axis being the length that varies from 1 to 6 mm and the minor axis being the crack opening of 0.05 mm. A contact pair boundary condition was selected on the delamination zone and as

mentioned before, an Augmented Lagrangian method was selected as contact pair (Auricchio & Sacco, 1996). They are mathematically defined as follows:

$$h(x) \leq 0 \tag{3.11}$$

$$t_N = -n(x) \cdot PN \geq 0 \tag{3.12}$$

$$t_{N(x)} \cdot h(x) = 0 \tag{3.13}$$

$$t_T = PN + t_N \cdot n = 0 \tag{3.14}$$

Equation 3.11 states the condition of impenetrability and the negative sign in Equation 3.12 means that the normal component of the traction on the surface should be compressive loading. Equation 3.13 is used to assume the frictionless contact between the contact pairs. Here h and P are the scalar-valued gauge function and the first Piola-Kirchoff stress tensor (Equation 3.14) respectively. N is the outward normal of the reference condition and n is the outward normal of the current configuration respectively. The results of the simulation described as y-displacement during the opening and closing action of the delamination at various times is shown in Fig. 3.14.

The data acquired during the VHCF experiment is the time domain signal recorded by the laser vibrometer, microphone and load sensors. Unlike the time domain signals from an ultrasonic linear measurement, the time domain signals in the non-linear analysis here does not show any presence of damage and it simply measures the amplitude in the y-axis at various intervals. This is shown in Fig. 3.15 for the pristine and the damaged condition as a comparison between experiment and simulation.

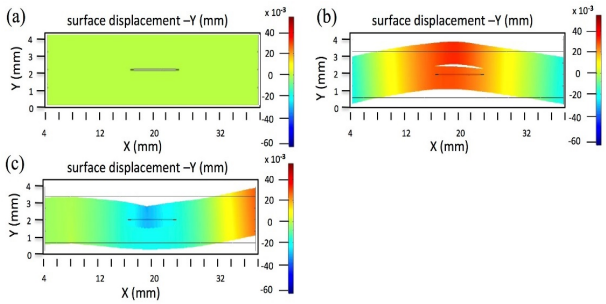

Figure 3.14 FEM simulation (a) Original state; (b) Opening of the crack; and (c) Closing of the crack

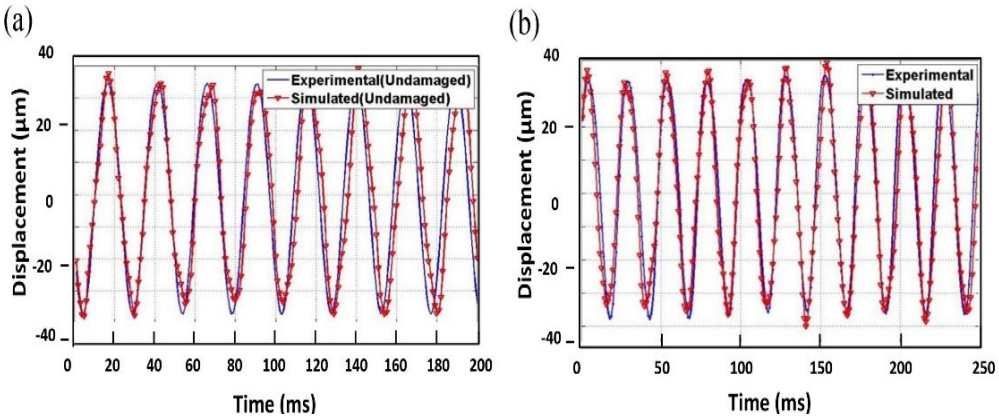

Figure 3.15 (a) Time domain signals of experiment and simulation for undamaged; and (b) Time domain signals of experiment and simulation for damaged specimen

3.4 Analysis of Experimental Data Using Signal Processing Methods

3.4.1 Fast Fourier Transformation (FFT)

The presence of damages in general affects the fundamental frequency, which is the excitation frequency 20 kHz in the specific case considered here. The information regarding the damage is therefore condensed in the time domain signals and it requires analysis in frequency domain to extract the condensed information, which is achieved by means of Fourier transformation or Fast Fourier Transformation (FFT). A Fourier transform is an operation that transforms a periodic time domain signal into frequency domain functions and in the result it describes the frequencies and their corresponding amplitudes present in the function. In the following discussion, the excitation function of the form as described by Equation 3.10 is taken to represent the signal $x(t)$ in discrete-time and plot the signal (time domain). This is shown in Fig 3.15 for the pristine and the damaged condition using both experimental and simulated data. Fourier transformation is defined as follows:

$$F(f) = \int_{-\infty}^{\infty} x(t) \, . \, e^{-i2\pi ft} dt \qquad 3.15$$

One can inverse the Fourier function in the frequency domain to represent the signal back in the time domain as shown in Equation 3.16. This is called the Inverse-Fourier transform.

$$\int_{-\infty}^{\infty} F(f).e^{i2\pi ft}df = x(t) \qquad 3.16$$

where *x(t)* is the time domain representation of the signal, *F(f)* is the frequency domain representation of the signal and i=$\sqrt{-1}$. FFT is an efficient method to calculate the Fourier transformation. The detailed formulation of the FFT algorithm can be referred to in (Kalyanasundaram & Baldev Raj, 2011). In the present case FFT is achieved by means of a MATLAB tool (MATLAB-User-manual, 2015). The FFT of the time-domain data for N=10^8 cycles is shown in Fig. 3.16.

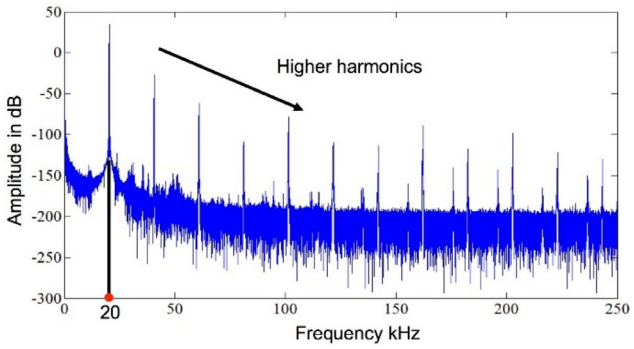

Figure 3.16 Frequency spectrum for a pristine condition of the experimental data at N=10^8 cycles

Fig. 3.17 (a) shows the frequency response of the two states: (1) pristine and (2) damaged conditions of the experimental data in a logarithmic scale. The first peak is the eigenfrequency (20 kHz) and the respective amplitudes of the higher harmonics are changed for the damaged condition taken at 1.35 x 10^8 cycles.

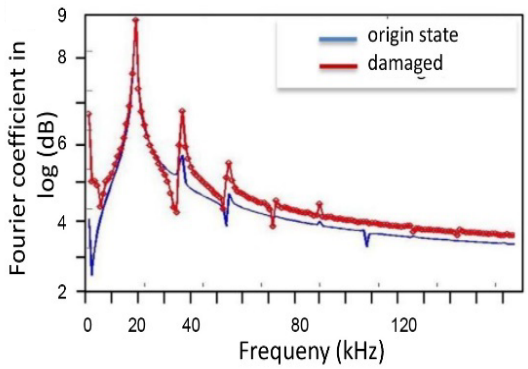

Figure 3.17 Comparison of the frequency spectrum for pristine and damaged condition of the experimental data

3.4.2 Short Time Fourier Transformation (STFT)

Fast Fourier Transformation (FFT) analysis yields the frequency spectrum of the time domain signals. However, after the transformation into the frequency domain, the phase information is lost. The main drawback of the FFT is that simultaneous time and frequency localisation is not possible. The procedure to get both time and frequency information is achieved by means of STFT. In the process, the longer time signal is divided into shorter segments/windows of equal length and FFT is computed separately on each segment. In STFT, windowing places a critical role usually where a Hanning window or a Gaussian window is used. In the end the frequency spectrum is plotted over the time intervals in 2D. Mathematically it can be written as follows (Equation 3.17):

$$STFT(t^*, u) = \int_t [f(t) \cdot W(t - t^*)] \cdot e^{-i2\pi ut} \qquad 3.17$$

STFT of $f(t)$ is computed for each window centred at $t = t^*$, W is the windowing function, t^* is the time index and u is the frequency index. The window selected should be narrow enough to ensure that the portion of the signal falling within the window is stationary. When the window is wide, the STFT gives good frequency resolution but poor time resolution and vice versa when the window is narrow. Fig. 3.18 (a) shows the STFT for N=10^6 and Fig. 3.18 (b) N=10^8 cycles. The higher harmonics in the spectrogram increases providing evidence of the non-linear response as the number of cycles reaches to 10^8 cycles.

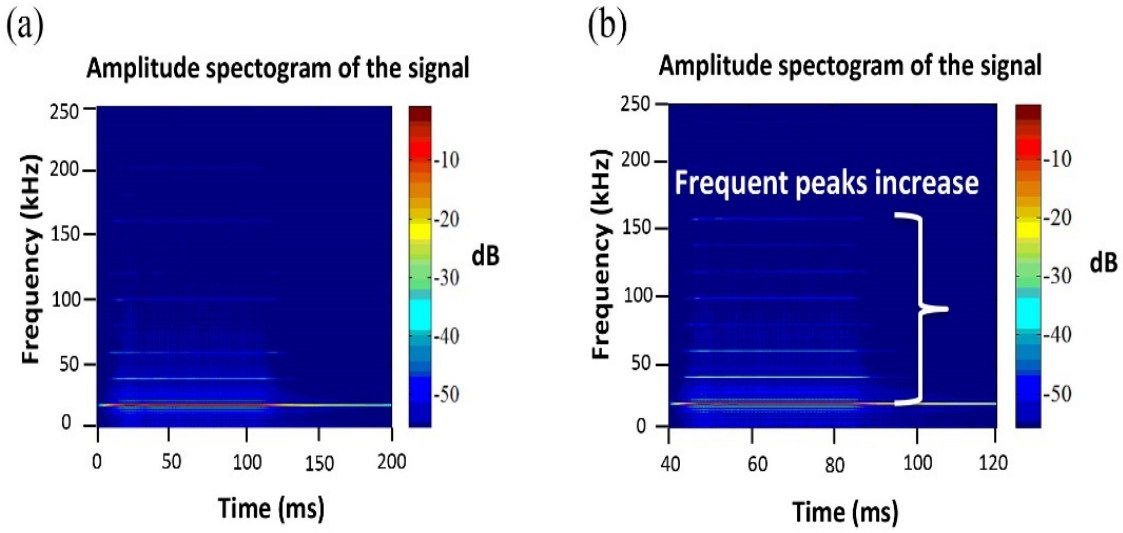

Figure 3.18 (a) STFT of 10^6 cycles; and (b) STFT of 10^8 cycles of experimental data

Alternative to the STFT is wavelets, which use multiple window sizes that are varying. However, in the present context, STFT analysis is used for analysing experimental data for various cycles.

3.4.3 Distortion Factor

In (Rabe, et al., 2012) the distortion factor was used as a measure to describe the non-linear behaviour of the material under VHCF for various numbers of fatigue cycles. Fig. 3.19 shows the number of fatigue cycles versus the distortion factor *(K)* in %. The formula shown in Equation 3.18 is used for computing K, where A_1, A_2, A_3 are the amplitudes of the higher harmonics of the frequency spectrum.

$$K[\%] = 100 \cdot \sqrt{\frac{{A_2}^2 + {A_3}^2 + \ldots}{{A_1}^2 + {A_2}^2 + ..}} \qquad 3.18$$

From Fig. 3.19 it becomes obvious that the distortion factor increases with the number of cycles but at around 2.2 x 10^8 and 3.2 x 10^8 cycles it exhibits some characteristic peaks which may be due to the cause of an opening and closing action of the micro-level delamination.

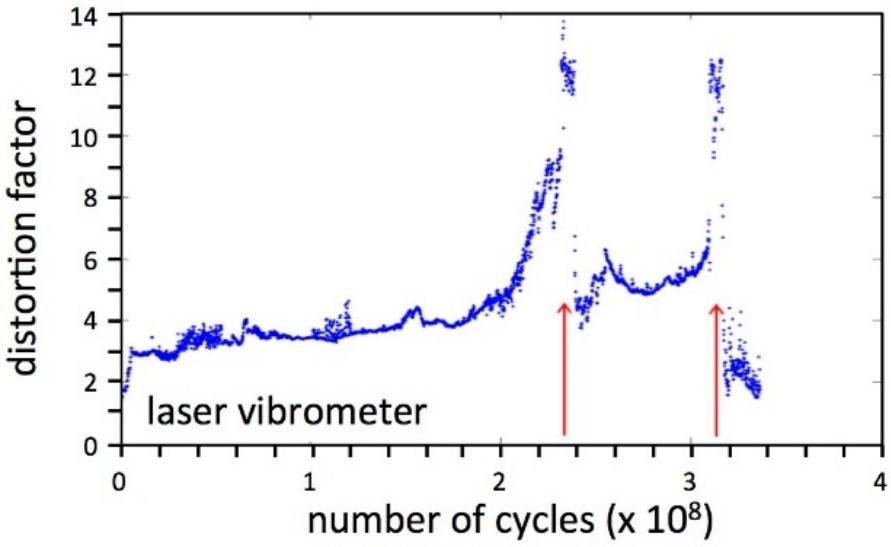

Figure 3.19 Distortion factor of the experimental data (Rabe, et al., 2012)

3.4.4 Damage Index Measures

Different types of damage indexes have been proposed for analysing the experimental data to measure the non-linear behaviour during the VHCF regime. These are summarised as follows:

Centre frequency shift

$$f_{central} = \frac{\sum_{i=1}^{N}[F(f_i) \cdot f_i]}{\sum_{i=1}^{N} F(f_i)} \quad 3.19$$

Energy coefficient of the frequency spectrum

$$E = \sum_{i=1}^{N} F(f_i) \quad 3.20$$

Correlation coefficients of the frequency spectrum

$$\gamma = \frac{\sum_{i=1}^{N} F_b(f_i) F_m \cdot (f_i)}{\sqrt{\sum_{i=1}^{N} F_b(f_i)^2 \cdot \sum_{i=1}^{N} F_m(f_i)^2}} \quad 3.21$$

Differential of the frequency spectrum

$$D = \sqrt{\frac{\sum_{i=1}^{N}[F_b(f_i) - F_m(f_i)]^2}{\sum_{i=1}^{N} F_b(f_i)^2}} \quad 3.22$$

Total distortion factor of the time domain signal

$$THD = \frac{\sqrt{\sum_{i=1}^{N} {A_i}^2}}{A_b} \quad 3.23$$

where $F(f_i)$ is the first harmonics and f_i are the frequencies of the corresponding higher harmonics. $F_m(f_i)$ is the frequency spectrum of the measured cycle and $F_b(fi)$ is the frequency spectrum of the baseline data. The coefficients A_i and A_b are the amplitudes of the time domain signals of the measured signal and the baseline signal. The output of the various damage indexes has been plotted as shown in Fig. 3.20. The shift from the central frequency and the correlation coefficient follow the similar trend i.e. downwards.

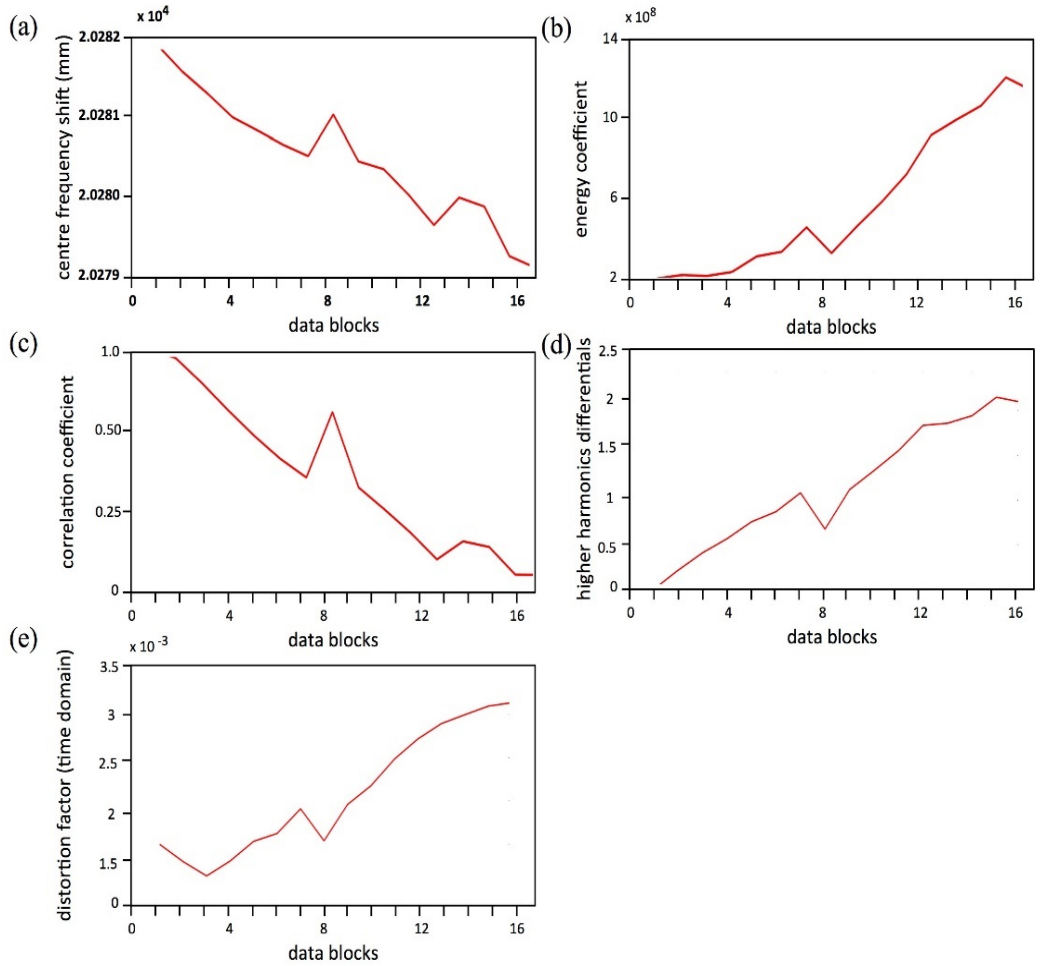

Figure 3.20 (a) Central frequency shift; (b) Energy coefficients of the frequency spectrum; (c) Correlation coefficient; (d) Differential harmonics of frequency spectrum; and (e) Total distortion factor of the time domain signal.

As the number of cycles is increased (higher number in the data blocks as shown in x-axis of Fig. 3.20(a)), the frequency components of the higher cycles deviate from the central frequency. Similarly, one can observe the correlation coefficient as shown in Fig. 3.20(c), if the correlation factor '1' means the difference between the frequency components of the two states (pristine and damaged) is zero and vice-versa when the correlation factor approaches to zero. In a similar way the energy, the differential factor and the total distortion factor (time-domain) increases when the number of cycles is increased.

Fig. 3.21 shows the damage index evaluation from Equations 3.21, 3.22 and 3.23 of the experimental data obtained from the load sensors on the shoulders in comparison to the LDV data as shown in Fig. 3.20. They follow the similar trend as seen before.

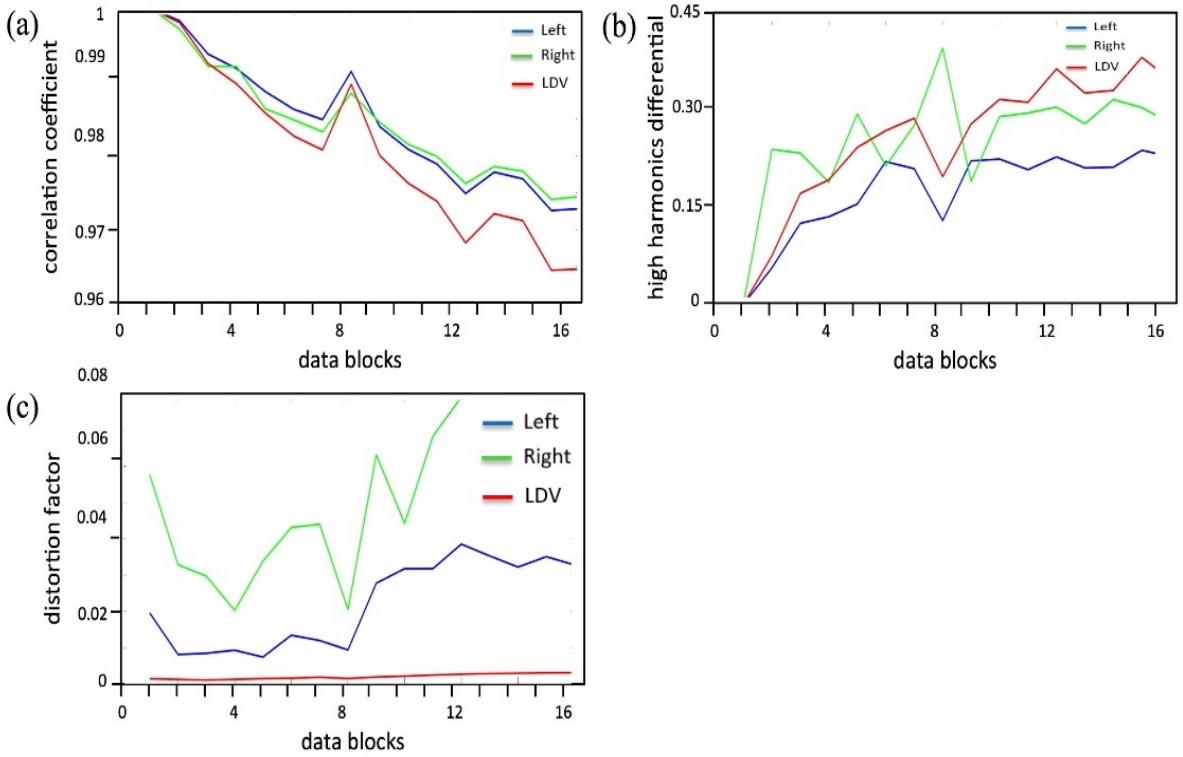

Figure 3.21 Comparison of LDV and load sensor data for the damage index: (a) Equation 3.21 (b) Equation 3.22; and (c) Equation 3.23

3.5 Analysis of Simulated and Experimental Results

Fig. 3.22 shows the simulated results for various delamination size ranges from 1 to 6 mm located in the centre of the specimen. When the damage size is increased, the amplitudes of the first harmonics are reduced, which is due to the change in the local stiffness at the delamination area. In a similar way, the presence of higher harmonics move from the higher towards a lower frequency when the damage increases. The results could be verified with acoustic resonance spectroscopy results discussed by (Meo & Zumpano, 2005). Fig. 3.23 shows the log scale comparison between experiment and simulated frequency domain signals. The difference in the second higher harmonics between experiment and simulated data is supported by the understanding that in reality there are numerous damages originating from the subjected CFRP specimen whereas, only one delamination was considered in the simulated model. The following are the assumptions considered for the numerical simulation:

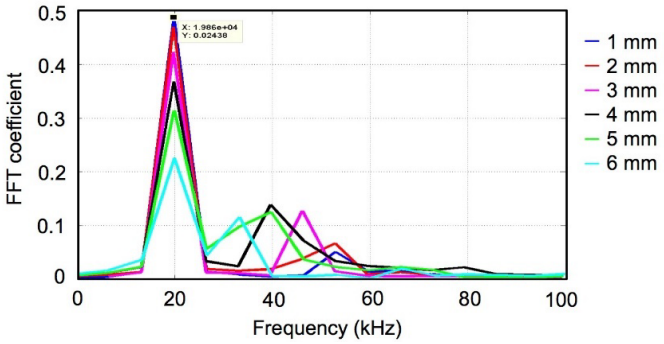

Figure 3.22 Frequency spectrum for various crack sizes when the delamination is at the center of the specimen as shown in Fig. 3.13.

1. Only one delamination is considered for the calculation of the frequency spectrum in the simulation model. However, there are multiple delamination sites that exist for such samples in reality.
2. Dynamic propagation of the damage is not considered. The delamination size is constant for all the time cycles in the simulation.
3. The experimental results are subject to mechanical and electronic noise, while simulation does not consider such noise.

The response from the simulation model at the pristine state and the damage state (1.35×10^8 cycles) has been compared to the experimental response obtained from the LDV. The generation of higher harmonics and the evaluation of damage indexes based on various signal processing methods confirm that the presence of micro level delamination can cause nonlinearity in the data obtained.

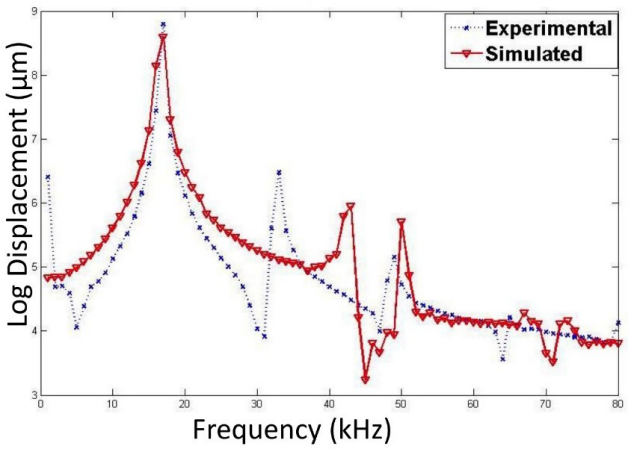

Figure 3.23 Comparison of frequency spectra between simulation and experiment

3.6 Inverse Approach of Characterising Damages Using Simulation

By repeating the simulation for various positions of the delamination a database has been formed to characterize damages using an inverse approach. The ratio of higher harmonics to the eigenfrequency forms the frequency function. The numerical interpolation function is then used with the help of MATLAB to obtain a statistical fit, which is shown in Fig. 3.24. From the analysis of the experimental data the frequency function can be estimated from the higher harmonics. By correlating the value of this function with the surface plot shown in Fig. 3.24(b) obtained from the simulation, the size and the location of the delamination can be found. The background of this work can be referred to in (Bagchi, Sridaran Venkat, Starke, Boller, & Mitra, 2015).

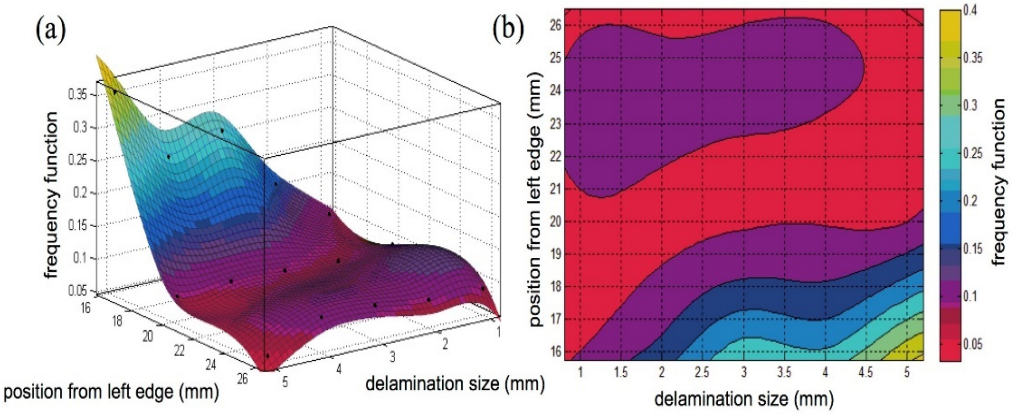

Figure 3.24 (a) Curve fitting for various crack sizes at different positions using MATLAB; and (b) Surface plot for the size and location of the delamination

The numerical studies show that the presence of breathing cracks or incumbent damages in the frequency domain exhibits higher harmonic peaks due to the opening/ closing action of the delamination. Numerical inversion mentioned in the current research proves to be an effective tool for prognostics and diagnostics of the non-linear acoustic behaviour in a composite structure. Such an approach can even be validated with non-destructive testing methods using ultrasonic and computed tomography for further quantitative evaluation.

How such an inverse approach can be generalised is shown in Fig. 3.25. The idea is for a damage tolerant structure a surface plot like the one shown in Fig. 3.24(b), which can be generated through simulation. This looks feasible for structures, which can be completely

exposed to vibrational modes even in the ultrasonic range. However, for structures, where only a portion can be excited, such as through an impact hammer, the description of the vibrational behaviour may be much more complicated but possibly not impossible. With such a surface plot available a structure could now be analysed considering a wideband actuation spectrum to excite the structure either globally or even locally and to analyse the frequency response function with respect to its modal characteristics serving as a characteristic to identify local damage resonances appropriately.

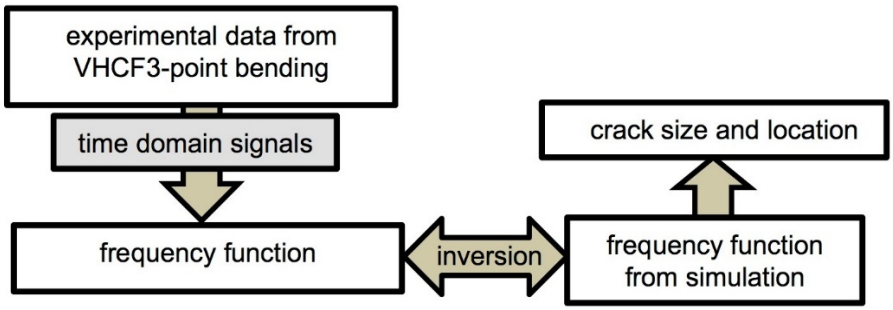

Figure 3.25 Damage quantification through inversion using simulation

Chapter 4

Guided Waves and their Relation to Structural Health Monitoring

4.1 Fundamentals of Guided Waves

When a wave propagates in an infinite medium where boundaries have no influence on the wave propagation the wave is called a bulk wave. In contrast, when it propagates in a finite medium, which has a boundary for its existence, it is called a guided wave, which again can be differentiated between Lamb waves and surface (Rayleigh and Love) waves in general. Thin plates, rods, tubes and multi-layered structures are considered to be waveguides. When ultrasonic waves travel in the waveguides at some angle and frequency, they are reflected back and forth inside the waveguides. This causes mode conversion, whereby the longitudinal and shear waves are reflected and transmitted at interfaces leading into both constructive and destructive interferences being superimposed together to form guided waves (Rose, 2014). For a particular angle and frequency chosen, the interference phenomena can be totally constructive, destructive, or intermediate in nature. There is certainly more than one constructive interference point for a set of incidence angles and frequencies for a guided wave problem. The constructive interference points can be plotted to produce wave velocity dispersion curves of frequencies versus phase velocities. Since phase velocity and incidence angle are represented by means of Snell's law, dispersion curves can be drawn for different phase velocities to frequencies.

Although bulk waves and guided waves are fundamentally different in either isotropic or anisotropic media, they are governed by the same set of partial differential wave equations. The main difference is that, for bulk waves, there are no boundary conditions that need to be satisfied by the proposed solution. The stress-free boundary condition in the guided wave analysis is difficult to solve analytically. In many cases, analytical solutions do not even exist and can only be solved numerically. Formulation of Lamb wave dispersion equations by solving characteristic wave equations are explained by many authors (Gopalakrishnan, 2011), (Giurgiutiu, 2014), (Nayfeh, 1995), (Raghavan, 2007) (Rose, 2014), (Rokhlin, Chimenti, & Nagy, 2011), (Ostochowicz, Kudela, Krawczuk, & Zak,

2012), and (Su & Ye, 2009). There are two basic types of Lamb wave modes called symmetric and antisymmetric modes. It can be proven that, at low frequencies, the symmetric Lamb waves approach the behaviour of the axial plate waves, whereas the antisymmetric Lamb waves approach the behaviour of the flexural plate waves. Lamb waves are dispersive waves and their speed depends on the product between frequency *(f)*, plate thickness (d) and isotropic/anisotropic properties. The wave-speed dispersion curves are obtained from the solution of the Rayleigh-Lamb equation (Equations 4.1 and 4.2). For a given frequency-thickness product, for each solution of the Rayleigh–Lamb equation, one can find a Lamb-wave speed and a corresponding Lamb-wave mode. Mode shapes and particle displacements of the fundamental symmetrical and anti-symmetrical modes are shown in Fig. 4.1 (a) and (b) where 'd' is the thickness of the plate and the arrows represent the direction of the particle vibration. These figures are obtained using COMSOL FEM simulation in 2D.

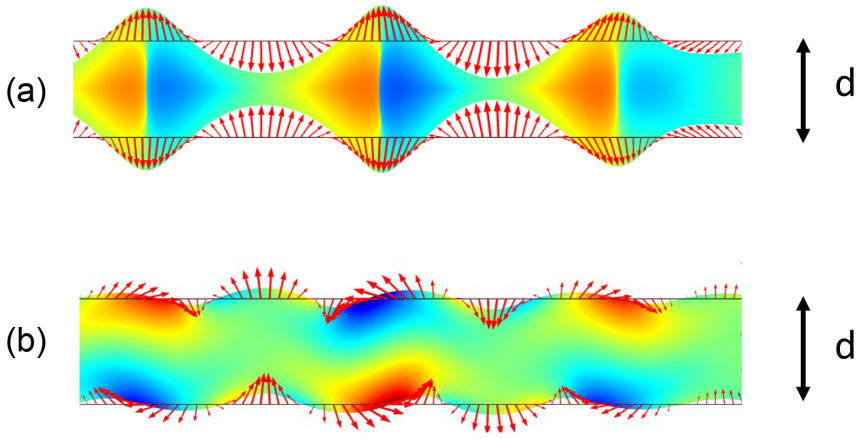

Figure 4.1 Mode shapes of fundamental: (a) Symmetrical; and (b) Anti-symmetrical modes

Characteristic Rayleigh-Lamb wave dispersion equation for the two modes are given in Equations 4.1 and 4.2. The detailed formulation of these equations can be referred to in (Rose, 2014).

$$\frac{\tan(qd)}{\tan(pd)} = -\frac{4pqk^2}{\left(q^2-k^2\right)^2} \quad \text{Symmetric modes} \qquad 4.1$$

$$\frac{\tan(qd)}{\tan(pd)} = -\frac{(q^2-k^2)^2}{4k^2pq} \quad \text{Antisymmetric modes} \qquad 4.2$$

where, $p^2 = \left(\frac{\omega}{C_L}\right)^2 - k^2$, $q^2 = \left(\frac{\omega}{C_T}\right)^2 - k^2$ and ω is circular frequency. Both p and q depend on the wave number k which is $\left(\frac{\omega}{c_p}\right)$ and c_p is the phase velocity of the Lamb wave mode. The terms C_L and C_T are longitudinal and transverse velocities of the medium. Lamb waves are dispersive waves with their speed depending on the product of fd between the frequency f and the plate half thickness d. The higher the fd product, the larger the number of Lamb-wave modes that simultaneously exist. Typical dispersion curves for a 3 mm aluminium plate are shown in Fig. 4.2 for phase velocities. For low values of the fd product, only the basic modes i.e., symmetric and antisymmetric Lamb wave modes exist.

As a result of Equation 2.9 from Chapter 2.1, the dispersion curves for the group velocities are obtained as shown in Fig. 4.3. Both the phase and group velocity dispersion curves are obtained using the CIVA- Guided Wave Testing Module (CIVA, 2015).

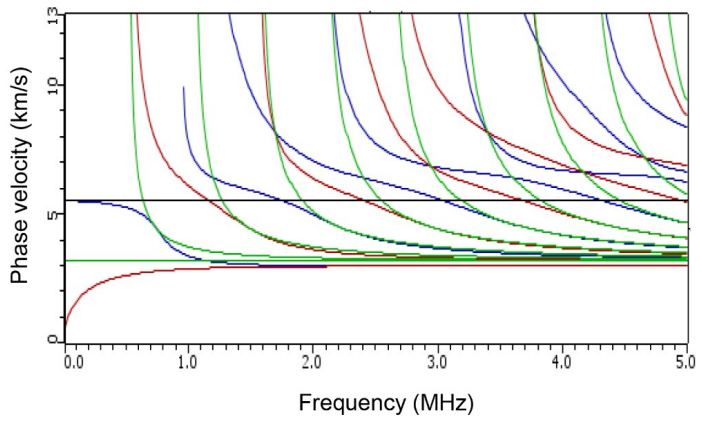

Figure 4.2 Phase velocity dispersion curve for aluminum plate of 3 mm thickness

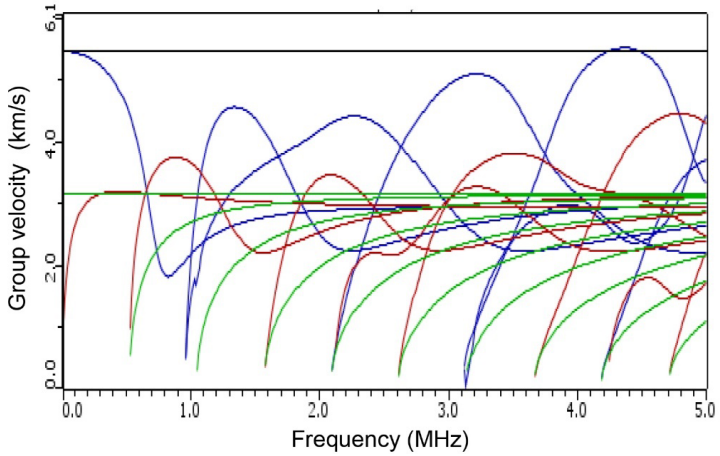

Figure 4.3 Group dispersion curve for aluminum plate of 3 mm thickness

4.2 Structural Health Monitoring Based on Guided Waves

Definition and importance of SHM can be referred to in the first chapter. In this section various concepts of SHM are explored. Basically, SHM can be classified as either an active or passive SHM system. When associated with NDT technologies to be integrated into the material or structure considered, passive techniques include techniques such as acoustic emission while the active techniques may include acousto-ultrasonics when considering acoustic principles. In SHM, the piezoelectric transducers can act both as transmitters (actuators) and receivers (sensors), which provide flexibility in terms of SHM. In active SHM as shown in Fig. 4.4 both actuators and sensors are used. Actuators send signals into the structure, which are then received by the sensors for evaluation, whereas in passive SHM (Fig. 4.5), only sensors are used. The signals generated as a result of activities such as impact or defect propagation are used as a source for generation of the signal. Damage localisation and damage characterisation are integrated components of the active SHM systems (Boller, Chang, & Fujino, 2009). The localised damages can be further evaluated by means of bulk acoustic waves for determination of accurate size of the flaws. The main advantage of SHM is automation of the inspection processes specifically in areas being badly accessible, which will reduce inspection cost without compromising safety and increase a structure's operational availability.

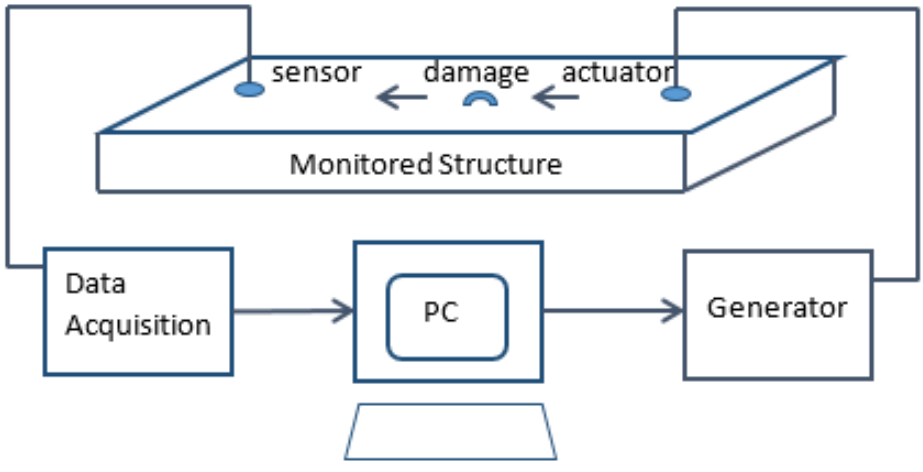

Figure 4.4 Elements in active SHM

Enhancement of the damage tolerance principle and hence lighter weight design through an opportunity of inspecting a structure's integrity on a virtually continuous basis and taking maximum advantage of a material's potential is the key aspect of SHM.

The most popular acoustic technique used in active SHM is guided wave testing with a specific focus on Lamb waves acting in structures of finite and constant dimensions.

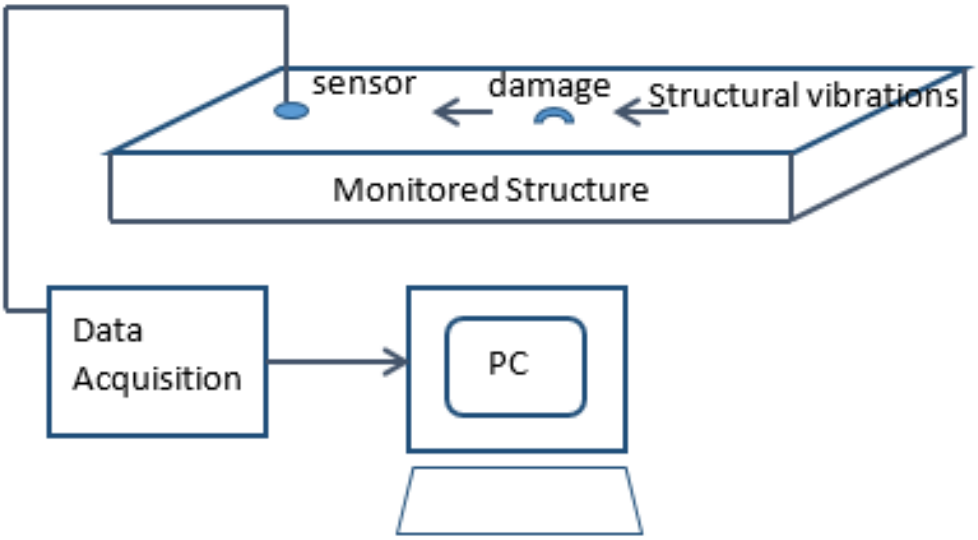

Figure 4.5 Elements in passive SHM

The advantages of guided waves are that they can effectively propagate long distances within the structures, provided the cross-section stays constant and acoustic impedance differences are high. With this they are suitable for localising damages within a large part of structures. Compared to conventional ultrasonic techniques monitoring on the basis of guided waves requires fewer sensors-actuators (transducers), which can be distributed on the surface for in situ damage monitoring. The principle involves small Piezo-electric Wafer Active Sensors (PWAS) (also considered as piezoelectric patches), which are embedded into and/or attached onto the structure acting as actuators for sending the guided wave signals and as sensors for receiving the guided waves respectively. The advantage of using several PWAS patches compared to traditional ultrasonic transducers is that they are light in weight, small in size and comparatively low in cost. The difference in principle of operations between PWAS patches and conventional ultrasonic transducers are explained in (Giurgiutiu, 2015). The important characteristics of Lamb waves in any medium is dispersion (i.e. phase and group velocities dependence on frequency of excitation) and as a result different mode of propagation exist for specific excitation frequencies, which complicates the process of interpreting the signals that come from the structure. The solution to the problem is to excite/generate single modes of guided waves rather than many.

PWAS are widely considered in SHM applications since they are comparatively inexpensive, non-obtrusive, non-intrusive, and minimally invasive devices (Nieuwenhuis, Neumann, Greve, & Oppenheim, 2005). These small devices can be easily attached onto the surface of structures for health monitoring purposes. These types of patches are available in a variety of shapes and sizes. PWAS patches work by the piezoelectric principle that couples the electrical and mechanical variables which is given by a constitutive equation of the form (Giurgiutiu, 2014)

$$S_{ij} = S^{E}_{ijkl}\sigma_{kl} + d_{kij}E_k + \delta_{ij}\alpha^{E}_{i}\theta \qquad 4.3$$

$$D_i = d_{ikl}\sigma_{kl} + \xi^{\sigma}_{ik}E_k + \tilde{D}_i\theta \qquad 4.4$$

where S^{E}_{ijkl} is the mechanical compliance tensor measured at zero electric field ($E = 0$), S_{ij} is the mechanical strain tensor, σ_{kl} is the mechanical stress tensor, and d_{kij} represents piezoelectric coupling effects. E_k is the electric field, D_i represents electrical displacement and ξ^{σ}_{ik} denotes dielectric permittivity at zero mechanical stress ($\sigma = 0$). θ is a temperature term and α_i is the coefficient of thermal expansion. $\tilde{D}_i$ represents the electric displacement temperature coefficient. δ_{ij} is the Kronecker delta (δ_{ij}=1 $i = j$; otherwise it is zero). Equations 4.3 and 4.4 are called the piezoelectric constitutive equations that are used to predict how much strain and electrical displacement will be created at given stress, electric field, and temperature. Equation 4.3 is the actuation equation, but Equation 4.4 can be more precisely represented in the following form to predict the electric field for a given applied stress:

$$E_i = g_{ikl}\sigma_{kl} + \beta^{\sigma}_{ik}D_k + \tilde{E}_i\theta \qquad 4.5$$

where E_i is the electric field and g_{ikl} is the piezoelectric voltage coefficient that denotes how much electric field is induced by the applied stress. The coefficient $\tilde{E}_i$ is the pyro electric voltage coefficient that represents how much electrical field is induced per unit temperature change and β^{σ}_{ik} represents the electric permittivity matrix. The Equation 4.5 is called the sensing effect equation. Piezoelectric materials can be used as sensors to measure deformations within the structure through their direct piezoelectric effect and as actuators to send acoustic waves into the structure through their converse piezoelectric effect. When the voltage is applied to this piezoelectric material attached onto the

structure's surface an in-plane motion is generated causing Lamb waves to propagate. Several different materials with piezoelectric properties are available. Although piezoelectric properties occur naturally in some crystalline materials (e.g. quartz crystals and Rochelle salt) the piezoelectric effect can be induced by electrical poling of certain polycrystalline materials such as piezoceramics. Lead Zirconate Titanate (PZT) and the polymer Polyvinylidene Fluoride (PVDF) are being widely used as piezoelectric materials for SHM applications. Table 4.1 shows different piezoelectric materials and their mechanical and electrical properties (Giurgiutiu, 2015). The application of PWAS in a guided wave based SHM is shown in Fig. 4.6, which shows two methods namely the pitch-catch and the pulse echo method. In the following Table 4.1, Young's modulus of PZT is similar to that of aluminium, whereas Young's modulus of PVDF is 1/12th of aluminium. Due to the lower stiffness, PVDF is much more suited to sensing applications. However, due to their higher piezoelectric coefficients PZT materials are much more suitable for actuation applications.

Property of transducer	units	PVDF	PZT
Density	Kg/m^3	1780	7500
Relative permittivity	$\frac{\varepsilon}{\varepsilon_0}$	12	1200
Piezoelectric voltage constant d_{31}	$10^{-12}\ \frac{C}{N}$	18-24	110
Voltage constant g_{31}	$10^{3}\ \frac{Vm}{N}$	216	10
Electromechanical constant k_{31}	$\%\ at\ 1\ kHz$	0.12	0.30
Young's modulus E_{11}	GPa	4-6	63
Acoustic impedance	$10^{6} Kg/m^2 s$	2.7	30

Table 4.1 Properties of piezoelectric materials

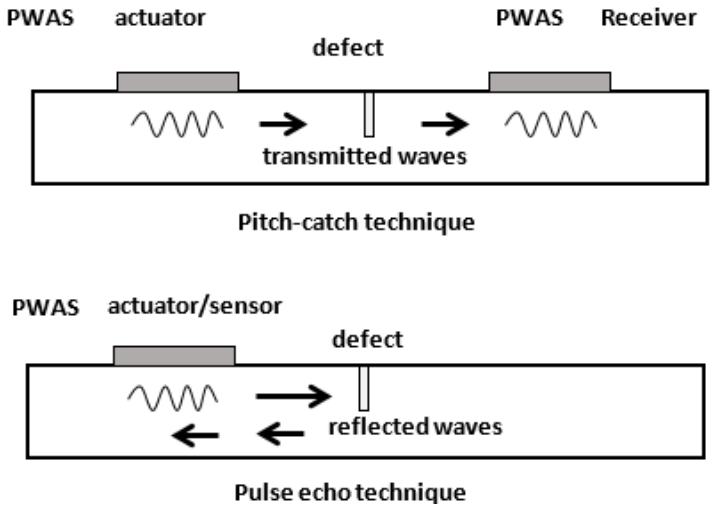

Figure 4.6 Pitch catch and pulse echo methods in acoustic based SHM

4.3 Guided Waves in the Context of Structural Numerical Simulation

To explore the complexities and application of GW in SHM, numerical simulation of GW has been performed on two types of test samples. The first one is a flat plate considered under fatigue loading with three holes where a crack is assumed to start from the holes. The test sample also named the 'generic plate' has been chosen to analyse guided wave phenomena under less complex conditions before switching to something being of a more complex and possibly also more application oriented shape. The second test sample is therefore a stiffened panel of a shape similar to what may be known from structures applied in aircraft or ships and has been called the 'stiffened panel'. Further details regarding the test samples is given below.

4.3.1 Generic Plate

This test sample consisting of a plate with three holes is shown in Fig. 4.7 and the respective material properties and dimensions are provided in Table 4.2.

Material	Properties	Dimensions	Crack geometry
Aluminium plate	Young's modulus-70 Gpa Density- 2700 kg/m^3 Poisson's ratio- 0.33	600 x 112 mm Thickness- 1mm Ø6mm-3 holes	Crack length- 25 mm Crack height- 1 mm

Table 4.2 Properties and dimensions of the generic plate

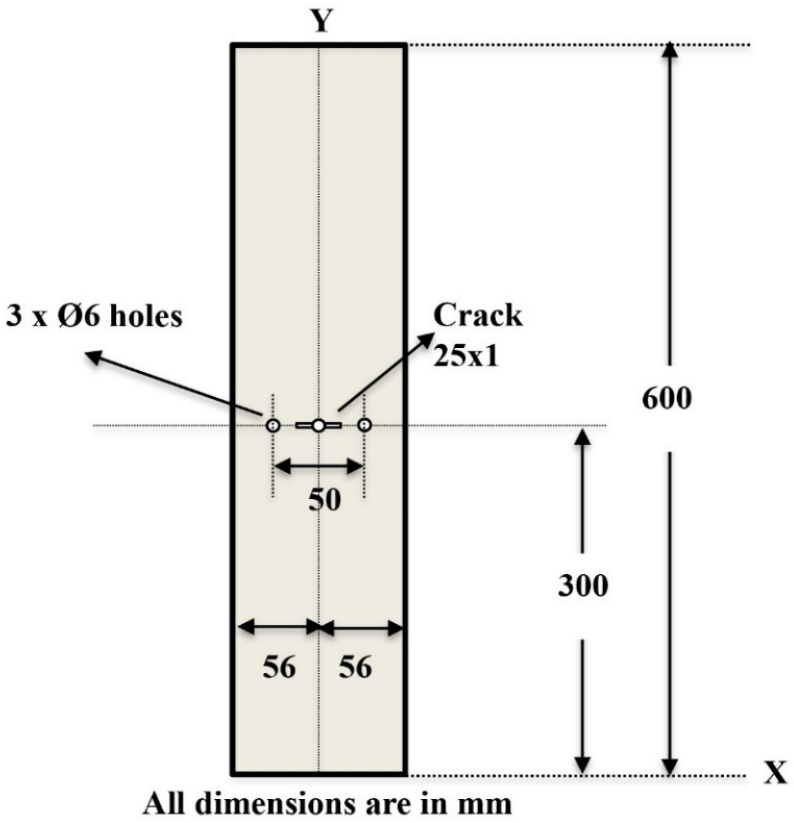

Figure 4.7 Generic plate for stress analysis and guided wave simulation

4.3.2 Stiffened Panel

This test sample is an aluminium plate with stringers riveted on it as shown in Fig. 4.8 and the material properties and dimensions are provided in Table 4.3.

Material	Properties	Dimensions	Crack geometry
Skin- Aluminium	Young's modulus-70 Gpa Density- 2700 kg/m^3 Poisson's ratio- 0.33	1300 x 1200 mm Thickness- 2 mm	Crack length- 51 mm Crack height- 1 mm
Stringer- Aluminium	Same as above	Ø 5mm- 51 holes for one stringer	

Table 4.3 Properties of the stiffened panel

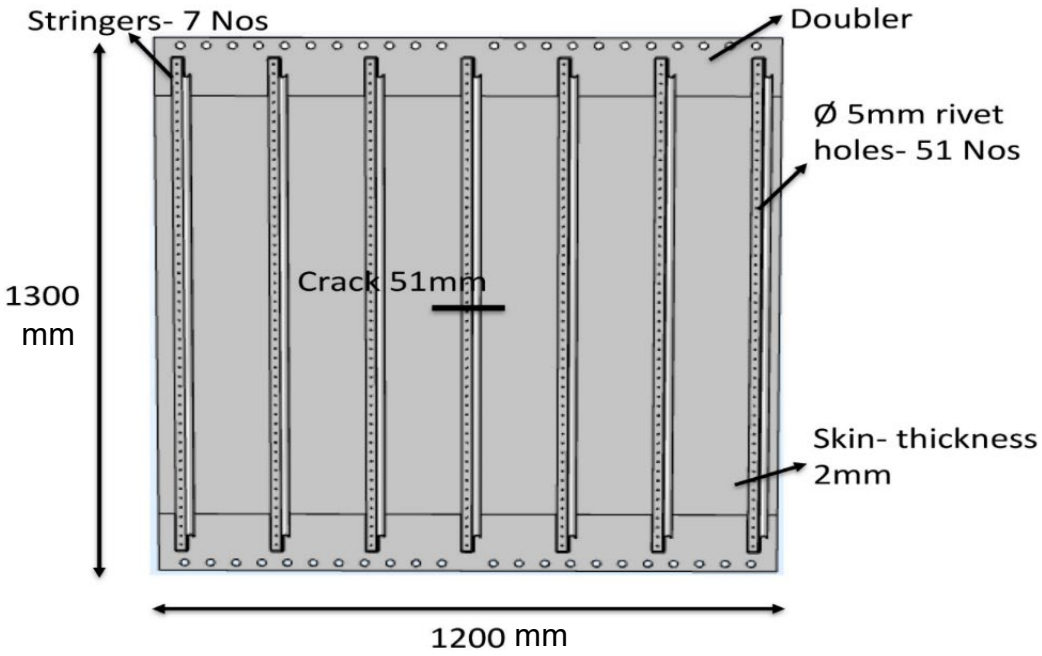

Figure 4.8 Stiffened panel for guided wave analysis

4.3.3 The Structural Simulation Process

Numerical simulation tools have been used for several decades in non-destructive testing and SHM. Significant progress in computational power and numerical algorithms in recent years has allowed the research community to simulate guided wave propagation more easily than before. There are numerous methods (Sridaran Venkat, Boller, Ravi, Mahapatra, & Steckel, 2015) listed for carrying out guided wave simulations. Apart from guided wave simulation, the role of FEM in stress/strain, fatigue and bulk wave ultrasonic simulations using CIVA form major elements in an acoustics based SHM. The sequence of application of these tools is shown in Fig. 4.9.

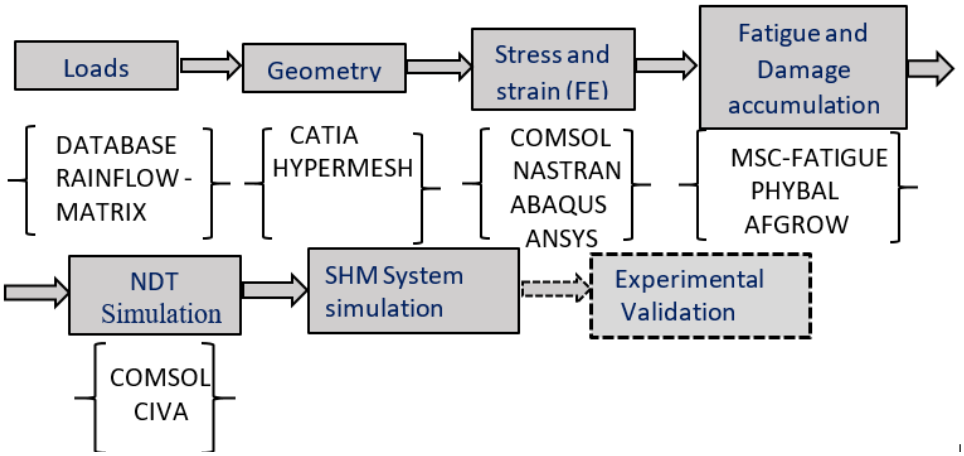

Figure 4.9 Sequence of simulation tools in SHM architecture

By means of computer aided designing tools (CAD), the digital model of a component considered has to be generated. Once the loads are known and applied on the component, the stress and strain distribution can be obtained through FEA (Finite Element Analysis) tools, where there are numerous FEA tools available on the market. The results from the FEA identify stress/strain concentrations where potential damage is due to arise. Until this point, the load is assumed to be static but when the structure is in operation, fatigue loads play an important role where the initiation and propagation of damage has to be determined through fatigue analysis and will aid in identifying the potential risk-zones for the damage initiation. MSC Fatigue and AFGROW software are examples that play a key role in this process. At this level, identifying the potential risk zone for a given structure and for a given loading condition is well established with the help of those CAD and FEA tools. Besides this, a link to NDT is established with the help of either FEM tools or EXTENDE's CIVA (CIVA, 2015). The main feature of this NDT simulation is to identify the transducer parameters to reliably detect the tolerable damages. It is mainly driven in terms of bulk wave ultrasonic NDT methods where the defect sensitivity highly depends on the parameters of the ultrasonic beam field. Typical application of this type of NDT simulation would aid designing an NDT and NDE procedure for the given flaw condition for a complex geometry.

Numerical simulation of guided waves using FEM-COMSOL tool offers many advantages. It helps one to understand and visualise the wave propagation and scattering process in an anisotropic material when the wave interacts with the damage. However, for the numerical solution to be accurate and to get the convergence, the mesh parameters especially for laminated composites need to be lower than the layer thickness which might increase the degrees of freedom in a FEM model and the computing power may not be enough to accomplish this task. Here, reduced geometry and homogenisation approaches need to be implemented without compromising the accuracy of the numerical solution. FEM is a time-consuming method as it solves for displacements at every time step, which may take a few hours to many days. There is therefore a need for efficient simulation tools for SHM guided wave simulations. Researchers used several hybrid methods to solve numerical problems in SHM. A well-known ultrasonic module in the NDE simulation tool CIVA 15 provided by EXTENDE uses an add-on hybrid function called ATHENA-2D, which combines semi-

analytically formulated ray tracing and FEM models for simulating the complex defects in ultrasonic NDE.

In another modelling study, (Srivatsava, 2010) used the global-local method to simulate the ultrasonic guided waves interaction with structural defects. In his approach, the Semi-Analytical Finite Element (SAFE) method was preferred in the global region when compared to a pure analytical solution. The advantage of the SAFE method is that it can handle complex geometries and multi-layered composites in an efficient manner. In Srivatsava's paper, the SAFE method is used in a global region and FEM analysis in the defect region for studying the defect interaction on an aluminium plate and aerospace composite joints and then validated his approach experimentally.

In more recent studies, (Gresil & Giurgiutiu, 2013) used a time-domain hybrid global-local concept for guided wave propagation using PWAS. In their paper, the time-domain analytical approach in the global region using an analytical software called Waveform Revealer (WFR) has been developed (Shen & Giurgiutiu, 2015) which allows the finite element mesh in the local region to describe the wave to defect interaction through modelling. The approach is quite like the one from (Srivatsava, 2010) described above. However, (Gresil & Giurgiutiu, 2013) used time domain signals in the global region using an analytical solution rather than a semi-analytical. The WFR software generates two time-domain signals S_o and A_o modes that go to the FEM module. This method is shown in Fig. 4.10. The output from the FEM module serves as an input for the WFR software again to generate the final waveform. The FEM in the local region is achieved by means of the ABAQUS - FEA software. Validation of this hybrid method with the experiment was carried out on Lamb wave interactions with notches and found a similarity between the experimental and the simulation results. This approach compared to previous methods has many advantages, however, the time-domain hybrid model has to be run every time for each test frequency. In addition to this, it requires interface matching or more appropriate boundary conditions between the analytical and the local FEM. The disadvantage of this method is that the analytical software (WFR) is not applicable to 2D or 3D problems, as well as for anisotropic structures.

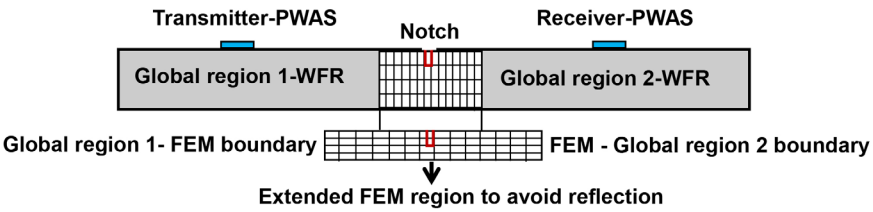

Figure 4.10 Global-local FEM approach using PWAS patches

(Shen, 2013), (Shen & Giurgiutiu, 2014) and (Shen & Giurgiutiu, 2015) have developed another hybrid method named Combined Analytical Finite Element Approach (CAFA) for PWAS based Lamb wave simulation. In their approach they computed Wave Damage Interaction Coefficients (WDIC) for coupling the analytical expression and the local FEM models. The purpose of WDIC is that it can for example describe the 3D interaction between the incident wave and the damage with scattering and mode conversion to be accounted for as well. One of the major features added to this approach is that the artificial non-reflecting boundary conditions to obtain WDIC and the entire analysis are carried out in 2D. The schematic representation of CAFA is shown in Fig. 4.11. Various hybrid numerical models used for simulating guided waves are shown in Fig. 4.12. Another interesting method for GW simulation is SFEM (Spectral FEM). The application of SFEM in SHM for various damage features has been studied by (Gopalakrishnan, 2011) and (Gopalakrishnan, Chakraborty, & Mahapatra Roy, 2008).

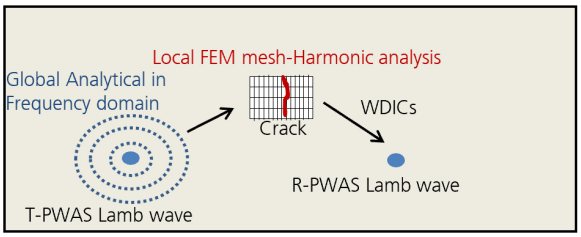

Figure 4.11 CAFA approach

In a recently completed activity (Balajee Ravi, et al., 2015), (Boller et al. 2016), (Balajee Ravi, Chakraborty, Mahapatra, Sridaran Venkat, & Boller, 2015), (Balajee et al. 2015) and (Balajee Ravi, et al., 2016) ray tracing has been combined with SFEM, which can become a potential numerical simulation tool for guided waves in composites. In the research programme, *Integration of Non-Destructive Evaluation based Ultrasonic Simulation* (INDEUS) the ray tracing-SFEM combination has been developed and validated with different other numerical simulation tools and by experiments.

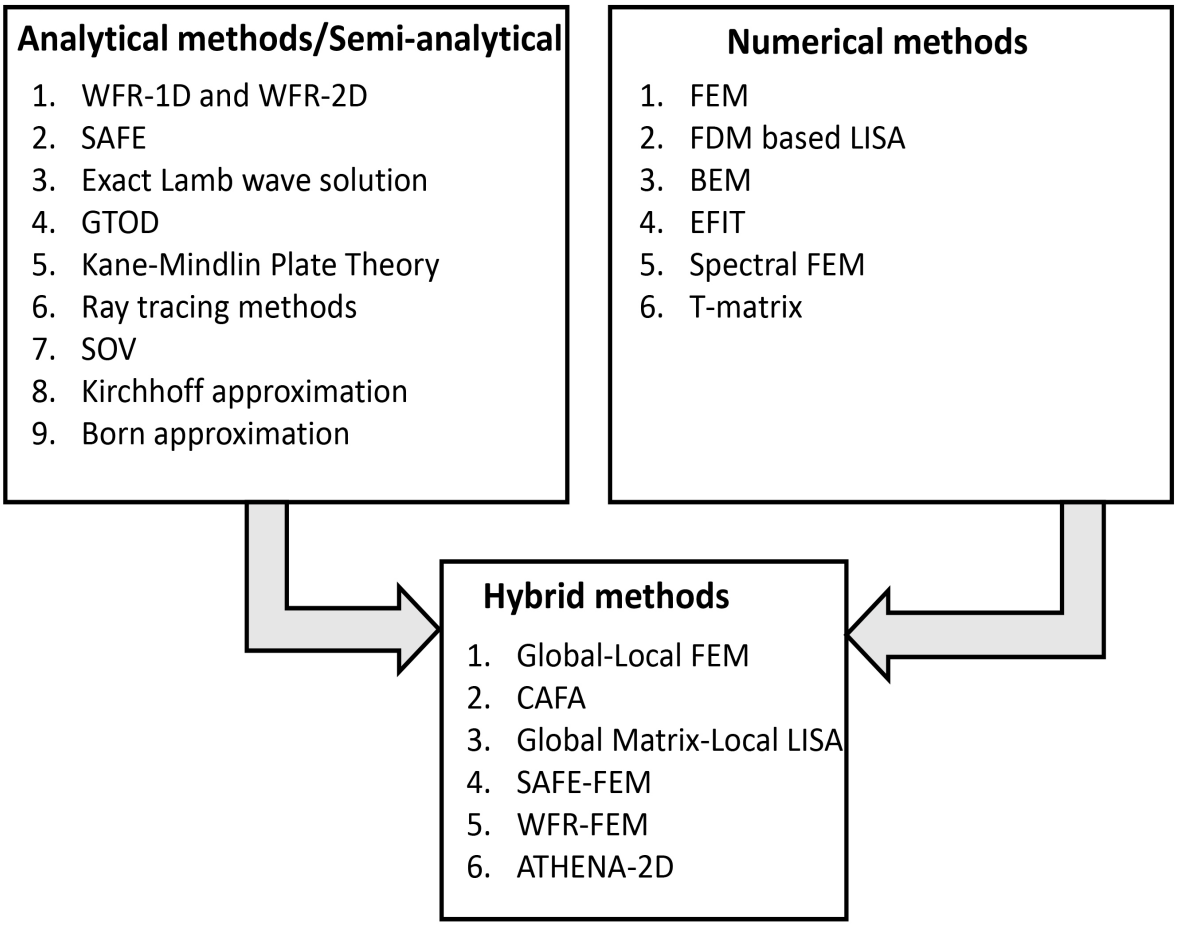

FEM- Finite Element Method
FDM- Finite Difference Method
EFIT- Elastic Finite Integration Technique
BEM- Boundary Element Method
GTOD- Geometrical Theory of Diffraction
CAFA- Combined Analytical Finite element Approach
SOV- Separation Of Variables
WFR- WaveForm Revealer
LISA- Local Interaction Simulation Approach
SAFE- Semi Analytical Finite Element

Figure 4.12 Various hybrid methods for ultrasonic NDE simulations

The numerical simulation interface allows one to input the transducer and flaw data for bulk wave analysis. The built-in ray tracing module performs guided wave simulation for SHM sensor configurations. Those models only perform a detailed analysis in the regions where damage is likely to occur while in the remaining areas of those structures simplified modeling through the application of ray tracing is performed.

4.3.4 Guided Wave Simulation Using FEM

Wave mechanics in any engineering structure is governed by partial differential equations and boundary conditions and the solution of the unknown variables is complicated if either the geometry or governing mechanism is too complex to obtain an analytical solution. In such cases FEM is used to obtain approximate solutions numerically. In FEM, the field is the domain of interest and most often represents the physical structure considered. The field variables are the dependent variables of interest governed by the differential equations. A schematic diagram of FEM is shown in Fig. 4.13.

Discretization of the whole domain into simpler sub-domains is one of the essential steps in FEM and it is defined as meshing. These sub-domains consist of simple shapes such as triangles, rectangles in 2D or tetragonal and bricks in 3D. This is shown in Fig. 4.14.

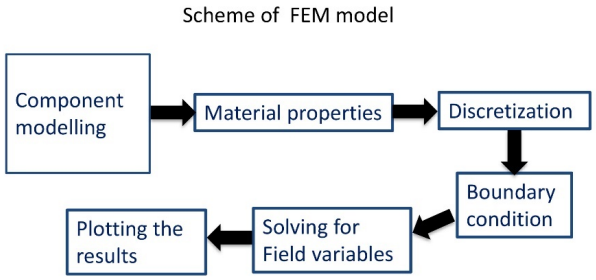

Figure 4.13 FEM process flow

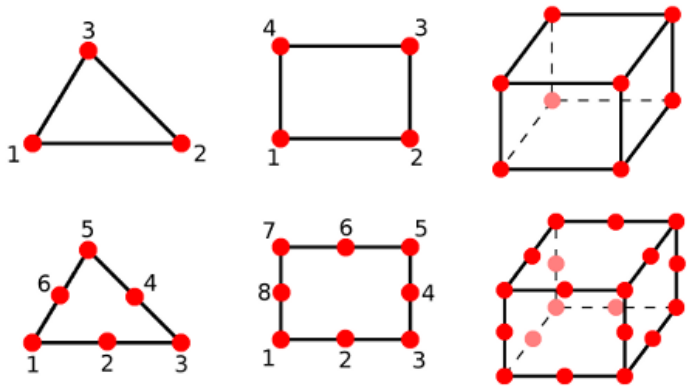

Figure 4.14 Triangular elements with 3 and 6 nodes, rectangular elements with 4 and 8 nodes and box element with 8 and 20 nodes (Sheehan, 2016)

It is assumed that an unknown displacement field on these shapes can be approximated using simple polynomial (quadratic) functions of a given order, the so-called shape functions. Each element has one or many nodes such that the shape function is assigned to

each node within an element. Constitutive equations can be derived from the theory of elasticity that shows the relationship between stresses, strains and displacements (Sheehan, 2016). In FEM, the algebraic equation on a single finite element for a dynamic stress analysis is written using Newton's second law as follows:

$$[M^E]\left\{\ddot{u}^E\right\} + [K^E]\{u^E\} + [C]\left\{\dot{u}^E\right\} = \{F^E\} \quad 4.6$$

where the parameters represent

K- Material stiffness

M- Mass matrix

C- Damping matrix

F- Applied force

u- Displacement

$\dot{u}$- Velocity vector

$\ddot{u}$- Acceleration vector

In order to obtain the solution for the unknowns (stresses), all the elemental equations are assembled in the following form:

$$[M]\left\{\ddot{u}\right\} + [K]\{u\} + [C]\{\dot{u}\} = \{F\} \quad 4.7$$

For a harmonic wave with a circular frequency of ω in an undamped material, Equation 4.7 can be simplified as:

$$([K] - \omega^2[M])\{u\} = \{F\} \quad 4.8$$

Matrix $[K] - \omega^2[M]$ is called the dynamic stiffness matrix. Based on Equation 4.8, the problem can be solved in the frequency domain instead of the time domain. To solve a dynamic problem in the time domain, numerical methods are needed. A direct integration method is the most popular numerical approach for calculating the time domain response. The numerical method is a finite difference method that obtains derivation of time from Taylor's polynomial. By means of a constitutive relationship, strains and stresses are obtained at all the elements. Material properties have been assigned to the geometric

model. Boundary conditions are necessary in order to solve the partial differential equation to get an optimal solution. Everywhere on the boundary either the displacements (Dirichlet boundary conditions) or forces (Neumann boundary condition) will be given. The structural mechanics module in COMSOL Multiphysics has various options for applying boundary conditions. The time dependant boundary load or electric potential is applied on the nodes to generate the initial displacement. The important parameters in the FEM model are element type, its size and the critical time step. Triangular mesh elements have been used since they are more sensitive towards defects like cracks and delaminations being typically considered (Su & Ye, 2009). The size of element is selected based on the criteria as given in Equation 4.9.

$$\Delta x_{max} = \frac{\lambda_L}{R} \tag{4.9}$$

where λ_L is the wavelength of the longitudinal ultrasonic wave and R is the ratio of the wavelength to Δx_{max}. The value of $R \geq 8$ is recommended in (Ghose & Balasubramaniam, 2011). The requirement for the critical time step $\Delta t_{critical}$ is as given in Equation 4.10.

$$\Delta t_{critical} = \frac{\Delta x_{max}}{C_L} \tag{4.10}$$

In the modelling of wave propagation, a small deformation of elements is assumed with the critical time step being the time required for the wave to pass through the smallest element in the model. The condition in the above equation is called the CFL (Courant Friedrich Lewy) criterion (Zepeda Nunez, 2017), where C_L is the longitudinal ultrasonic wave in the material to be analysed. COMSOL Multiphysics chooses the optimised solver and its settings are based on the chosen space dimension, physics and study type.

For the generation of guided waves using structural mechanics a direct mumps solver is used. Normally, COMSOL uses two fundamental classes of algorithms that are used to solve Equation 4.8: the direct and the iterative methods. The direct solvers used by COMSOL are the mumps, pardiso, and spooles solvers (COMSOL-Multiphysics, 2016). All these solvers are based on the Lower-Upper (LU) decomposition or factorization. Once the solutions from the solver are obtained the results can be plotted in displacement fields (u, v, w) as a function of time. It can also be represented as in 1D as time versus displacement fields. Fig. 4.15 shows the 2D displacement field (y-component) for symmetrical wave

propagation obtained by the structural mechanics module in COMSOL. In the modelling performed in this thesis, Δx_{max} of 1.2 mm and 2.5 mm have been used in the structure domain and Δx_{max} of 0.2 mm has been used for the piezoelectric domain (Table 4.4). The time step of 0.1µs satisfies the CFL criteria. When solving a system of linear equations of a simulation, COMSOL will automatically detect the best solver without user interaction.

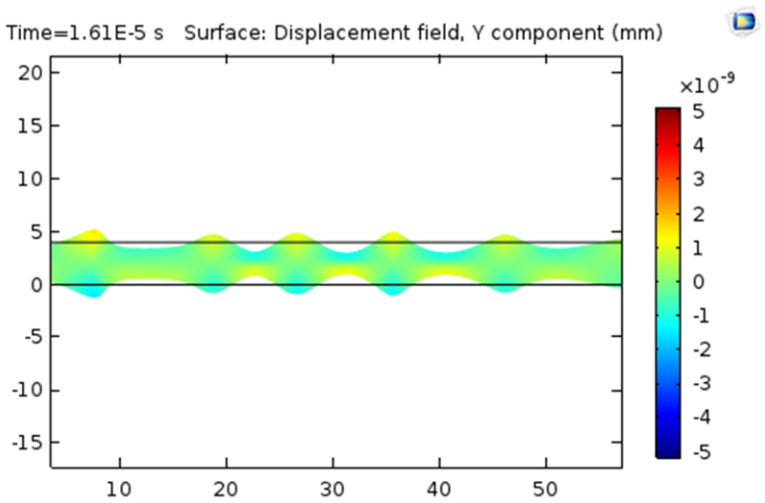

Figure 4.15 Displacement field in 2D for a plate geometry using COMSOL Multiphysics

Material	Mesh parameters	Time step	Maximum duration
Generic specimen	Δx max= 1.2 mm	0.1 µs	90 µs
Stiffened plate	Δx max= 2.5 mm	0.1 µs	170 µs
Actuators and sensors	Δx max= 0.2 mm		

Table 4.4 FEM parameters for guided wave simulation

In the context of this thesis 3D FEM models have been developed by means of COMSOL-Multiphysics that couple piezoelectric devices and the structural mechanics modules. The material behaviour due to an applied force has been studied within the structural mechanics module and the piezoelectric effect has been studied within the electrostatics

domain. This is shown in Fig. 4.16 where the piezoelectric material is being applied as a common interface between the two-coupling physical materials. A 2D-FEM model was studied by (Nieuwenhuis, Neumann, Greve, & Oppenheim, 2005) for the generation and detection of guided waves using PZT wafer transducers. The governing equations for the piezoelectric effect, i.e. the generated electric field for the applied stress, electrical displacement and converse piezoelectric effect in terms of the total strain generated for the given electric field, the resulting stress σ can be referred to from Equations 4.3 to 4.5.

Guided wave simulation can be performed without the multi-physics option by considering only the structural mechanics module and then plain strain condition. In this case the respective transducer geometry is given a time dependent boundary load. The application of such a model can be referred to in the literature (Ghose & Balasubramaniam, 2011). The advantage of the multi-physics model is that it allows guided wave propagation to be simulated when actual piezoelectric properties of the actuator and sensor are considered which has greater influence on the sensitivity towards the damage.

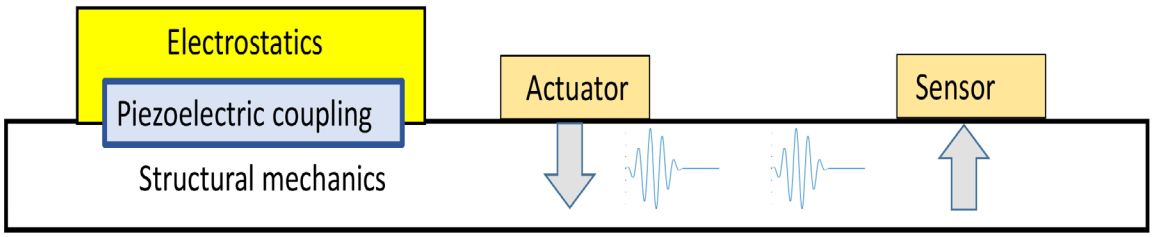

Figure 4.16 Guided wave multi-physics model in COMSOL

4.3.5 Input Signal or Excitation Signal

Since guided waves are dispersive waves, a tone burst excitation has been chosen in order to excite coherent single-frequency waves and to minimise the dispersion. However, the raw tone burst excitation has side frequencies or side lobes associated with the sharp transition at the start and the end of the signal. A Hanning window function of the form (Equation 4.11) is therefore applied to smoothen the raw tone burst excitation to apparently reduce the side lobes (Giurgiutiu, 2014). The windowed signal and frequency spectrum of the smoothed tone burst signal is shown in Fig. 4.17, which hardly shows any side lobes.

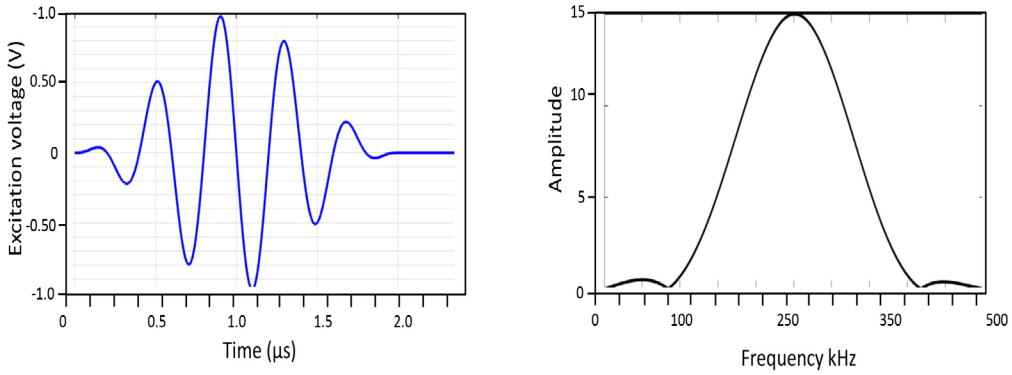

Figure 4.17 Hanning window tone burst excitation

$$V(t) = \frac{1}{2}\left[1 - \cos\left(\frac{\omega_0\, t}{N_c}\right)\right] \sin(\omega_0\, t), t \in \left[0, \frac{N_c}{f}\right] \qquad 4.11$$

where,

$V(t)$ – Excitation voltage

ω_0- Angular frequency

N_C- Number of cycles.

4.3.6 Boundary Conditions

Linear elastic material is selected from the structural mechanics domain and charge conservation, electric potential and ground are selected from the electrostatics domain. All the sides of the specimen are set as free boundary conditions. Peak to peak voltage of 20V of the excitation function of the form of Equation 4.11 is applied on the actuator geometry and all the piezoelectric materials are grounded. Low reflecting boundary conditions have been selected in order to avoid reflections from the boundaries.

4.4 Numerical Simulation Results

4.4.1 Selection of Actuators and Sensors

In order to record the received electrical voltage on the sensors for all the time steps, COMSOL software has built-in boundary probe models. A boundary probe has been selected from COMSOL for all the sensors. The selection of piezoelectric material for the actuator and sensor has a large influence on the guided wave results. Table 4.5 shows the properties and dimensions of the piezoelectric materials.

Type	Dimension	Properties
PZT-5A	Ø5 mm and 0.48 mm thick	d_{33}= 350 x 10^{-2} m/V g_{33}= 16.6 x10^{-3} Vm/N k_{33}=0.53 k_{31}=0.40 ρ=7.7 g/m^3

Table 4.5 Piezoelectric properties for simulation

d_{33}- Extensional strain constant

g_{33}- Extensional voltage constant

k_{33}- Extensional coupling coefficient

k_{31}- Transverse coupling coefficient

ρ- Density of the material.

Properties*- other mechanical, physical properties are available in the COMSOL material library.

4.4.2 Stress and Fatigue Analysis

Stress and displacement analysis of the generic plate (Fig. 4.7 and Table 4.2) are shown in Fig.s 4.18 (a & b) and 4.19 (a & b) using ANSYS and COMSOL Multiphysics. The stiffened panel (Fig. 4.8 and Table 4.3) has seven 'L' shaped stiffeners. The stiffeners are provided to support the skin and to prevent the skin from bending and specifically buckling in the z direction. A 21 kN in-plane pressure has been applied on this stiffened panel. Stress analysis was carried out for an undamaged stiffened panel as well as for plates with various crack lengths. The cracks were introduced at a rivet hole location in the centre of the panel including the associated stiffener. The stress contour is shown in Fig. 4.20 (a) for various crack lengths. It can be observed from the contours that for the undamaged panel the maximum stress arises around the rivet holes and these are the areas prone to crack initiation. As crack length increases, the stress intensity at the crack tip increases too. Generally, the stress or strain response of a structure or a component to loads applied is the indication for any type of fatigue to initiate. A probability of damage can be determined by performing fatigue analysis numerically even for a cracked structure as seen in Fig. 4.20(b).

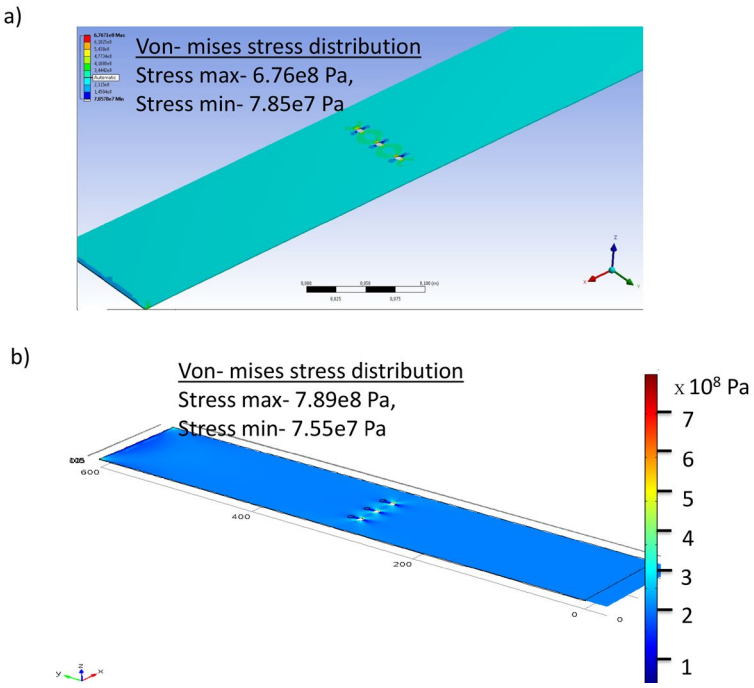

Figure 4.18 Stress simulations using: a) ANSYS FEM; and b) COMSOL Multiphyscis tools

The initial crack length was set here to 50 mm and stress and fatigue analyses were carried out for different crack lengths up to 340 mm.

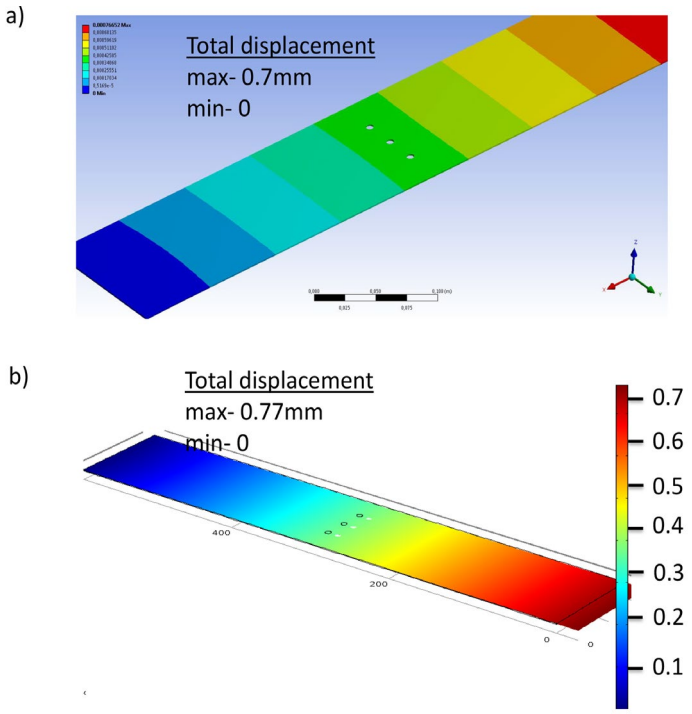

Figure 4.19 Strain simulation using FEM: a) ANSYS; and b) COMSOL Multiphysics

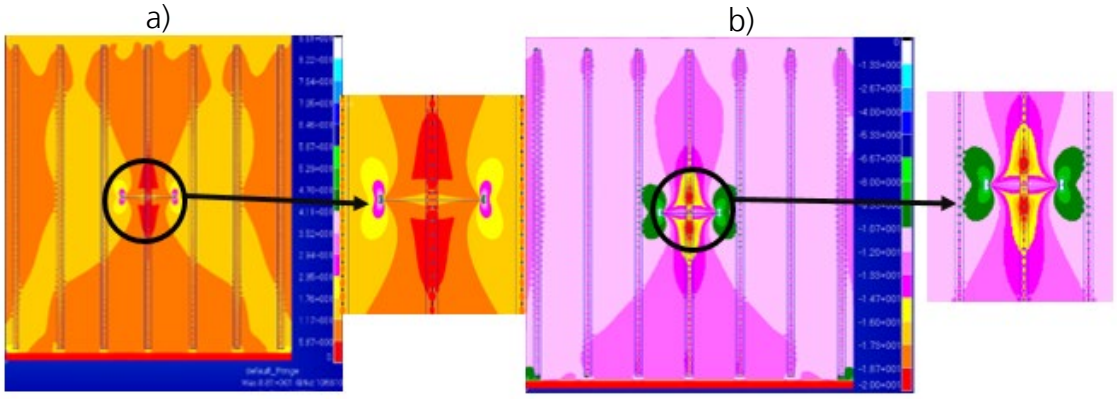

Figure 4.20 Stiffened panel with crack and their corresponding: a) Stress concentration zones; and b) Probability of damage accumulation (Balajee Ravi, et al., 2016)

4.4.3 Guided Wave Propagation

Results of the guided wave propagation for the pitch-catch method using COMSOL Multiphysics are shown in Fig.s 4.21 and 4.22 for the generic plate and Fig. 4.23 for the stiffened panel. The top view of the simulation results is shown for both the undamaged and damaged conditions for various time steps. The length of the crack is 25 mm for the generic plate and 51 mm for the stiffened panel respectively. There are two modes S_0 and A_0 that exist in the plates as has been seen in the beginning of the chapter for the given excitation frequency of 200 kHz. The actuators and sensors are marked as circles in these figures. The crack is placed on the middle of the plate based on the assumption that the crack would originate around the rivet holes and the load being symmetrical across the plate. As the wave encounters the crack region, it undergoes reflection and transmission. The intensity of the reflection and transmission depends on the length of the crack.

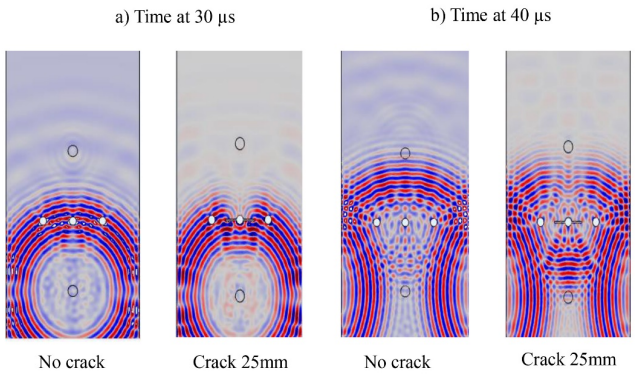

Figure 4.21 Guided wave propagation in the generic plate at various time intervals for the geometry having no crack and crack after: a) 30 μs; and b) 40 μs

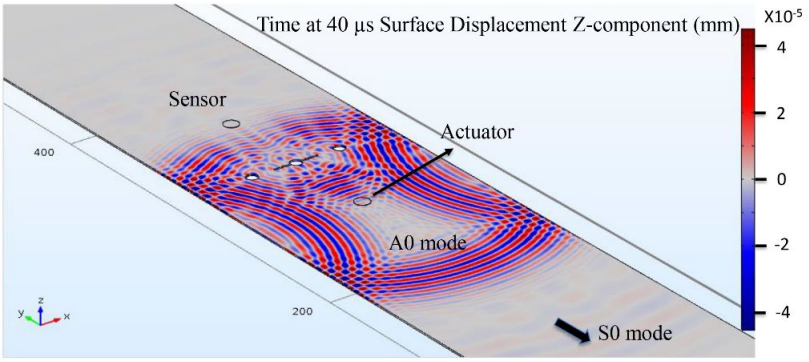

Figure 4.22 Guided wave propagation in generic plate in three dimension

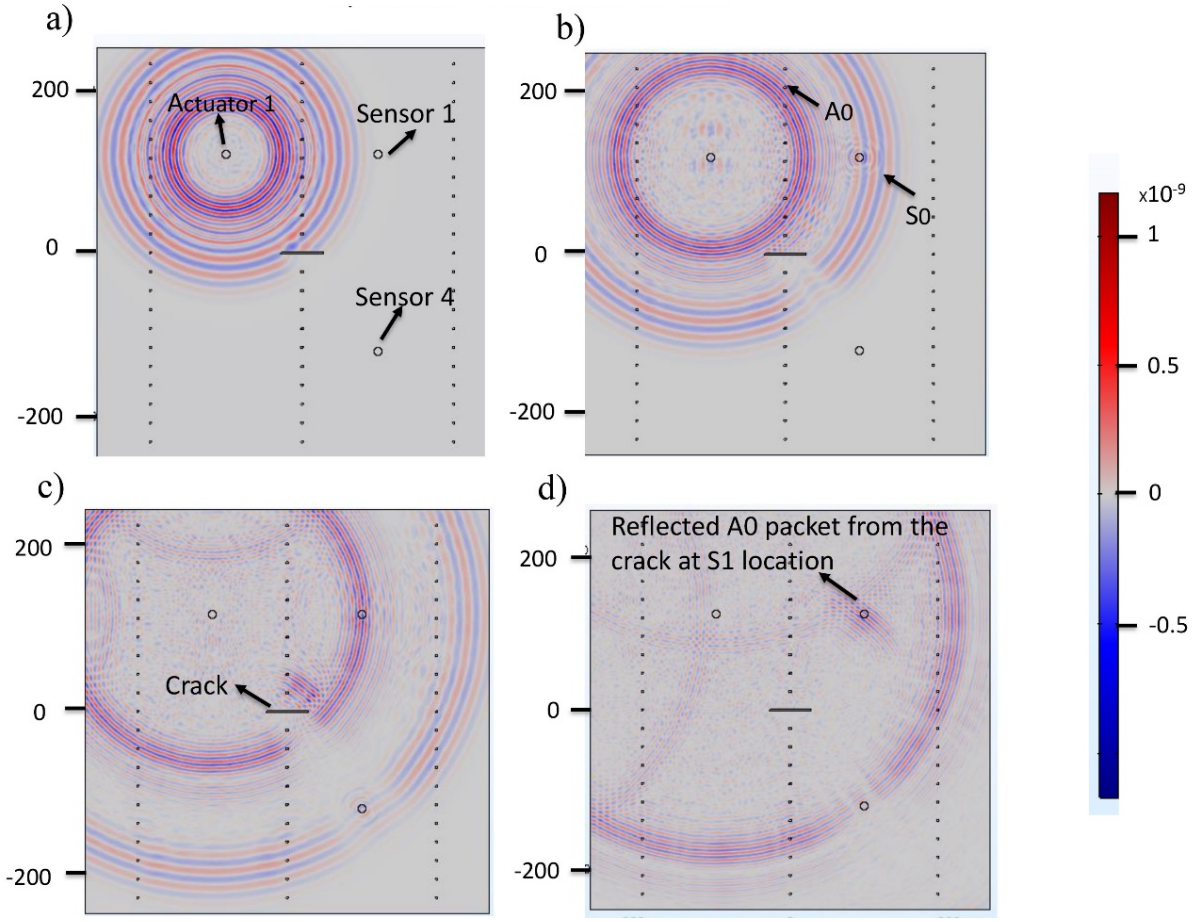

Figure 4.23 Guided wave propagation in stiffened panel having no stringers in the geometry after various time intervals from signal initiation: a) 30 µs, b) 45 µs, c) 65 µs; and d)105 µs

4.5 Differential Imaging as Means for Damage Information Monitoring

The damage tolerant design principle enhances a structure to be designed lightweight. The key factor for an optimised monitoring is to find the key locations where a damage information can be extracted. Various studies have been undertaken by different institutions (Malinowski, Wandowski, & Ostachowicz, 2012), (Wandowski, Malinowski, & Ostachowicz, 2016), (Sharif Khodaei, 2016), (Fendzi, et al., 2014), (Mallardo, Aliabadi, & Sharif Khodaei, 2012), (Lee & Staszweski, 2007) and (Shi, Law, & Zhang, 2000) in the context of sensor optimisation for guided wave based monitoring.

Most of the work has been focussed on random sensor placement. However, (Malinowski, Wandowski, & Ostachowicz, 2012) used scanning LDV measurements on the test component to find the optimum sensor layout for an artificial damage. They used both concentrated sensors and distributed sensor arrays for the investigation. LDV, by its advantage of non-contact measurement, could record the out-of-plane and in-plane displacements for a given set of scanning points defined by the user which could otherwise have been achieved by the PZT mounted on the surface of the specimen. The authors (Malinowski, Wandowski, & Ostachowicz, 2012) introduced a damage index for a received signal along with signal processing as shown below by Equation 4.12.

$$DI(P) = \sum_{k=0}^{n} \hat{S}(t_k) \qquad 4.12$$

where, $DI(P)$ is the damage index calculated at an arbitrary point P and $\hat{S}(t)$ is the squared time-windowed signal $\hat{S}(t_k) = S^2{}_W(t)$ and $S_W(t) = S(t) \times W(t)$. Here $S(t)$ is the time domain signal and $W(t)$ is the windowed part of time-domain signal as shown in Fig. 4.24. t_{AP} and t_{PS} in this figure are corresponding to the travel times of the wave from observation point P to the actuator (A) and to the sensor (S). The procedure is repeated for all the points from the mesh created during the LDV measurement. The time window is defined for all the signals and if it registers any damage reflections, the value of $DI(P)$ would be higher and vice versa for undamaged conditions.

Three types of sensor network were taken for the analysis; 1. Concentrated sensor array of 3x3, 2. Concentrated sensor array of 5x5 and 3. Distributed sensor array of 5x5.

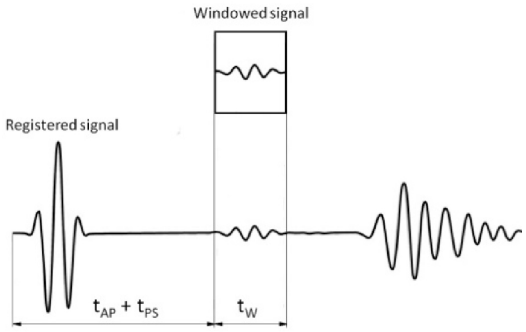

Figure 4.24 Windowing in damage detection algorithm (Malinowski, Wandowski, & Ostachowicz, 2012)

For all these cases, the actuator was placed on the centre of the test object, which was an aluminium plate of 1000 x 1000 x 1 mm in size. The damage index $DI(P)$ evaluated from the equation for all the scanning points are mapped into the component coordinates using different colour values. The high $DI(P)$ values lead to the formation of ellipses while mapping all the scanning points. The results of the distributed sensor network show more promising results than the concentrated array network. This is because of the concentrated arrays, where the foci of the ellipses are close to each other. In a similar approach, (Wandowski, Malinowski, & Ostachowicz, 2016) used the LDV for registering the elastic wave field to study the various mode conversions for different defect configurations. (Sharif Khodaei, 2016) used an optimisation sensor strategy based on the maximum coverage area (MCA) within a sensor network for a complex composite structure. A fitness function (Equation 4.13) was introduced in this paper (Sharif Khodaei, 2016) that considered physical and geometrical constraints of the structures in addition to the wave propagation characteristics of the composite structures. Within the sensor network, the optimisation process driven by genetic algorithms ensures the maximum coverage area for the sensors. This will in turn reduce the number of sensors required to detect the damage. When the sensors are close to the boundaries, the damage index reduces for that sensor since the reflected waves from the damage and the reflected waves from the boundaries do coincide. The fitness function of the first part is formulated by means of dividing the structure into pixels and constructing ellipses for all the sensor pairs. This results in identifying the intensity of the coverage. The ellipses are not included in the

fitness function if the length of the ellipse falls outside the boundaries. The highlight of the proposed method is that it considers the directional velocities of the composite structures, while constructing the ellipses. Another physical parameter related to wave attenuation is considered from the experiment and an attenuation profile is drawn such that the coverage index is weighed. The overall or global fitness function is defined as follows:

$$F = \frac{1}{C \cdot A_{network}} \tag{4.13}$$

$$C = \sum_{pixel=1}^{N\ pixels} cov(pixel) \cdot attenuation\ factor \tag{4.14}$$

$$cov(pixel) = \sum_{path=1}^{N(N-1)} CI(pixel, path) \tag{4.15}$$

The value of CI is '0' for the ellipses falling outside the boundaries and '1' when it falls within the boundaries. $A_{network}$ is the area included within the sensor network. Once the minimum number of sensors N is chosen, then the optimisation algorithm searches for the optimum position P. The total number of possible networks made of N transducers with P being the number of possible positions is evaluated using genetic algorithms. The applicability of this algorithm has been demonstrated for a full composite wing, which has stiffeners, frames and varying thicknesses. In a similar way, (Fendzi, et al., 2014) formulated the optimisation problem where the objective function to be maximised is evaluated by means of a ray tracing approach and solved using genetic algorithms. (Sharif Khodaei, 2016) and (Fendzi, et al., 2014) considered the group velocity and spatial attenuation for extracting the damage features from the composite structures.

The probability of detection (POD) function depends on scattering of the wave by the damage. According to (Fendzi, et al., 2014) , it can be mathematically represented as:

$$E^{scatter} = \sum_{i=1}^{N} \int_{ti}^{tf} \left| \left(X^i sl(t) - X^i so(t) \right) \right|^2 dt \tag{4.16}$$

In Equation 4.16, $X^i sl(t)$ represents the measured time response of sensor i with damage and $X^i so(t)$ represents the measured time response of sensor i without damage respectively while ti and tf are the starting and ending time point of the integration. One

can get this scattering function through the finite element simulation. Instead of solving the transient FEM, which is computationally expensive, (Fendzi, et al., 2014) modelled the wavefronts of guided waves in the composites using a 2D-ray tracing method. In that case guided waves are discretized as rays, the group velocity determines how fast the rays travel with regard to time and the attenuation function determines how the amplitude varies during the propagation. The angular dependent velocities and the attenuation were measured through experiments. Here the optimal sensor position means the number of rays reflected from the damage and then going through the sensors to be maximum. Thus, the objective function can be defined as the number of these reflections and solves for the global maximum through the genetic algorithms.

(Mallardo, Aliabadi, & Sharif Khodaei, 2012) used Artificial Neural Networks (ANN) algorithms in combination with genetic algorithms to find the optimal sensor locations for detecting impact damages in a composite structure. ANN require data from sensors to train the network and it is difficult to produce the impact damage experimentally on various locations, so numerical simulation using FEM was adopted in this paper. An interesting contribution in the optimal sensor position studies comes from (Lee & Staszweski, 2007) where they used numerical simulations of 2D wave propagation of various defect configurations in an aluminium plate and they call the wave propagation method as Local Interaction Simulation Approach (LISA). From the simulation, the peak-to-peak amplitudes of different wave modes were calculated and represented as contour plots for all the coordinates (x, y) of the specimen under investigation. This process is repeated for the damaged and the undamaged conditions such that the largest difference in amplitudes in the contour plot shows the favourable position for placing the sensors.

When the excitation voltage is applied on the piezoelectric material, the strain obtained in a structure such as an aluminium plate is used for simulating the wave propagation problem in COMSOL Multiphysics. The relationship between the stress ($\sigma_{ij,j}$) and the displacement by ($\ddot{u}_i$) is obtained through the equation of motion (Equation 4.17):

$$\sigma_{ij,j} + \rho f_i = \rho \ddot{u}_i \qquad 4.17$$

where, ρ and f_i are the density of the medium and the applied force respectively. For the known elastic constants and by means of Hooke's law $\sigma_{ij} = C_{ijkl}\varepsilon_{kl}$, the following

constitutive relation is established between stress, strain and the displacements, which is implemented in the COMSOL structural mechanics module. Strains are defined from the deformations by:

$$\varepsilon_{ij} = \frac{1}{2}(u_{ij} + u_{ji}) \tag{4.18}$$

With respect to displacement in z-direction, the strain can be written as $\varepsilon_{ZZ} = \frac{\partial u_Z}{\partial Z}$ and one can write the differential displacements in the form of Equation 4.19:

$$\frac{\partial z\, \Delta u}{\partial z\, \partial t} = \left[\frac{\partial z\, u_{\,damaged}}{\partial z\, \partial t} - \frac{\partial z\, u_{\,undamaged}}{\partial z\, \partial t}\right] \tag{4.19}$$

where σ and ε are the Cauchy stress and strain tensors and u is the displacement. The results of the FEM simulation are wave propagation at all the time steps and the recorded voltage signals at the sensor locations. The wave propagation at various time intervals for undamaged and damaged cases is shown in Fig.s 4.21 to 4.23 for the generic plate and for the stiffened panel respectively. In guided wave analysis, the signals at the present state of the structure are often compared with the signals that were stored during the pristine condition. This process is often done only after placing the sensors for monitoring, which are supposed to be at an optimum location for measuring the damage. However, in order to find the optimum position of the sensors, differential imaging is an interesting option to be applied, which is very similar to differential signals (Giurgiutiu , 2014). In this method, the wave propagation at particular time intervals for the given damage is subtracted from the wave propagation of the pristine condition using Equation 4.19. The resultant wave propagation shown in Fig.s 4.25 to 4.27 shows the points of maximum and minimum residual displacements for the generic plate for various crack sizes as the wave propagates over time.

Fig. 4.28 shows the differential image results for the stiffened panel. The differential FEM model is built by implementing a parametric sweep for an undamaged and a damaged condition using COMSOL Multiphysics. Based on the results of differential imaging, the maximum residual displacement points have been selected as shown in the differential images.

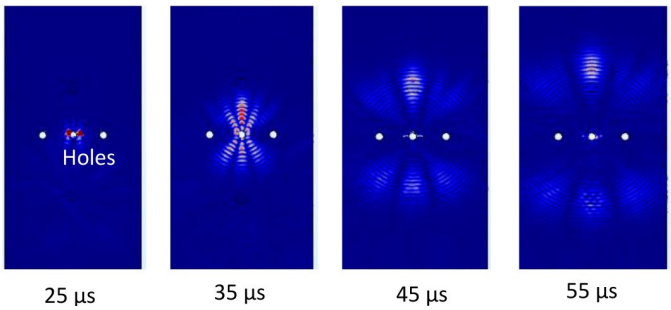

Figure 4.25 Differential images for the generic plate with a crack length of 15 mm at the central hole

These points are termed as hot spots where the sensors should be placed on these paths (the direction and magnitude of the highest differential displacements in the images) to have a maximum detectability of the damages. Also for any complicated geometries, the influence of boundary reflections affect the detectability because it is more difficult to separate the reflections from the boundary and the reflections due to the damage. However, in differential imaging, the reflections due to boundaries are subtracted such that they have zero influence on the detectability.

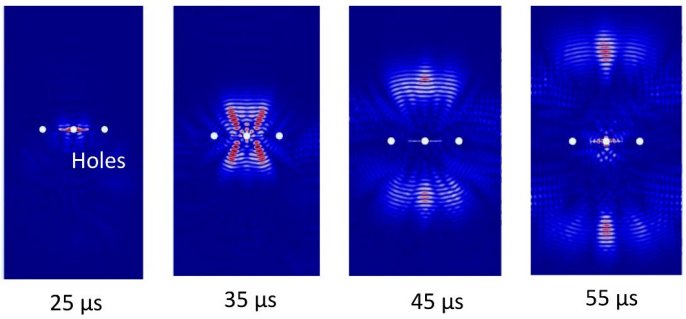

Figure 4.26 Differential images for the generic plate of crack length 25 mm at the centre hole

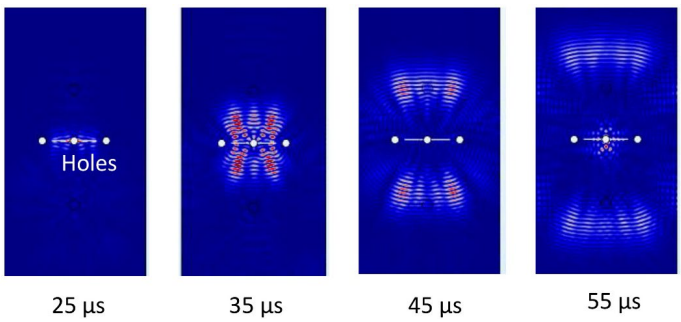

Figure 4.27 Differential images for the generic plate of crack length 35 mm at the centre hole

Fig.s 4.29 and 4.30 show the sensor positions on the generic plate and the stiffened panel for a given actuator position for further analysis respectively. Fig.s 4.31 and 4.32 show the received signals for corresponding sensor positions for both the test samples.

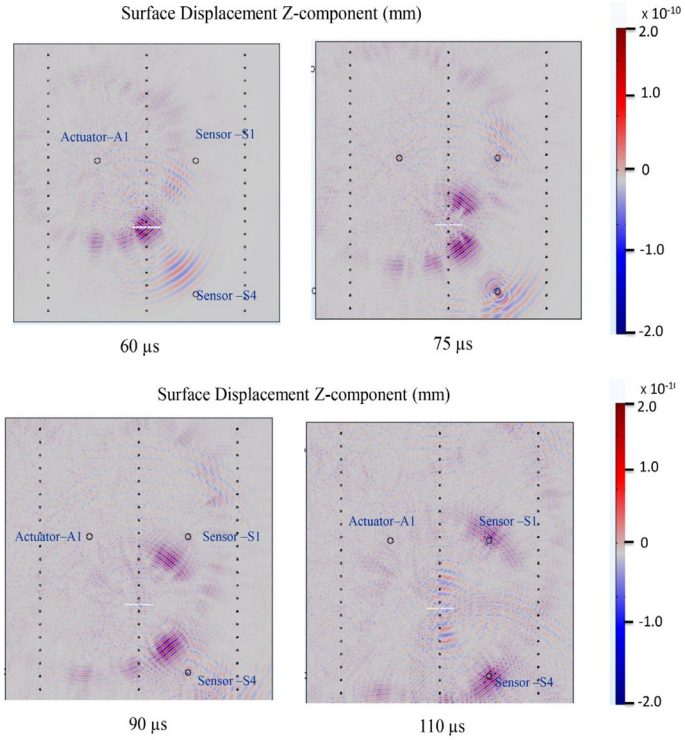

Figure 4.28 Differential images for stiffened panel for a crack length of 51 mm starting at the middle rivet line at various times

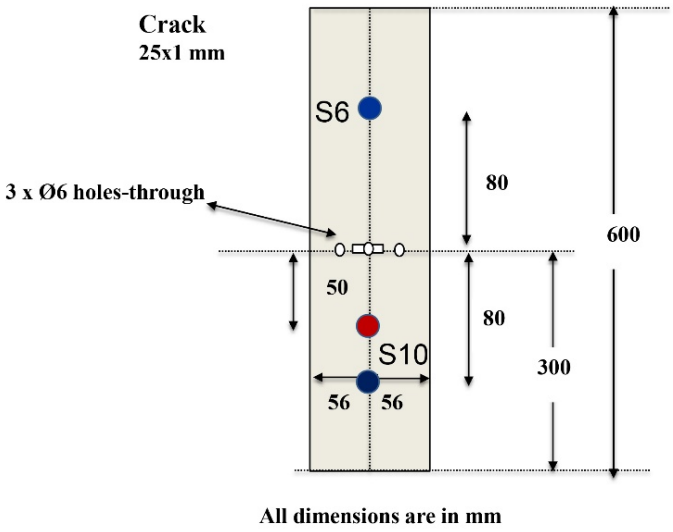

Figure 4.29 Actuator and sensor positions on generic plate

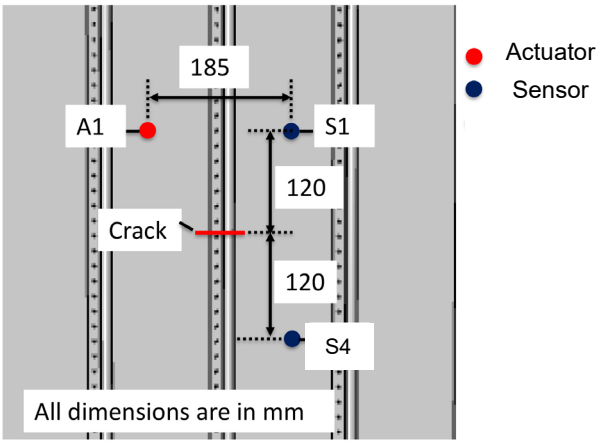

Figure 4.30 Actuator and sensor positions in the simulated model for stiffened panel

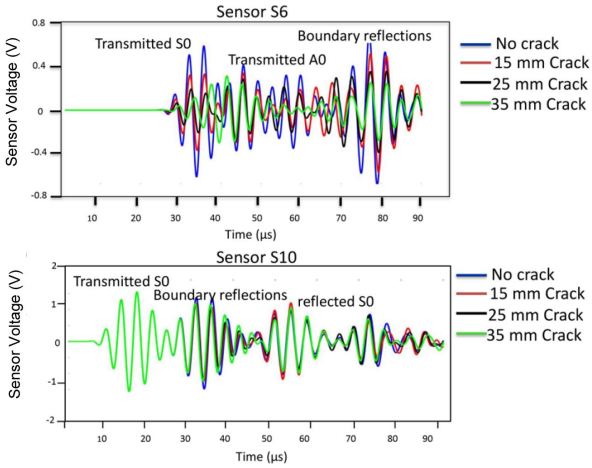

Figure 4.31 Received signals at sensors a) S6 and; b) S10 of Fig. 4.29

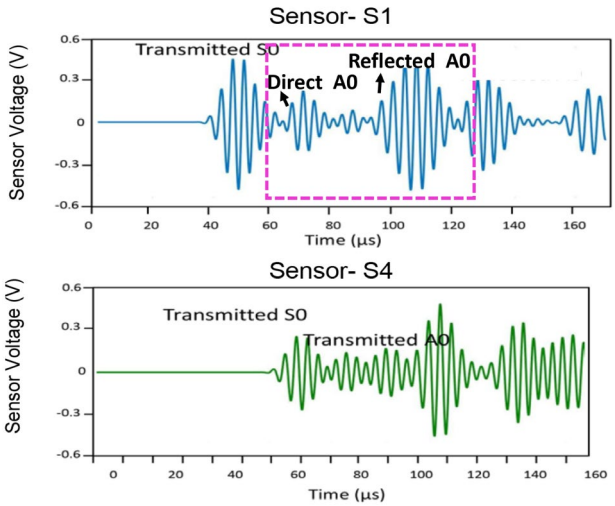

Figure 4.32 Sensor signals for stiffened panel at a) S1 position and; b) S4 position of Fig. 4.30

Damage detection based on guided wave signals has been reported in many references (Boller, Chang, & Fujino, 2009), (Gopalakrishnan, 2011), (Giurgiutiu, 2015) (Stepinski, Uhl, & Staszewski, 2013), (Lee & Staszweski, 2007) and (Rathod & Roy, 2011). The simplest form of identifying the presence of damage is by signal differentials where the current state of the signal is subtracted from the signal in the pristine condition. The higher the differential signals expressed in amplitudes, the more severe the damage is present and can be monitored. The damage index or damage metric value is used to measure the amount of damage present in the structure through the statistical processing of the resultant signal with the pristine state signals. If any damage is present in the structure, the spectral content of the signal is affected. The resultant scalar value is called a damage index. The simplest of the damage indexes one can calculate is Root Mean Square Deviation (RMSD) and the Correlation Coefficient Deviation (CCD). Various damage indices are applicable to guided wave signals and have been reported in (Taltavull, Sridaran Venkat, Boller, & Dürager, 2017). In the following, the damage index based on RMSD is discussed. It is expressed as in Equation 4.20. As shown in Fig. 4.33 more sensors are placed on the path of higher differential displacements. In this case sensors S1 to S10 for the generic plate and sensors S1 and S4 for the stiffened panel are considered.

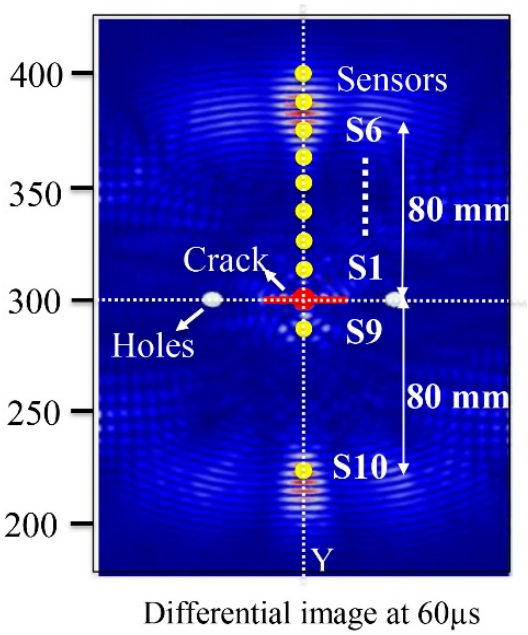

Figure 4.33 Various sensor positions for the calculation of RMSD

RMSD is calculated for all the different sensor positions for the generic plate. The result is shown in Fig. 4.34. Sensor S6 shows a higher damage index whereas sensors S9 and

S10 show a lower damage index. Fig. 4.35 shows the differential signals of sensor S6 for various crack sizes. It has to be noted that at close to 60 µs, for the crack size of 25 mm, a higher differential amplitude is obtained which is evident from the differential image shown in Fig. 4.33. From Fig. 4.34 it is evident that the sensor position S10 has a low RMSD value. The difference is due to the actuator position, which is closer to S10 than to S6 and also due to the constructive and destructive interferences of wave scattering.

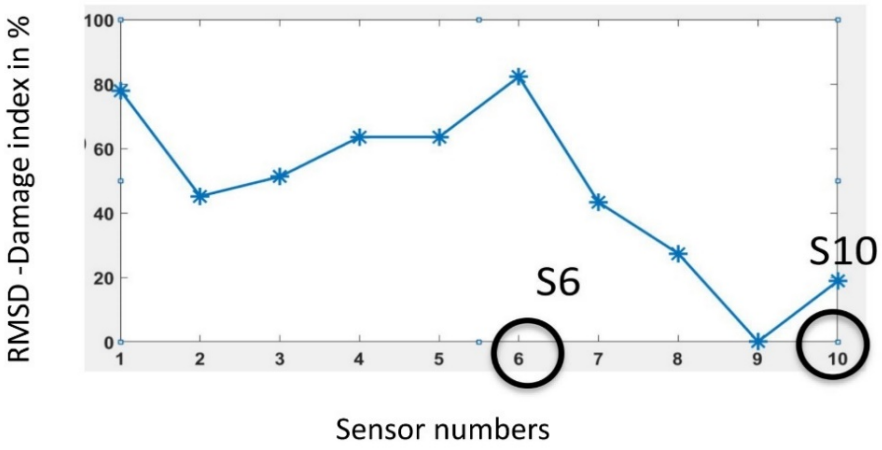

Figure 4.34 RMSD for various sensor positions

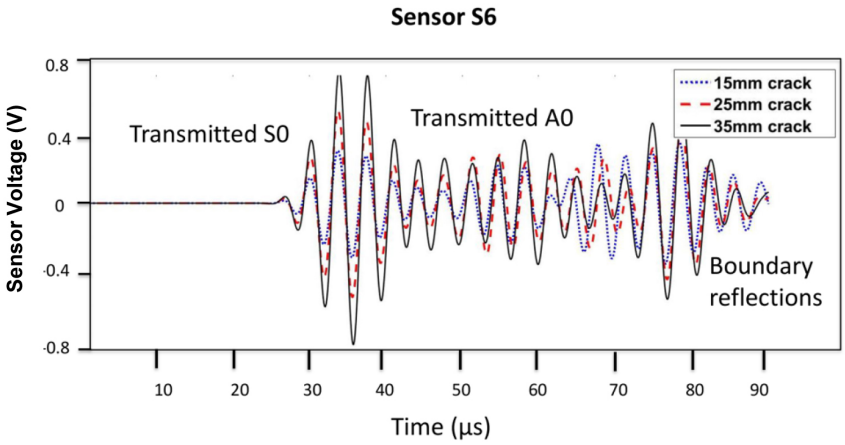

Figure 4.35 Differential signal of sensor S6 for various crack sizes

RMSD is given as,

$$\sqrt{\frac{\sum_N (S_i - S_i^0)^2}{\sum_N (S_i^0)^2}} = RMSD \qquad 4.20$$

where
S_i^0- is the frequency spectrum of the sensor signal in the pristine condition, and

S_i- is the frequency spectrum of the sensor signal in the damaged condition (crack 25mm length).

RMSD shown in Fig. 4.34 agrees with the differential image for the time at close to 60 μs. The RMSD (Equation 4.20) measures the deviation due to the presence of the damage in the signal.

4.6 Experimental Validation of Simulation

Once the hot spots for placing the sensors have been identified, experimental validation is carried out to validate the differential imaging method. An experimental setup is shown in Fig. 4.36 (a) for the generic plate. The actuator has been excited at ± 70 V using a frequency generator and a power amplifier. The oscilloscope reads the actuator and sensor signals, which have been digitised at a sampling rate of 10 mega samples per second. In Fig. 4.36 (b) one can observe the noise due to the electromagnetic field at the beginning of the measurement and this noise is mixed with the transmitted signal. The experimental results of S6 and S10 are shown in Fig.s 4.36 (b) and (c) in comparison with the simulated signals.

Fig. 4.37 (a) shows the stiffened panel mounted in the fatigue testing machine, with the actuator and sensor positions to be seen in Fig. 4.37 (b). The crack has been initiated in the middle of the test sample as shown in Fig. 4.37 (c). Transducer positions on the stiffened panel are shown in Fig. 4.38. To find out which of the sensors reacts with regard to the crack length propagating a correlation function has been defined as follows:

$$J(t) = Corr\big(x(t), x(t)\big)_{Auto} - Corr\big(x(t), y(t)\big)_{cross} \qquad 4.21$$

Equation 4.21 represents the difference between auto and cross correlation of the two signals *x(t)* and *y(t)* where *x(t)* is the signal of the pristine condition while *y(t)* is the signal of the damaged condition or where damage of a varying crack size has progressed over an increasing number of loading cycles. The correlation output attains a constant value after a certain size of the crack since there is no additional signal-packet spread due to increasing crack length. The result of the correlation output is shown in Fig. 4.39 plotted for various crack sizes when the experiment data had been taken for that additional sensors and actuators being embedded onto the stiffened panel as shown in Fig. 4.38.

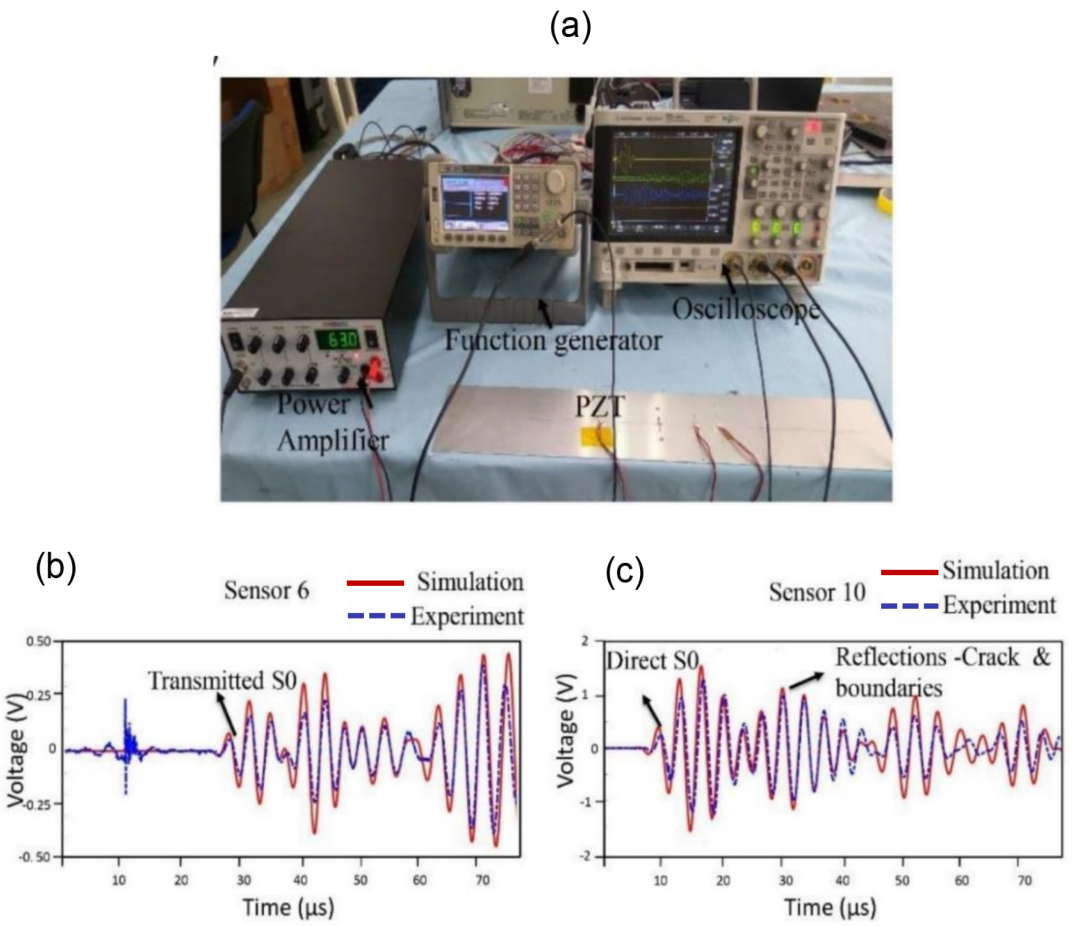

Figure 4.36 a) Experimental setup; b) Comparison of simulation and experiment for sensor 6; and c) Comparison of simulation and experiment for sensor 10

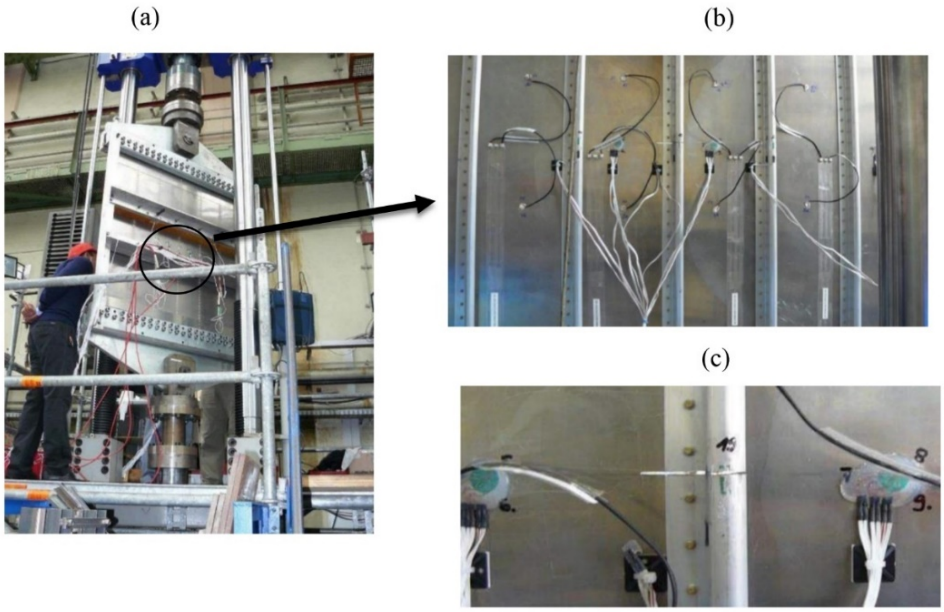

Figure 4.37 a) Experimental setup; b) Specimen; and c) Crack cut at the panel

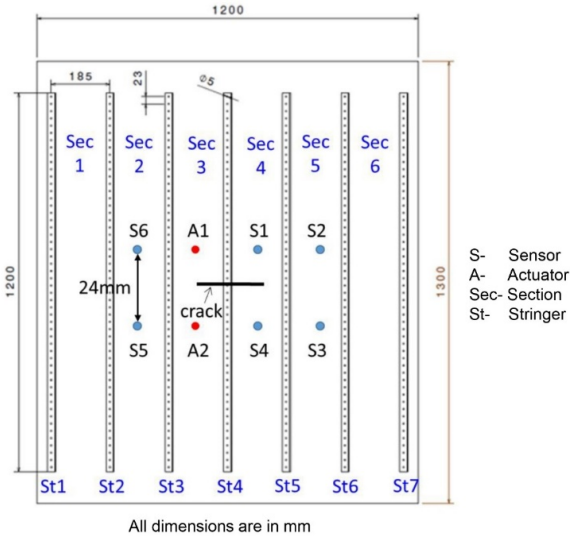

Figure 4.38 Sensors and actuator positions for calculating the correlation output on stiffened panel

Fig. 4.39 also shows that the correlation output for the sensor position S6 shows more correlation output for the crack sizes 50-80 mm in comparison to the S1 sensor position but when the crack size is larger than 80 mm, the S1 sensor shows a maximum correlation output as these results agree with the differential imaging. Due to the reduced geometry in the numerical model, the S6 position was not considered during the simulation. Simulated results of the stiffened panel for the S1 sensor position (Fig. 4.32(a)) reads well with the theoretical calculation of the direct and reflected A0 wave packets when calculated using the actuator, sensor and crack positions as shown in Fig. 4.30 respectively.

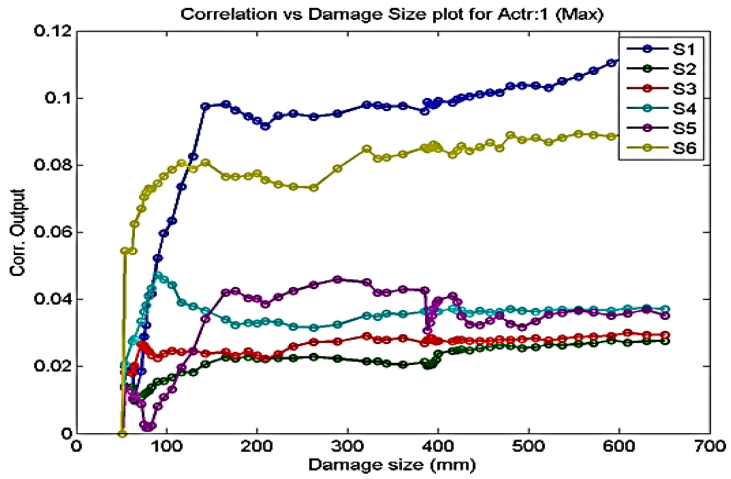

Figure 4.39 Correlation output as a measure of damage index for various sensor positions (Balajee Ravi, et al., 2016)

The calculated theoretical A0 mode velocity obtained from the dispersion curve at 200 kHz is 3140 m/s. Therefore, travel times for the direct and reflected A0 wave packets are 57μs and 95μs respectively. This can be verified with the Fig. 4.32(a) for the S1 position of the simulated results.

Due to computational constraints, stringers are not considered in the GW simulation models. In case if stringers were considered for the simulation, the effect of stringers in terms of optimum sensor positions would be negligible as the differential imaging would only highlight the maximum differential displacement points for a given tolerable damage and not the effect of stringers.

Chapter 5

Configuration of a SHM Toolbox to Solve Structural Ageing Problems

5.1 SHM within the Structural Design Process

Following the design process described in Fig. 1.7 this process can be extended to a process chain, which has been described to some degree in (Boller, et al., 2017) and is shown in Fig. 5.1 below:

Figure 5.1 Design process chain for structural assessment

The different elements of this process chain represent essential elements in the design process, which are first subject to a simulation being usually numerical to provide flexibility with regard to the approach. The results of such an approach are then finally validated through experimentation, which requires hardware tools as well. With all of this numerical simulation and experimentation data are generated, which need to be processed in an adequate way. Although SHM in the above process chain is shown as a single element and is widely defined as the integration of sensing and possibly actuation devices as such, it is still kept open what those devices should specifically end up with from a technology, logic, design and hardware point of view. When simply associating SHM with NDT, sensing is easily limited to damage detection only. However, when sensing is considered on a broader scope such as also sensing loads in general or strains in damage critical areas then SHM achieves a scope, which can easily encompass the complete design process being shown in Fig. 5.1. Establishing an SHM toolbox in that regard therefore may result in a multilevel approach for which the highest level can obtain a form as shown in Fig. 5.2.

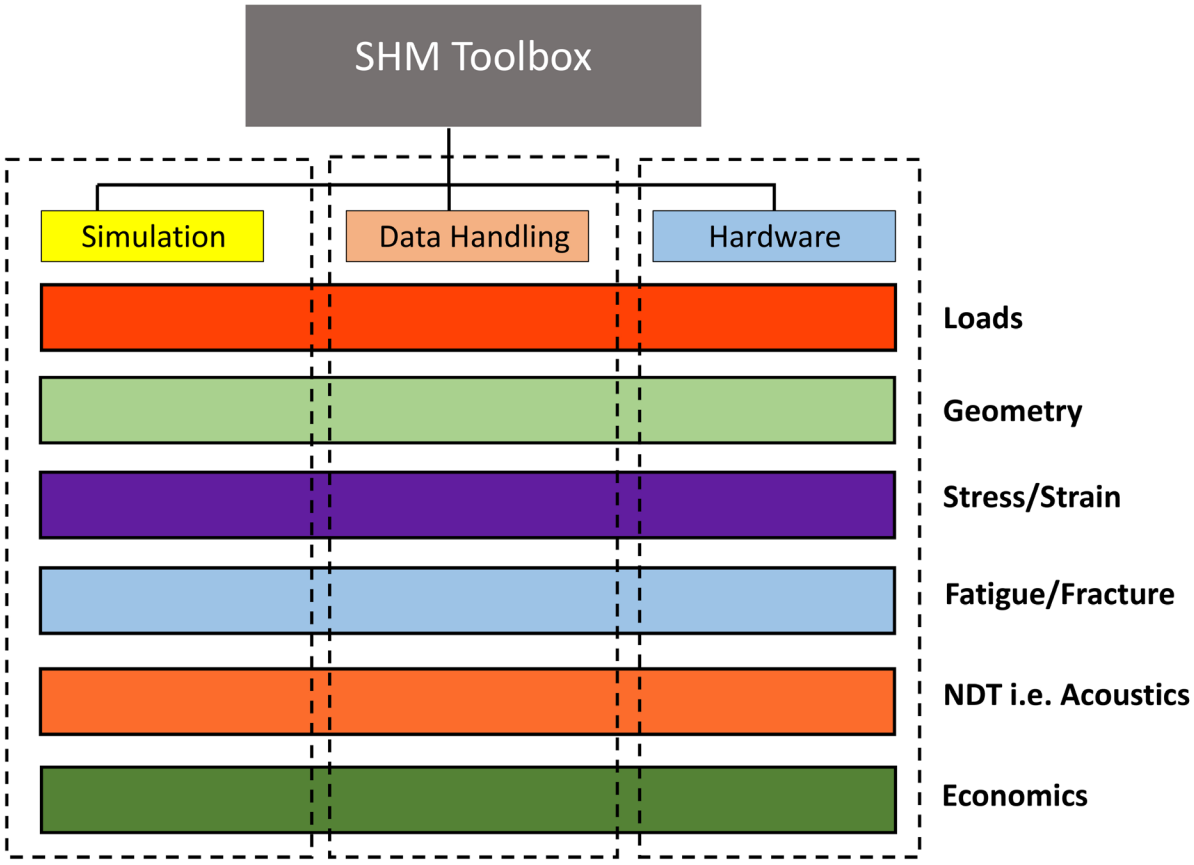

Figure 5.2 SHM toolbox structure from its highest level

It is beyond the scope of this thesis to fill all the elements shown in Fig 5.2. What will be demonstrated here is how the element 'NDT' can be gradually filled and what complexity stands behind making the toolbox to some degree complete in the end. Many of the techniques used in NDT can be considered for SHM. Those being of interest include acoustic emission, eddy current, electromagnetics, microwave/radar, optics including visual, thermography, ultrasonics, and vibrations in terms of modal analysis. Only a limited number of those are intensively followed up within the context of SHM so far, which may have different reasons. However, due to the inheritance of SHM into NDT no completeness of a potential of a SHM toolbox can be claimed here but rather the principle on how to structure such a toolbox such that it can be continuously filled with the respective tools in accordance to their availability and structural assessment needs. The following example elaborated and shown here is therefore limited to acoustic methods only but can be taken as a template for any future extensions in terms of alternative techniques such as having been mentioned above.

5.2 SHM Toolbox Using Acoustic Methods

There have been many research activities in the field of ultrasonic NDT, either in terms of damage or material characterisation using phased array transducers and methods such as Sampling Phased Array (SPA) or Reverse Phase Matching (RPM) described in the chapters before. These have been used for metals as well as for composites in the past. Most of this work has been performed in the context of bulk waves. Different methods applied consider non-linear acoustic analysis used when it comes to anisotropic materials such as composites (Solodov, Krohn, & Busse, 2002) and (Ooijevaar, 2014.) to detect early damage (i.e. fiber breakage, micro delamination). Research in guided wave analysis has been widely triggered by their advantage of monitoring large planar structures using low-cost surface mountable piezoelectric patches. However, in the past, these methods (non-linear analysis, bulk waves and guided waves) have been applied individually for specific composite applications and none of them were applied as a combination. It is therefore important to highlight that when these methods are combined by taking the advantage of one over the other, a simulation platform, specifically in view of SHM, could be useful. In an attempt, the work presented here will try to provide an 'umbrella' under which at least a majority of such methods can be integrated. This could bring numerous advantages in terms of a holistic monitoring of structures together where the case of ageing composite structures will be specifically addressed here.

This thesis intends to make some contributions in establishing an acoustics based toolbox allowing SHM systems to be designed and developed by inheriting knowledge available or developed in classical NDT. Based on the structure of the SHM toolbox described in Fig. 5.2 the different descriptions and developments for the different sub-modules and hence tools can be found in the different chapters as to the overview given in Fig. 5.3. Simulation related aspects are therefore considered with regard to anisotropy in composite materials (Chapter 2), non-linearities resulting from delaminations (Chapter 3) and handling of guided wave results (Chapter 4). Hardware related aspects include a function generator, power amplifier, SPA hardware, phased array transducers and PZTs to perform SPA. As to the data handling sub-module contributions inputs are related to SPA and RPM (Chapter 2), the use of non-linear characteristics (Chapter 3) and the application of differential imaging and sensor placement optimisation (Chapter 4). Finally different

vibration/acoustics based methods are addressed including phased array and SPA (Chapter 2), modal analysis and resulting higher harmonics (Chapter 3) and ultrasonic guided waves (Chapter 4).

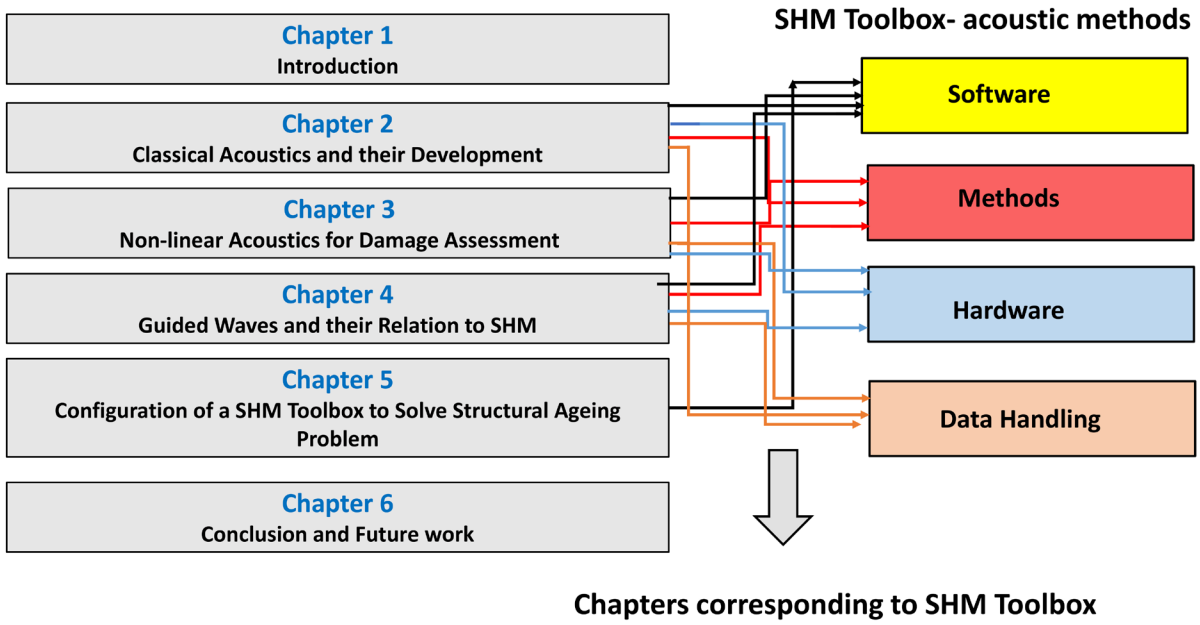

Figure 5.3 Relationship between SHM Toolbox and acoustic methods described in the thesis

Fig 5.4 is a trial to summarise how the NDT related information and technology available in acoustics can be made available to design and develop an acoustics based SHM system. Starting from the methods being available such a module is divided into the three sub-modules already presented in Fig. 5.2. Since SHM can be part of a NDT solution where the sampling of information is limited due to its transducers being fixed to defined locations, this fixation requires an optimisation process to be gone through prior to hardware realisation of the SHM system under consideration. This optimisation process, which is achieved in classical NDT through continuous sampling until the volume to be inspected has been fully covered, can only be solved through simulation and possibly intelligent signal processing. As a consequence simulation is considered as the first sub-module in such a toolbox followed by hardware, with data handling including signal processing serving as a linking sub-module between the simulation and hardware sub-modules. Within the simulation sub-module, specifically when considering the complete process chain shown in Fig. 5.1, various design and simulation tools are to be considered to carry out digital modelling, including a CAD based component's geometry, stress/strain

analysis, fatigue analysis and NDT/SHM simulations. NDT/SHM being in the focus here mainly includes piezoelectric driven acoustic wave generation transducers either resulting in bulk or more often even in guided waves. Further considerations do also include the acoustic wave being generated by electromechanical transducers, lasers or through air coupling. Another acoustic technique to be mentioned here is acoustic emission, which is the passive monitoring option when compared to the active acousto-ultrasonic part.

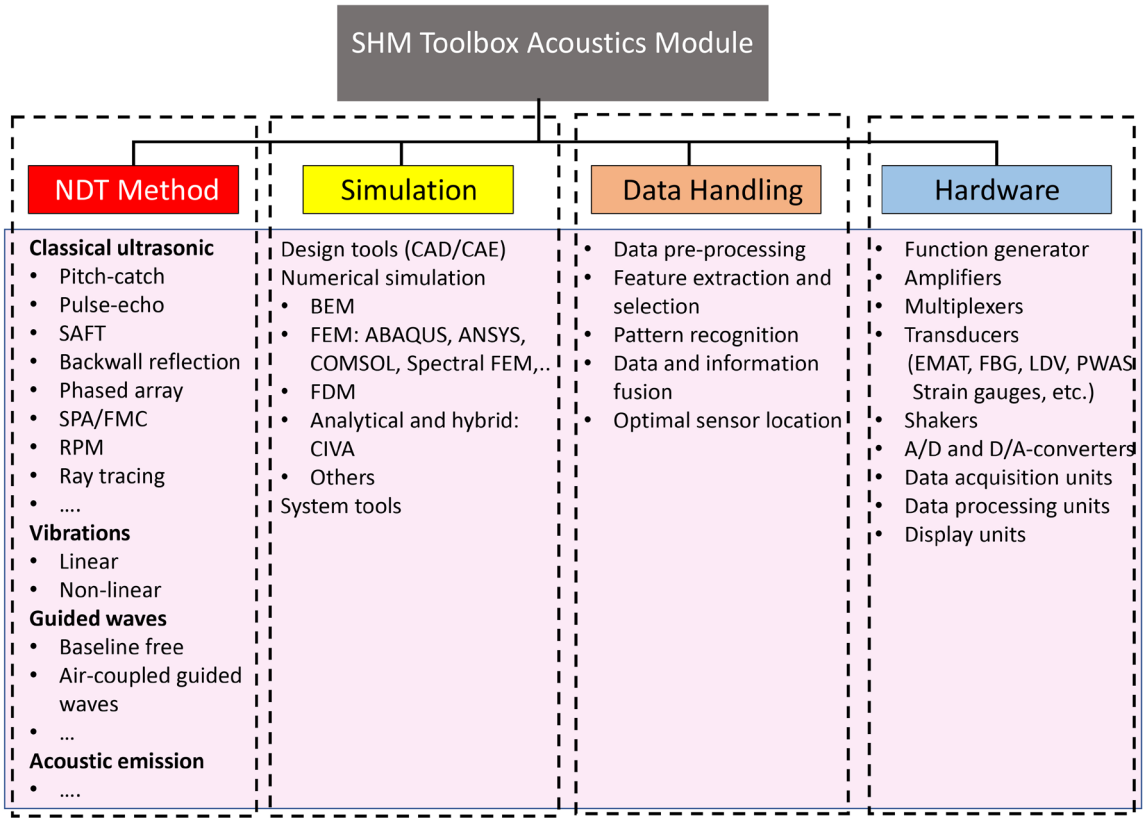

Figure 5.4 Structure of SHM toolbox for acoustics based SHM system design

The hardware sub-module involves the transducers, wiring and various electronic components allowing signals to be generated, amplified, multiplexed, recorded, processed and displayed. Once the data is generated from the hardware, they need to be processed along the data handling sub-module to obtain useful information about the condition of the structure. This includes mainly signal and image processing modules to handle the data obtained from the hardware components on the one hand and to compare them with data having been obtained through simulation on the other. The five consecutive aspects addressed in the data handling sub-module have been derived from a wider signal analysis point of view such as it has been described in (Staszewski & Worden, 2003) .

Within those aspects there is another multitude of techniques, which is summarised in Fig. 5.5 and which underline and describe the importance of the data handling sub-module.

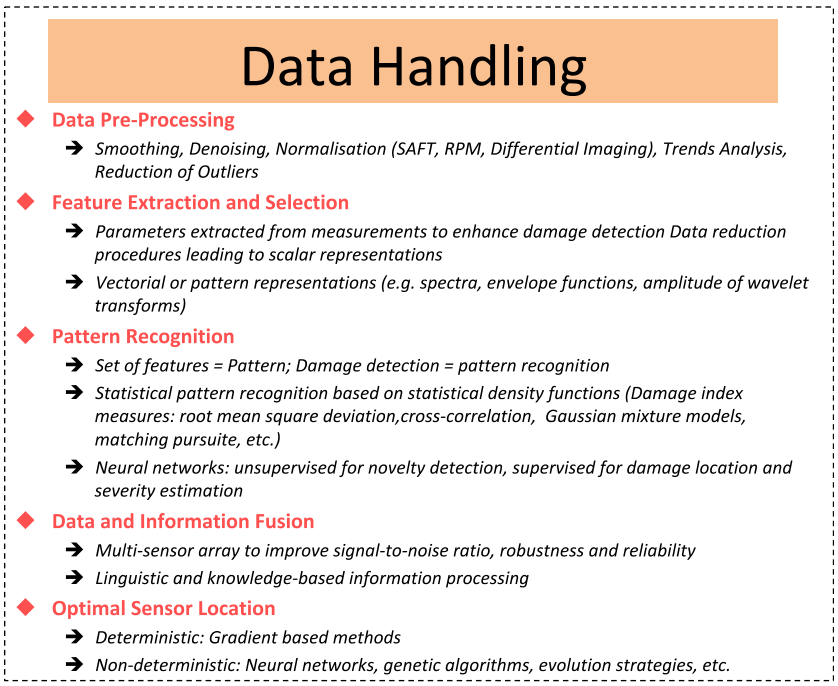

Figure 5.5 Options and techniques to be considered regarding sensor signal data handling

What is not considered in the approach in this thesis are the economic factors such as the analysis of the life cycle cost of the structure considered.

Once such a toolbox is sufficiently filled with the respective tools, assessments and designs of SHM systems can be considered where the case of an SHM system for ageing composite structures is an example being very much of interest to be analysed and demonstrating how to fill and validate the toolbox. This may build the basis for a concept encompassing NDT, simulation and a SHM system, possibly with a residual life management concept to be established in the end.

Fig. 5.4 claims the application of the different methods, which have been integrated into the SHM toolbox in this thesis. Considering all the elements corresponding to the toolbox modules when integrated as a system will allow a holistic assessment procedure to be realised in the sense of SHM in the context of dealing with ageing composite structures.

5.3 Approach to Handle Ageing Composite Structures

Polymer based composite materials are increasingly used today. Some of the structures made from these materials have already achieved the end of their operational life and as such have become subject of recycling. However, since the operational life of structures can vary significantly there are situations that can be anticipated in the future that structures with very long-life cycles can become subject of a structural reassessment. Such issues are currently becoming increasingly relevant in the context of civil infrastructure with materials such as steel and reinforced concrete. However, similar situations may be anticipated with polymer-based composites in the future and it would therefore be good to already have some relevant solutions available. A solution on how this could be solved is therefore given below.

The case to be considered here is a composite structure of which the material properties including the stacking sequence is unknown and which has been designed safe life the way polymer based composite structures have been designed in the past. Starting from this condition an approach is now proposed where the logic of developing the SHM system can be summarised as sketched in Fig. 5.6.

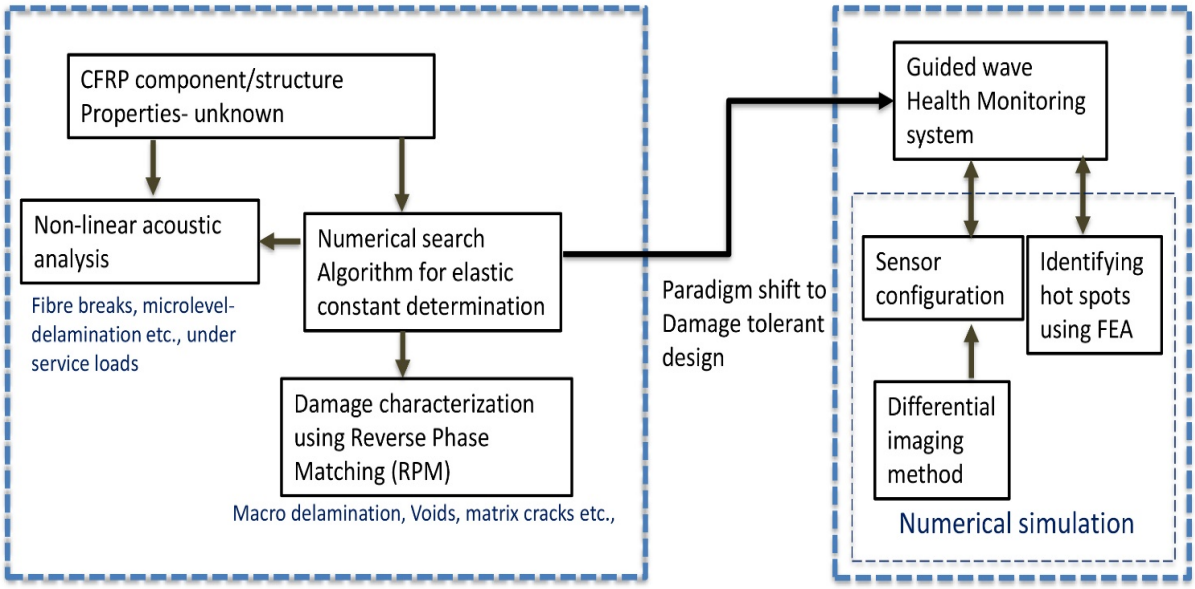

Figure 5.6 Integration of various NDT methods in the thesis

A core element in this process is numerical simulation combined with advanced sensor signal processing for which the process can be summarised in the following ten steps:

1. Numerical search algorithm for material characterisation using SPA and RPM.
2. The RPM method for damage characterisation of anisotropic materials.
3. The backwall reflection method to identify the severity of anisotropy.
4. Development of ray tracing methods for single layer, multi-layers and complex geometries.
5. Development of numerical simulation models to study the non-linear behaviour of composites under operational loads.
6. Damage index measures for characterising the severity of damages.
7. Quantification of incumbent damages using inversion with the data from the simulation.
8. Numerical model for simulating guided waves using COMSOL-Multiphysics in the context of damage tolerant design.
9. Differential imaging method to identify the higher differential displacements to optimise the sensor locations for a given tolerable damage.
10. Validation by experiments.

The way on how to get this detailed for the different steps is described in the different sections below.

5.3.1 Numerical Search for Material Characterisation (Steps 1 to 3)

In this context an iterative algorithm using a MATLAB tool for estimating elastic constants of an unknown CFRP material is introduced. The accurate reconstruction of an image (sector scan) using the data obtained from SPA along with RPM is only achieved when the elastic constants are known for the composite material under inspection. In the case considered here, the elastic constants are not known and they are not required for the conventional ultrasonic methods using A, B, and C-scans because one only needs one velocity in the thickness direction which is usually obtained by correlating the thickness measured by the signal and the actual thickness of the component being inspected. Ultrasonic methods have been widely used for the characterisation of isotropic and anisotropic materials for many years. (Balasubramaniam, 2005) and (Balasubramaniam & Whitney, 1996) used a through transmission ultrasonic goniometric technique for

measuring the elastic constants for a unidirectional laminate. Kline (Kline, 1992) used sectioning techniques for measuring the elastic constants. For thick composites one direct way of approaching the problem is to section the material in such a way as to take an optimal advantage of the symmetry of the problem. The same author also introduced a simplex method for the determination of elastic constants using ultrasonic data for the orthotropic symmetry. However, these methods are based on the experimental setups specifically designed for obtaining few or all of the elastic constants and it requires time and cost. In contrast to experimental techniques Pudovikov (Pudovikov, 2013) has developed the Gradient Elastic Constants Descent Method (GECDM) for obtaining elastic constants for inhomogeneous anisotropic materials with unknown elastic constants. This method is developed for inspecting austenitic weld materials whose elastic constants are usually not known prior to the inspection. This technique is based on iterative adjustment of material properties based upon the result of the known reflector position. The detailed description of this technique can be referred to in Pudovikov's thesis. A similar approach has been developed in this thesis for the estimation of elastic constants except the minimisation function that was used in GECDM. To implement this algorithm, reference reflectors (flat bottom holes, side-drilled holes) or any structural features such as rivets or sharp corners, notches etc., on the component should be known. In this case, the flat bottom hole has been used as a reflector. The values of the elastic constants $\mathbf{C}_{11}$, $\mathbf{C}_{13}$, $\mathbf{C}_{33}$, $\mathbf{C}_{44}$ and $\mathbf{C}_{55}$ are assumed for a given transversely isotropic medium. With the help of a ray tracing algorithm and data from the SPA, the images are reconstructed from the SPA data for various combinations of elastic constants. Each iteration gives one reconstructed image for a specific combination of elastic constants.

The values of those elastic constants are changed for the subsequent iterations. Once all the iterations have been finished, the corresponding images are stored in a matrix. Within this algorithm, a sub-routine (search function) is written to check whether the position of the reflector present in the image is correct or not. This sub-routine has predefined information about the position of the reflector. It looks for the region of interest where the coordinates of x and y are minimum and the amplitude of the reflector is higher. When these conditions are met, the images are segregated. Finally, the image that has the correct location and size of the flat bottom hole will have the correct set of elastic constants. These elastic constants are then taken for the reverse phase matching algorithm, which

is explained in Chapter 2. The block diagram of the numerical search algorithm is shown in Fig. 5.7. The algorithm has two phases. One is used to generate and save the images and the second phase is used to analyse the stored images. There are around 10,000 iterations (10,000 images) for the test sample having been measured. The number of iterations depends on the initial estimations. There are four major loops for the elastic constants each starting from minor values and moving to the major values.

The difference between the numerical search algorithm and GECDM is the minimisation function. The GECDM uses the minimisation function, which reduces the number of iterations every time after each iteration is accomplished. The search function is a mathematical function, which has variables of x and y coordinates of the flat bottom hole and corresponding amplitude values. The variable S from Fig. 5.7 is a function of variables x, y and the amplitude. When the value of S is optimum it means that the selected image will have an exact location of the reflector and a high amplitude. The elastic constants corresponding to this image is the correct set of the elastic constants for this anisotropic material.

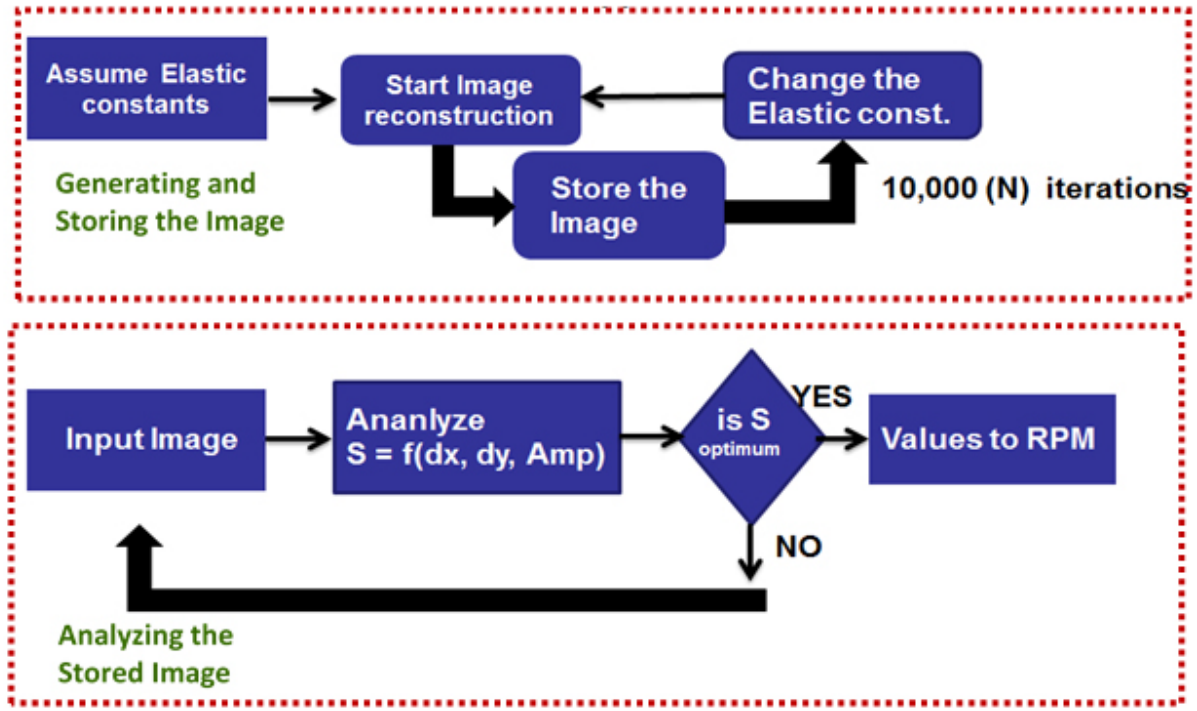

Figure 5.7 Flowchart of numerical search algorithm

In Fig. 5.8 the reconstructed images for each iteration are shown, thus resulting in N reconstructed images. The window for analysing the region of interest is shown in this

figure for a Ø 1 mm flat bottom hole. The search function identifies the correct image for the given condition. The elastic constants for the sorted image are automatically retrieved for the known iteration where the elastic constants are assumed. The elastic constants are C_{11}=158.1, C_{13}=7.0, C_{33}=13.0, C_{44}=3.0 and C_{55}=6.8 with units being in GPa. The density is 1600 g/cm3. The values obtained are fed into the reverse phase matching algorithm for image reconstruction.

Determining the elastic constants is a first important step, which needs to be performed with the classical phased array ultrasonic technique. This analysis may be extended in case of detecting a stacking sequence if an option exists to analyse the component and hence material in a possibly up to two-digit MHz range or in a very specific shear mode. Alternatively, the elastic constants can just be determined in a homogenized form (Deydier, Leymarie, & and Calmon, 2005), which will then also build the basis for any subsequent numerical simulation.

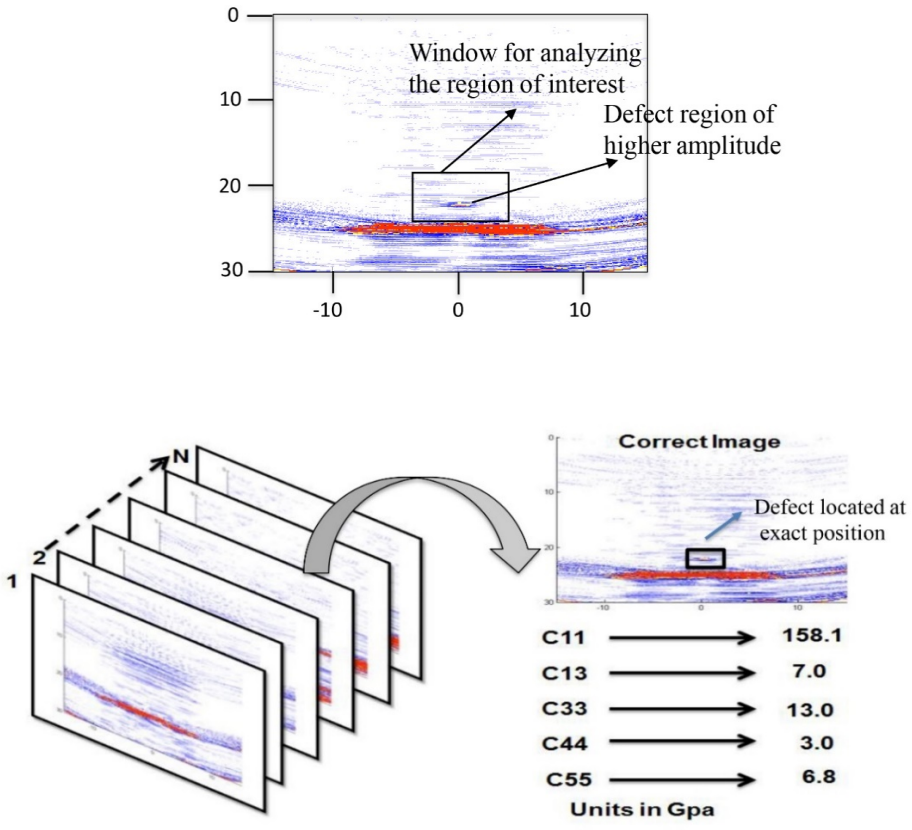

Figure 5.8 Resultant images of the numerical search algorithm

Fig. 5.9 shows the comparison of velocity distributions between the experimental back-wall reflection technique and the numerical search algorithm for the angle range between -30° to 30°.The difference between the two approaches is less than 10%.

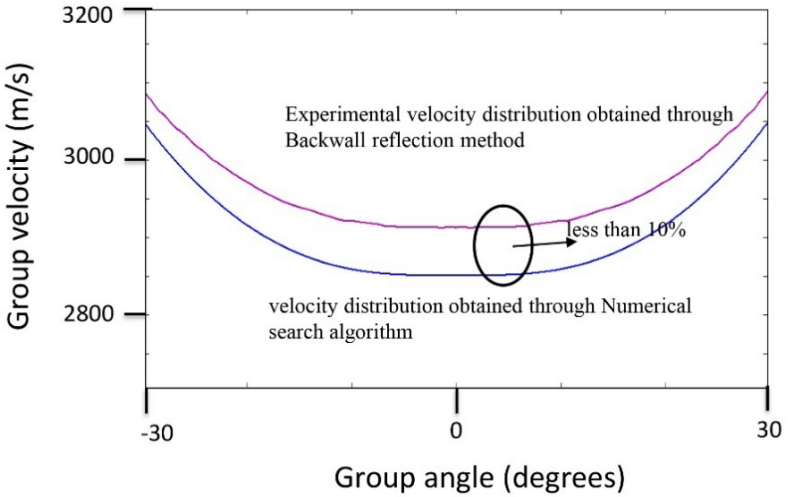

Figure 5.9 Group angle versus velocity distribution for a 64-element PA transducer

5.3.2 Ray Tracing for Time Efficient Wave Simulation (Step 4)

In view of speeding up the numerical wave propagation process it is essential to have a ray tracing procedure available that allows the propagation of acoustic waves travelling in the structure to be simulated in an appropriate way preferably in near to real time. In case a layer per layer analysis of the composite material is possible then an ultimate condition would be met. However, a homogenized model looks to be more realistic in the first place.

5.3.3 Simulation of Structural Non-linear Behaviour (Steps 5 to 7)

Once the CFRP component considered can be described in terms of its materials properties and hence anisotropic behaviour different possible damages can be included in the numerical simulation models and the component's dynamic response in terms of a frequency or a related factor can be determined. An important question in that regard is the way on how such an approach can be applied for a very large complexly shaped component. In such a case, where critical damages usually emerge in localised regions a proper understanding of the local structural behaviour is required, not only from the structural response point of view but also from the way it would have to be actuated. This analysis

would possibly derive where potential (i.e. piezoelectric) actuators would have to be placed such that the appropriate structural dynamic response would be obtained.

5.3.4 Simulation of Structural Behaviour in Terms of Damage Tolerance and Guided Wave Propagation (Step 8)

If a structure is due to be damage tolerant then its damage tolerance potential (i.e. size and location of the damage) has to be defined. This has to be done in the context of a static strength analysis where the ultimate limit load has to be applied to the damaged structure without leading the structure to collapse. In case that this condition is met the tolerable damage can then be defined in terms of location and size and simulations of acoustic waves travelling can be performed for the undamaged and the damaged condition followed by differential imaging along which of the sensor locations are found to reliably detect the tolerable damage. Fig. 5.10 shows the generic plate with three holes and a crack now made of a CFRP composite material.

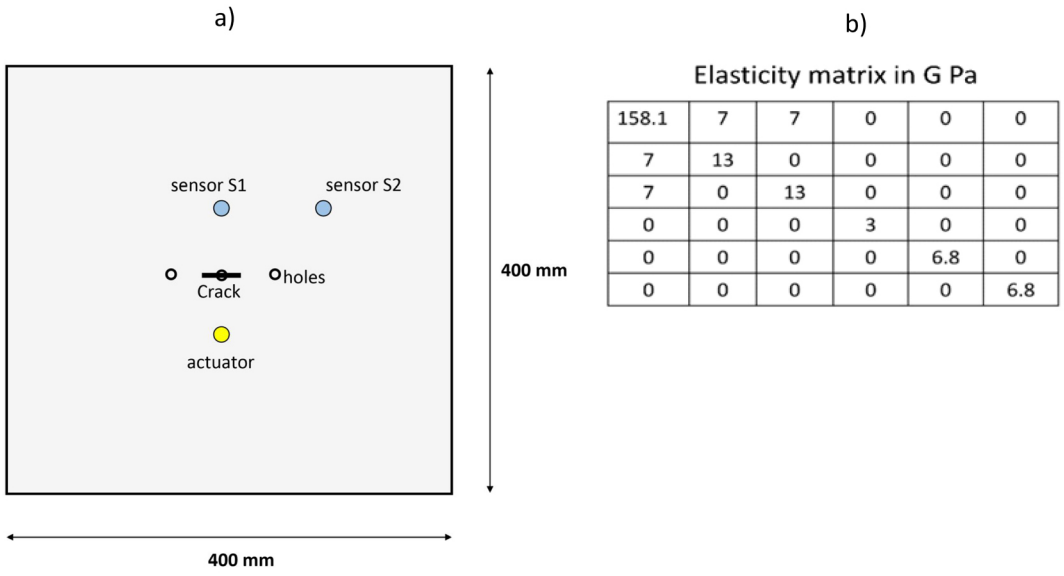

158.1	7	7	0	0	0
7	13	0	0	0	0
7	0	13	0	0	0
0	0	0	3	0	0
0	0	0	0	6.8	0
0	0	0	0	0	6.8

Figure 5.10 a) Composite plate; and b) Elasticity matrix as obtained using iteration

The results of the wave propagation at various time intervals for the CFRP plate with a damage of a 50 mm cut at the centre of the plate are shown in Fig.s 5.11 (d, e and f). The elasticity matrix as shown in Fig. 5.10 (b) has been obtained through the numerical search algorithm described above. From Fig. 5.11 one can understand that in anisotropic material the wave propagation is not circular like in isotropic materials.

One of the important aspects in the wave propagation is the group velocity of the various guided wave modes. They are identified by means of measuring the arrival time and the known distance between the actuator and sensor positions. The group velocities obtained from simulation can be verified by means of theoretical calculation of the dispersion curves.

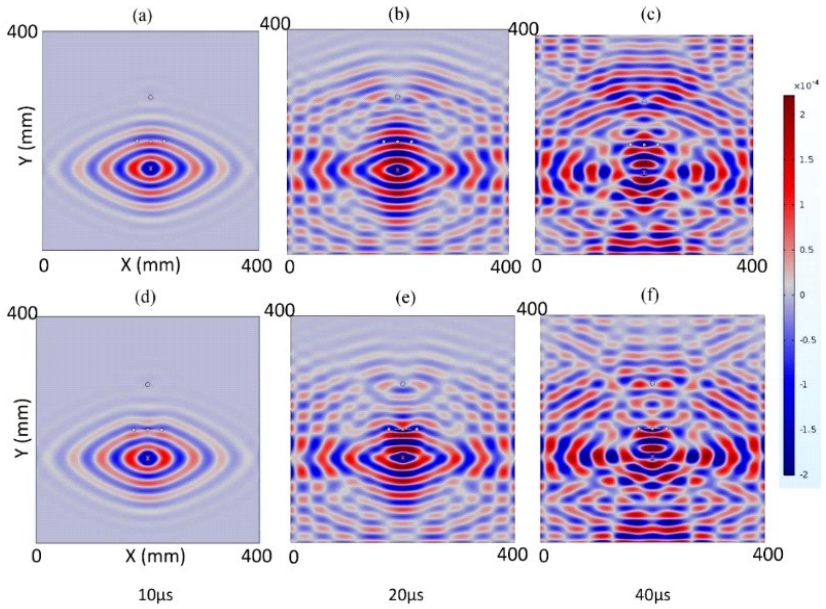

Figure 5.11 Wave propagation in CFRP plate at various time steps for undamaged cases: a), b) and c); For the crack at the center d), e) and f)

5.3.5 Differential Imaging and Experimental Validation (Steps 9 and 10)

Differential imaging results of a CFRP plate are shown in Fig. 5.12. Here, two sensor points as shown in Fig. 5.10 (a) have been identified for analysis. Sensor position S1 has a high magnitude and direction of the residual displacements and sensor position S2 has relatively low differential displacements when compared to S1 position. For composite specimens, the group velocity varies according to the elastic properties as shown in the simulated results. It is very essential to note that the sensor locations should be selected according to the direction where the group travels. Following the differential images as shown in Fig.s 5.12 (a) to (c), the hot spots exist in the direction parallel to the length of the damage. The received signals in Fig. 5.13 for the S1 position shows that the amplitude is much higher than for the S2 position (Fig. 5.14). This can also be observed when comparing the differential signals for the case of S1 and S2 (Fig. 5.15). While a significant difference can be observed for S1 the difference in the case of S2 is rather marginal.

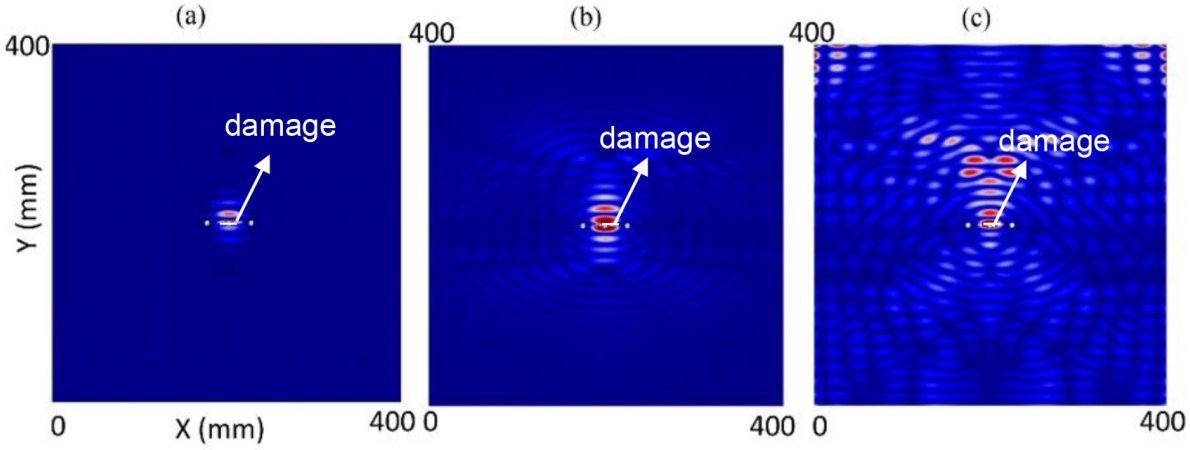

Figure 5.12 Differential images at: a) 10 μs; b) 20 μs; and c) 40 μs

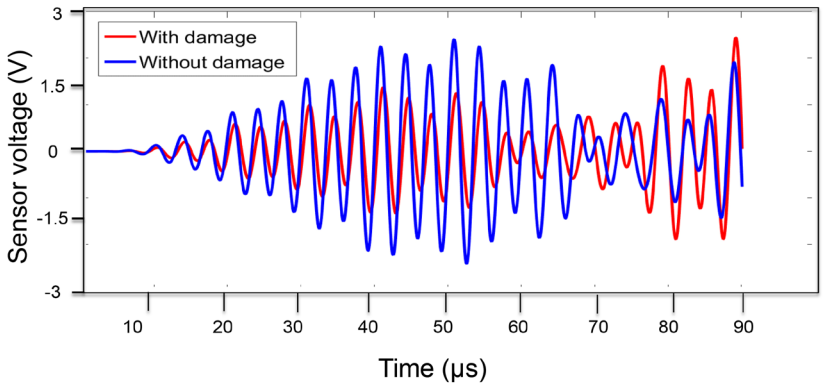

Figure 5.13 Received signals of sensor position S1

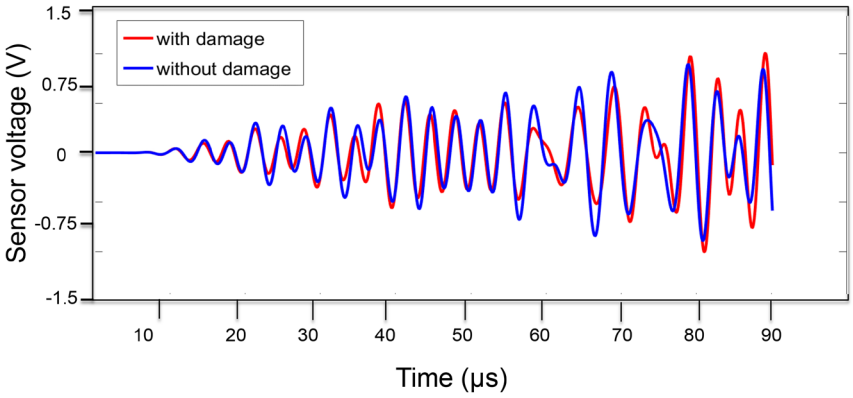

Figure 5.14 Received signals of sensor position S2

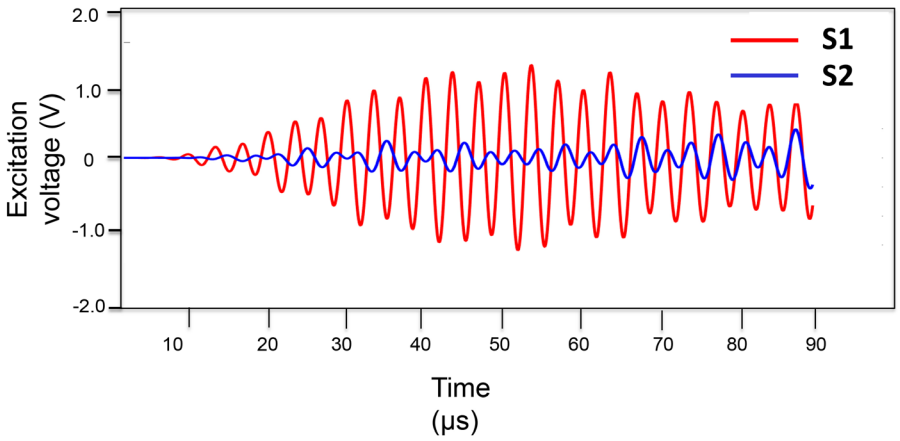

Figure 5.15 Differential signals: S1 (red) position and S2 (blue) position

Based on the information obtained above and an actuation configuration set one is now able to provide a sensor pattern that can be taken as a basis to configure the resulting sensor pattern, then to be realised as a SHM system in hardware and finally used for experimental validation. It may be worth mentioning, that in the case of a SHM system with a network of transducers methods like SPA and RPM may be worth to be applied as an additional information source allowing possibly the monitoring potential of the SHM system to be enhanced.

5.4 Guided Wave Dispersion Diagrams as an Alternative to Assess Ageing Structures

(Rojas, 2011) and (Gao, 2007) have studied the mechanical and physical properties of a metallic materials due to various ageing processes. (Rojas, 2011) studied the characteristics of Young's modulus on aluminium alloys due to thermal ageing. Fig. 5.16 shows that, as the temperature is increased, the value of Young's modulus tends to reduce.

Since the group velocity is dependent on Young's modulus, any change in Young's modulus will certainly affect the group velocity, which can be seen in the dispersion diagram as shown in Fig. 5.17 where the group velocity dispersion curves are shown for two different Young's moduli calculated by the CIVA-Guided Wave module.

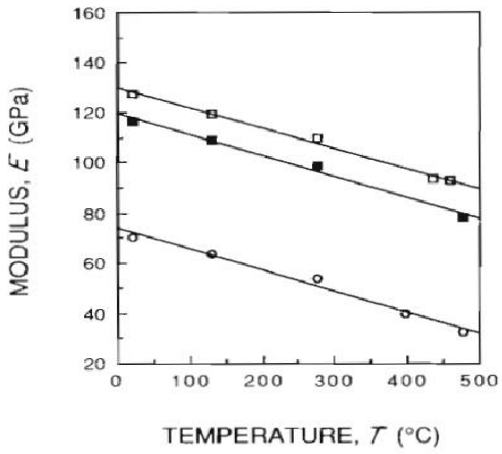

Figure 5.16 Reduction of Young's modulus due to thermal ageing of aluminium (Rojas, 2011)

(Rojas, 2011) and (Gao, 2007) have proven that any of the following parameters E (Young's modulus), density and thickness affect the group velocities, which is obvious from the guided wave constitutive equations. Any change in the above parameters can certainly be due to the effect of damage occurring as a result of ageing, as already stated in Chapter 1 (Fig. 1.3).

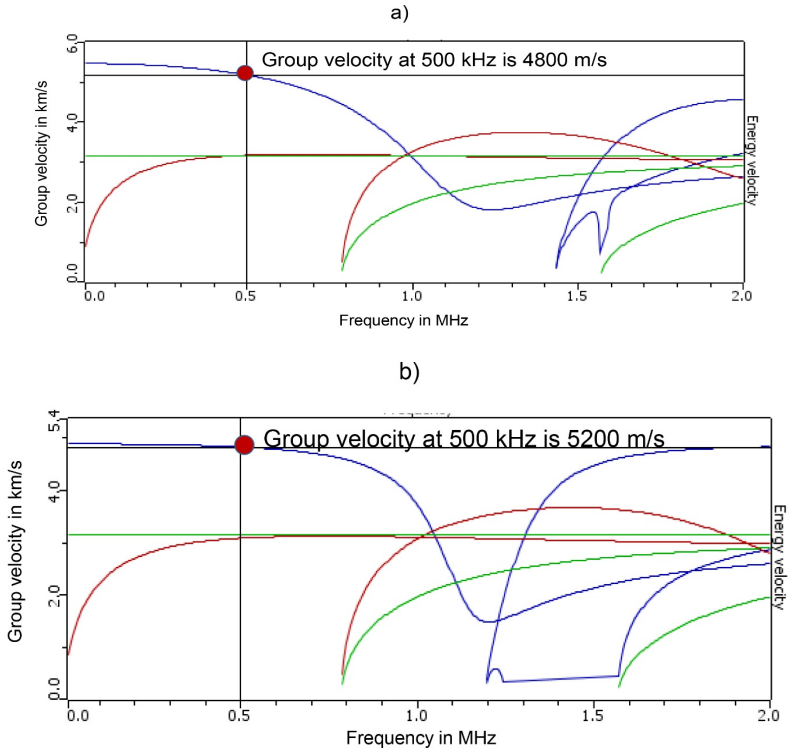

Figure 5.17 Difference in group velocities of dispersion diagrams due to ageing calculated using the CIVA-GWT module: a) Dispersion curve for reduced E-modulus; and b) Dispersion curve for actual Young's modulus (prior to ageing).

By means of calculating the dispersion curves at various intervals through experiments and comparing the various dispersion plots for different damage conditions, one can observe where differences in the dispersion diagramme become obvious and how measurements with a SHM system have to be performed such that the effect due to ageing can be well identified. This becomes obvious when comparing the two dispersion diagrams shown in Fig. 5.17. In a similar way, density and thickness reduction as a result of ageing can also be identified. A frequency sweep can be performed using a frequency generator and the arrival time is measured from the signal while the group velocity can be calculated by knowing the distance between the actuator and the sensor. In a similar manner, the dispersion analysis of composites was studied by (Gao, 2007).

Chapter 6

Conclusion and Future Work

6.1 Conclusions

In the scope of this thesis, the acoustic methods have been developed and integrated into the SHM toolbox (section 5.2 from Chapter 5) for holistic monitoring explained in view of assessing ageing composites structures. By means of SPA-RPM approaches, the true elastic constants of an anisotropic material can be determined with the help of known reflector locations. However, the stacking sequences and layer orientations could not be considered in this thesis due to computation limitations. Homogenised elastic constants have been used instead so far to determine the respective wave velocities in an anisotropic medium.

Even if the anisotropic and hence respective elastic properties would be known it would still be highly difficult to get those included in an acoustics based SHM system that would appropriately track the waves disseminated in the anisotropic material and structure. In case the wave propagation in that anisotropic material and structure could be correctly described and hence damage be detected through a differential signal determined through the difference between the signal for the undamaged and the damaged condition then it remains unclear when the damage would appear due to the randomness of damage incubation. Design and realisation of a SHM system for an ageing anisotropic structure and/or component is therefore a difficult task that can possibly only take place after a series of steps as shown in Chapter 5 (section 5.3) including a remarkable portion of simulation to be done along the realisation process of the SHM system.

Fig. 6.1 shows that the configured toolbox can be even extended to prognostics tools for a remaining life estimation of a structure. Then the data from both diagnostics and prognostics will flow to a potential operations and maintenance department where a predictive action can be taken either to extend the service life of the structure or to repair/ recycle the structural components. Technology maturity level of ultrasonic NDT methods described in this thesis is relatively high when compared to guided wave SHM and vibrational methods. Inheriting NDT methods similar to SPA-RPM into the SHM domain will

lead to enhance the SHM based monitoring approach in resolution and can be applied not only for ageing composites but any other application where SHM plays a role.

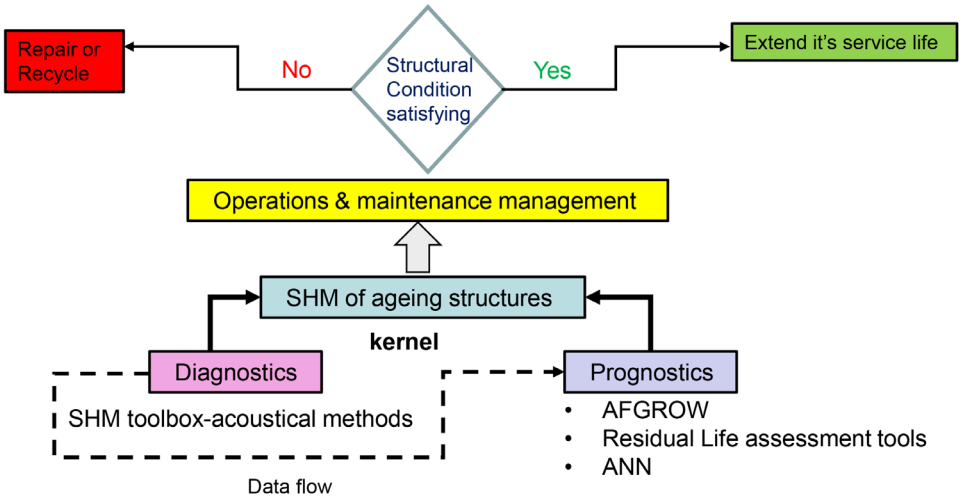

Figure 6.1 Combination of diagnostics and prognostics toolboxes

In summary, it has to be stated that a continuous screening of developments in NDT can have a significant positive impact on SHM developments specifically when this is combined with structural design. This proves that SHM is not a discipline on its own but rather an integrative process that laterally integrates different disciplines to a mainly holistic entity.

6.2 Future Work

The main objective behind this thesis has been to develop classical NDT and to build the bridge to SHM in view of developing a monitoring solution for ageing composite structures using acoustic methods. In the context of sensor optimization, numerical models (GW-FEM models and the differential imaging method) have been established and partially validated with experiments with respect to steel structures. A similar approach is also possible for anisotropic materials and structures whose properties are characterized using SPA-RPM. The experimental validation of such approaches has to be considered as future work. The differential imaging method using numerical FEM simulation is effective in identifying potential locations for placing the sensors. The damage index analysis is an interesting means to be considered from the differential imaging point of view and also deserves further attention in the future.

Another important aspect to be considered is the numerical search algorithm using MATLAB and the determination of elastic constants and possibly more. In this thesis the homogenised elastic matrix, which means the layer properties (fiber orientation and layer thickness) of the laminate have been ignored. This is because the wavelength of the ultrasonic bulk wave is in the order of millimetres and the layer properties are in the micrometre range. There is a chance that one can increase the frequency of the ultrasonic bulk wave in the specimen but at the same time there is a possibility of high wave attenuation in the material. The methods to numerically obtain the homogenised elastic matrix have been studied by various authors (Deydier, Leymarie, & and Calmon, 2005), (Sridaran Venkat, Bulavinov, Pudovikov, & Boller, 2010) and (Kappatos, et al., 2017) and have to be considered state of the art. The NDE-simulation tool CIVA (CIVA, 2015) has a feature to model ultrasonic wave propagation in the laminated composites using the homogenisation method. To perform an experimental analysis, one needs an excitation frequency where a minimum number of guided wave modes exists. This can be accomplished by calculating the dispersion curves. However, the dispersion curves in CFRP material are not a direct solution because of anisotropic properties. Many authors explained a semi-analytical approach to calculate the dispersion diagram (Rokhlin & Wang, 2002), (Rokhlin, Chimenti, & Nagy, 2011), (Rose, 2014) and (Gao, 2007). The software DISPERSE allows one to calculate the dispersion curves for known elastic properties of a CFRP sample. Wave attenuation and the effect due to beam spreading needs to be considered for the guided wave inspection of anisotropic material (Sharif Khodaei, 2016). All of those constraints have been addressed recently and need a solution in the future. Wave propagation analysis for large composite parts may be time consuming because of higher degrees of finite element nodes so ray tracing methods combined with FEM in the sense of hybrids can be a solution for this problem.

The scheme described in this thesis is adapted for finding the optimal sensor position provided the actuator positions are known. However, a similar scheme could be used for optimising the actuator positions for a given tolerable damage. In this case, the input function (excitation signal), number of actuators and different PZT sensor shapes can well determine the optimisation scheme for the actuators. This method can be applied initially for isotropic and then for anisotropic materials respectively.

The differential images show higher differential points to form a contour of maximum differential signals and can be realised as the differential pattern for harvesting maximum

differential energy. The ground work has been prepared in the context of piezoelectric coating for the given tolerable damage (Bareiro Ferreira, Sridaran Venkat, Adam, & Boller, 2016) and (Rathod, Jeayseelan, Dutta, & Mahapatra, 2017) where the development of the fabrication process and characterisation of a BaTiO3/epoxy resin piezoelectric composite is described in detail. This can become an interesting option in case the differential imaging approach can be generalised, and additive manufacturing may get a breakthrough within the context of SHM systems to be printed on structures.

So far in the presented approach, external influences due to temperature and dynamic loading conditions were not considered in both the simulation and experiments. These external factors are also known as time-varying boundary conditions. For example, a minor change in the load condition can introduce large variations in phase and amplitude of the guided wave signal and in the end will affect the detectability of a guided wave signal. Environmental compensation methods have been proposed in the literature (Croxford, Moll, Wilcox, & Michaels, 2010). The work has already been developed to study the influence of load conditions in the guided wave signal through numerical simulation and experimental validation for an aluminium plate (Qiu, Sridaran Venkat, Boller, & Yuan, 2016). Such methods are further options to be included in the SHM toolbox also in view of getting extended to composite structures.

In the context of bulk waves, SPA along with RPM has been proven as an efficient tool for quantitative NDT. In a similar manner, the SPA principle in combination with RPM can be applied to an array of PWAS (actuators and sensors) to perform a quantitative guided wave SHM approach in real-time. This may yield a higher probability of detection of damages also in the case of anisotropic structures because the actual anisotropic properties of the structure or components can be considered while it undergoes ageing.

In summary the SHM toolbox is a scheme to provide structural integrity technology in a structured form with a variety of further options to be continuously filled in the future.

Bibliography

Achenbach, J. D. (1987), "Wave Propgation in Elastic Solids", North Holland, Amsterdam, Netherlands.

Auld, B. A. (1973), "Acoustic Fields and Waves in Solids", Wiley-Interscience, New Jersey, USA.

Auricchio, F., & Sacco, E. (1996), "Augmented Lagrangian finite elements for plate contact problems", International Journal for Numerical Methods in Engineering, Volume 39, 4141-4158.

Backe, D., & Balle, F. (2016), "Ultrasonic fatigue and microstructural characterization of carbon fiber fabric reinforced polyphenylene sulfide in the very high cycle fatigue regime", Composites Science Technology, Volume 126, 115-121.

Backe, D., Balle, F., Helfen, T. B., Rabe, U., Hirsekorn, S., Sklarczyk, C., Boller, C. (2012), "Ultrasonic fatigue testing system combined with online nondestructive testing for carbon fiber reinforced composites",In The Minerals, Metals and Material Society Supplemental Proceedings, Volume 2, 855-863, Orlando, USA.

Bagchi, S., Sridaran Venkat, R., Starke, P., Boller, C., & Mitra, M. (2015), "Monitoring early damage initiation of very high cycle fatigued composite material using a nonlinearities based inverse approach", 10th International Workshop on Structural Health Monitoring (IWSHM), Stanford University, DEStech Publications, Inc., USA.

Balajee Ravi, N., Chakraborty, N., Shivamurthy, R., Sridaran Venkat, R., Mahapatra, D. R., & Boller, C. (2016), "Simulation of ultrasonic inspection of defects in thick structural components", 8th International Symposium on NDT in Aerospace, Bengaluru, India.

Balajee Ravi, N., Chakraborty, N., Steckel, M., Betagiri, P., Raghuraman, P., Shivamurthy, R., Boller, C. (2016), "A Study on effectiveness of an SHM sensor system for fatigue damage inspection", 8th European Workshop on Structural Health Monitoring (EWSHM), Bilbao, Spain.

Balajee Ravi, N., Rathod, V. T., Chakraborty, N., Mahapatra, D. R., Sridaran Venkat, R., & Boller, C. (2015), "Modeling ultrasonic NDE and guided wave based structural health monitoring", Proceedings of the SPIE, Volume 9437, San Diego, USA.

Balasubramaniam, K. (2000), "Skewing of the acoustic wave energy vector in stacked 1-3 anisotropic material systems", Journal of Sound and Vibration, Volume 236, 166-175.

Balasubramaniam, K. (2005), "Ultrasonic goniometry immersion techniques for the measurement of elastic moduli", Journal on Composite Structures, Volume 67, 3-17.

Balasubramaniam, K., & Whitney, S. C. (1996), "Ultrasonic through transmission characterization of thick fibre-reinforced composites", NDT & E International, Volume 29 (4), 225-236.

Balasubraminam, K. (2000), "Skewing of the acoustic wave energy vector in stacked 1-3 anisotropic material systems", Journal of Sound and Vibration, Volume 236(1), 166-175.

Balle, F. (2013), "Ultrasonic Fatigue of Advanced Materials", Ultrasonics, Volume 53, 1395-1450.

Bareiro Ferreira, O., Sridaran Venkat, R., Adam, J., & Boller, C. (2016), "Development of the fabrication process and characterization of piezoelectric BaTiO3/Epoxy composite to be used for coated ultrasonic transducer patterns in structural health monitoring", 19th World Conference in Non-destructive Testing (WCNDT), Munich, Germany.

Bing, Z., & Greenhalgh, S. (2004),"On the computation of elastic wave group velocities for a general anistropic medium", Journal of Geophysical Engineering, Volume 1 (3), 205-215.

Bing, Z., & Min-Yu, D. (1999), "Incidence, reflection and transmission angles in anisotropic media", Acta Seismologica Sinicia, Volume 12 (4), 413-418.

Boller, C., Chang, F. K., & Fujino, Y. (2009), "Encylopedia of Structural Health Monitoring", John Wiley & Sons.

Boller, C., Roy Mahapatra, D., Sridaran Venkat, R., Balajee Ravi, N., Chakraborty, N., Shivamurthy, R., & Simon, K. M. (2017), "Integration of Non-Destructive Evaluation-based Ultrasonic Simulation: A means for simulation in structural health monitoring", Structural Health Monitoring- An International Journal, Volume 16, 611-629.

Bray, D. E., & Stanley, R. K. (1996), "Nondestructive Evaluation - A Tool in Design, Manufacturing, and Service", CRC Press, Boca Raton, USA.

Bulavinov, A. (2008), " Sampling phased array: a new technique for signal processing and ultrasonic imaging", Proceedings of the SPIE, Volume 6531, San Diego, USA.

Bulavinov, A., Hanke, R., Hegemann, J., Kroening, M., Reddy, K. M., Pudovikov, S., & Sridaran Venkat, R. (2008), "Application of Sampling Phased ArrayTechnique for Ultrasonic Inspection of CFRP Components", 1st International Symposium on NDT in Aerospace, Fürth, Germany.

Bulavinov, A., Joneit, D., Kosov, S., Kröning, M., Pinchuk, R., Pudovikov, S., Zhantlessov, Y. (2008), "Die getaktete Gruppenstrahlertechnik und ihre Anwendungen", DGZFP Proceedings on Moderne Systemtechnik bei Prüfungen mit Ultraschall, Wuppertal, Germany.

Bulavinov, A., Pinchuk, R., Reddy, K., & Walte, F. (2010), "Industrial application of real-time 3D imaging by sampling phased array", Proceedings on 10th European Conference on NDT, Moscow, Russia.

Cantrell, J. H., & Yost, W. T. (2001), "Nonlinear ultrasonic characterization of fatigue microstructures", International Journal of Fatigue, Volume 23, 487-490.

Chinta, P. K., Mayer, P., & Langenberg, K. (2012), "Three dimensional elastic wave modeling in austenitic steel welds using Elastodynamic Finite Integration Technique (EFIT)", 18th World conference on Nondestructive testing, Durban, South Africa.

CIVA, EXTENDE. (2015), "CIVA-2015 User manual for NDE simulation tool", CEA LIST, France.

COMSOL-Multiphysics. (2016), "User Manual of COMSOL Multiphysics", COMSOL Multiphysics GmbH, Göttingen, Germany.

Connolly, G. D., Lowe, M. J., Rokhlin, S. I., & Temple, J. A. (2008), "Use of Fermat's principle to aid the interpretation of the ultrasonic inspection of anisotropic welds", AIP Conference Proceedings., Volume 975 (1), 1018-1025.

Croxford, A. J., Moll, J., Wilcox, P. D., & Michaels, J. E. (2010), "Efficient temperature compensation strategies for guided wave structural health monitoring", Ultrasonics, Volume 50 (4), 517-528.

Deydier, S., Leymarie, N., & and Calmon, P. (2005), "Modeling of the ultrasonic propagation into carbon-fiber-reinforced epoxy composites, using a ray theory based homogenization method", In: Thompson, D. O and Chimenti, D. E (Eds), Review of Progress in QNDE, AIP Conference ProceedingsVolume 820, 972-978.

Doctor, S. R. (1986), "SAFT-The evolution of a signal processing technology for ultrasonic testing", NDT & Interntional, Volume 19 (3), 163-167.

Drinkwater, B. W., & Wilcox, P. (2006), "Ultrasonic arrays for non-destructive evaluation : A review", NDT & E International, Volume 39, 525-542.

Fendzi, C., Morel, J., Rebillat, M., Guskov, M., Mechbal, N., & Coffignal, G. (2014), " Optimal sensor placement to enhance damage detection in composite plates", 7th European Workshop on Structural Health Monitoring (EWSHM 2014), France.

Fitch, P. J. (1988), "Synthetic Aperture Radar", Springer-Verlag, New York.

Fritzen, C.-P. (1998), "Damage detection based on model updating methods", Mechanical Systems and Signal Processing", Volume 12, 163-186.

Fritzen, C.-P. (2005), Vibrational-based structural health monitoring - concepts and applications, "Key Engineering Materials", Volume 293-294, 3-20.

Fritzen, C.-P. (2005(a)), "Recent developments in vibrational-based structural health monitoring", 5th International Workshop on Structural Health Monitoring (IWSHM), Stanford University, DEStech Publications, Inc., USA.

Frouin, J., Matikas, T. E., Na, J. K., & Sathish, S. (1999), "In situ monitoring of acoustic linear and nonlinear behaviour of titanium alloys during cyclic loading", Proceedings of the SPIE, Volume 3585, 107-116.

Gao, H. (2007), " Ultrasonic Guided wave Mechanics For Composite Materials Structural Health Monitoring", Doctoral Thesis, Pennsylvania State University, Pennsylvania, USA.

Ghose, B., & Balasubramaniam, K. (2011), "COMSOL based 2D FEM model for ultrasonic guided wave propagation in symmetrically delaminated unidirectional multilayered composite structures", Proceedings of the National Seminar and Exhibition on Nondestructive Evaluation (NDE 2011), India.

Giurgiutiu, V. (2014), "Structural Health Monitoring with Piezoelectric Wafer Active Sensors- 2nd Edition", Academic Press, New York, USA.

Giurgiutiu, V. (2015), "Structural Health Monitoring of Aerospace Composites", Academic Press, New York, USA.

Goldman, M. F. (2002), "General Aviation Maintenance- Related Accidents: A Review of 10 years of NTSB Data", Civil Aerospace Medical Institute, Federal Aviation Administration, Oklahoma, USA.

Gopalakrishnan, S. (2011), "Computational Techniques in SHM", Springer-Verlag, London.

Gopalakrishnan, S., Chakraborty, A., & Mahapatra Roy, D. (2008), "Spectral Finite Element Method - Wave Propagation, Diagnostics and Control in Anisotropic and Inhomogeneous Structures", Springer-Verlag, London.

Grandt, A. F. (2003), "Fundamentals of Structural Integrity- Damage Tolerant Design and Non-destructive Evaluation", Wiley-Interscience, New Jersey, USA.

Gresil, M., & Giurgiutiu, V. (2013), "Time domain hybrid global-local concept for guided wave propagation with piezoelectric wafer active sensor", Journal of Intelligent Material Systems and Structures, Volume 24 (15), 1897-1911.

Guechaichia, A. T. (2011), "A simple method for enhanced vibration-based structural health monitoring", In Journal of Physics: Conference Series, Volume 305, 1-10.

Harris, B. (2003), "Fatigue in Composites", CRC Press LLC, Boca Raton, USA.

Helbig, K. (1994), "Foundations of Anisotropy for exploration seismics", Pergamon Press, Oxford, U.K.

Helfen, T. B. (2014), "Nichtlinearer Ultraschall zur Charakterisierung von Ermüdungsschäden während der Hochfrequenz-Beanspruchung von C-Faser Kunststoffverbunden", Doctoral Thesis, Saarland University, Saarbrücken, Germany.

Jhang, K. Y. (2009), "Nonlinear ultrasonic techniques for non-destructive assessment of micro damage in material: A review", International Journal of Precision Engineering and Manufacturing, Volume 10 (1), 123-135.

Kalyanasundaram, P., & Baldev Raj, V. B. (2011), "Practical Digital Signal Processing", Alpha Science International, Oxford, U.K.

Kappatos, V., Asfis, G., Salonitis, K., Zitzilonis, V., Avdelidis, N. P., Cheilakou, E., & Theodorakeas, P. (2017), "Theoretical assessment of different ultrasonic configurations for delamination defects detection in composite components", 5th International Conference on Through-Life Engineering Services- Procedia CIRP, Volume 59, 29-34.

Kim, H.-J., Song, S.-J., & Kang, S.-S. (2011), "Model-based simulation of focused beam fields produced by phased array ultrasonic transducer in dissimilar metal welds", NDT & E International, Volume 44, 290-296.

Kline, R. A. (1992), "Nondestructive Characterization of Composite Media", Technomic Publishing Company.

Kolkoori, S. R., Rahman, M. U., Chinta, P. K., Kreutzbruck, M., Rethmeier, M., & Prager, J. (2013), "Ultrasonic field profile evaluation in acoustically inhomogeneous anisotropic materials using 2D ray tracing model: Numerical and experimental comparison", Ultrasonics, Volume 53 (2), 396-411.

Kolkoori, S., Hoehne, C., Prager, J., l Rethmeier, M., & Kreutzbruck, M. (2014), "Quantitative evaluation of ultrasonic C-scan image in acoustically homogeneous and layered anisotropic materials using three dimensional ray tracing method", Ultrasonics, Volume 54, 551-562.

Kramer, S. (1989), "Ultrasonic weld defect sizing using the Synthetic Aperture Focusing Technique", In: Thompson, D. O and Chimenti, D. E (Eds), Review of Progress in QNDE, Volume 8, 1995-2002, Springer, Boston, USA.

Kriz, R. D., & Liu, W. L. (2007), "Simulation of visualization of energy waves propagating in 2D-3D anisotropic media", www.sv.rkriz.net (last visited February 2019).

Lee, B. C., & Staszweski, W. J. (2007), "Sensor location studies for damage detection with Lamb waves", Smart Materials and Structures, Volume 16, 399-408.

Li, C., Pain, D., Wilcox, P. D., & Drinkwater, B. W. (2013), "Imaging composite materials using ultrasonic arrays", NDT & E International, Volume 53, 8-17.

Malinowski, P., Wandowski, T., & Ostachowicz, W. (2012), "Investigation of sensor placement in Lamb wave based SHM method", Key Engineering Materials, Volume 518, 174-183.

Mallardo, V., Aliabadi, M. H., & Sharif Khodaei, Z. (2012), "Optimal sensor positioning for impact localization in smart composite panels", Journal of Intelligent Material Systems and Structures, Volume 24 (5), 559-573.

MATLAB-User-manual. (2015), "Short Time Fourier Transformation (STFT) with MATLAB implementation", MathWorks Inc., USA.

Meo, M., & Zumpano, G. (2005), "Nonlinear elastic wave spectroscopy identification of impact damage on a sandwich plate", Composite Structures, Volume 71, 302-306.

Nayfeh, A. H. (1995), "Wave Propagation in Layered Anisotropic Media with Applications to Composites", North Holland Publishing Company, Amsterdam, Netherlands.

Nieuwenhuis, J. H., Neumann, J., Greve, D. W., & Oppenheim, I. J. (2005), "Generation and detection of guided waves using PZT wafer transducers", IEEE Transactions Ultrasonics, Ferroelectrics and Frequency Control, Volume 52 (11), 2103-2111.

Ogilvy, J. A. (1986), "Ultrasonic beam profiles and beam propagation in an austenitic weld using a theoretical ray tracing model", Ultrasonics, Volume 24, 337-347.

Onishi, M. (2012),"Toray's business strategy for carbon fibre composite materials-Report", Report retrieved from the website, www.toray.com (last visited February 2019).

Ooijevaar, T. (2014), "Vibration based structural health monitoring of composite skin-stiffener structures", Doctoral Thesis, Twente University, Netherlands.

Ostochowicz, W., Kudela, P., Krawczuk, M., & Zak, A. (2012), "Guided waves in Structures for SHM: The Time-Domain Spectral Element Method", John Wiley & Sons, Ltd, Chichester, U.K.

Papadakis, P. (1986), "Ultrasonic Instruments and Devices", Academic Press, New York, USA.

Postma, G. (1955), "Wave propagation in a stratified medium", Geophysics, Volume 20 (4), 780-806.

Pudovikov, S. (2013), "Optimierung und Nachweis der Ultraschallprüfbarkeit von akustisch anisotropen Werkstoffen an austenitischen Schweiß- und Mischwerkstoffen", Doctoral Thesis, Saarland University , Saarbrücken, Germany.

Qiu, L., Sridaran Venkat, R., Boller, C., & Yuan, S. (2016), "Multiphysics simulation of guided wave propagation under load condition", 8th International Symposium on NDT in Aerospace, Bengaluru, India.

Rabe, U., Helfen, T. B., Weikert, M., Hirsekorn, S., Herrmann, H. J., Boller, C.,Eifler, D. (2012), "Nonlinear ultrasonic testing of carbon fibre reinforced plastics in the very high cycle fatigue regime", 17th International Conference on Nonlinear Elasticity in Materials, In: Proceedings of Meetings on Acoustics, Acoustical Society of America, Volume 16, 1-6.

Raghavan, A. (2007), "Guided Wave Structural Health Monitoring", Doctoral Thesis, University of Michigan, Ann Arbor, Michigan, USA.

Rathod, V. T., & Roy, D. M. (2011),"Ultrasonic Lamb wave based monitoring of corrosion type of damage in plate using a circular array of piezoelectric transducers", NDT & E International, Volume 44 (7), 628-636.

Rathod, V. T., Jeayseelan, A., Dutta, S., & Mahapatra, R. (2017), "Ultrasonic guided wave sensing characteristics of large area thin piezo coating", Smart Materials and Structures, Volume 26 (10), 1-30.

Rojas G, J. (2011), "Microstructural characterization and viscoelastic properties of AlZnMg and AlCuMg alloys", Doctoral Thesis, Polytechnic university of Catalonia, Barcelona, Spain.

Rokhlin, S. I., & Wang, L. (2002), "Ultrasonic waves in layered anisotropic media: characterization of multidirectional composites", International Journal of Solids and Structures, Volume 39, 4133-4149.

Rokhlin, S. I., Chimenti, D., & Nagy, P. B. (2011), "Physical Ultrasonics of Composites", Oxford University Press, New York, USA.

Rose, J. L. (2004), "Ultrasonic Waves in Solid Media", Cambridge University Press , New York, USA.

Rose, J. L. (2014), "Ultrasonic Guided Waves in Solid Media", Cambridge University Press, New York, USA.

Sadri, M., & Riahi, M. A. (2010), "Raytracing and amplitude calculation in anisotropic layered media", Geophysical Journal International, Volume 180 (3), 1170-1180.

Salah, L., & Tomblin, J. (2010), "Aging effects evaluation of a decommisioned Boeing CFRP 737-200 horizontal stabilizer (Phase II)", Proceedings on FAA Aging Aircraft Conference, Federal Aviation Administration, Universal Tech Corporation, Dayton, USA.

Schmitz, V., & Walte, F. (1999), "3D ray tracing in austenite materials", NDT & E International, Volume 32 (4), 201-213.

Schmitz, V., Müller, W., & Schäfer, G. (1992), "Synthetic Aperture Focusing Technique-state of the art", Journal of Acoustical Imaging, Volume 19, 545-551.

Seydel, J. (1982), "Ultrasonic Synthetic Aperture Focusing Techniques in NDT", In Research Techniques in Non-destructive Testing, Edited by Sharpe, R. S., Volume 6, 1-47, Academic Press, London, UK.

Sharif Khodaei, Z. (2016), "An optimization strategy for best sensor placement for damage detection and localization in complex composite structures", 8th European Workshop On Structural Health Monitoring (EWSHM), Bilbao, Spain.

Sheehan, J. D. (2016), "Notes on Finite Element Modeling", Dublin Institute for Advanced Studies, https://homepages.dias.ie (last visited 26/02/2019).

Shen, Y. (2013), "Predictive modeling of Nonlinear wave propagation for structural health monitoring with piezoelectric wafer active sensors", Journal of Intelligent Materials and Smart Structures, Volume 25 (4), 506-520.

Shen, Y., & Giurgiutiu, V. (2014), "WaveformRevealer- An Analytical framework and predictive tool for the simulation of multimodal guided wave propagation and interaction with damage", Structural Health Monitoring - An International Journal, Volume 13 (5), 491-511.

Shen, Y., & Giurgiutiu, V. (2015), "WFR-2D: An Analytical model for PWAS generated 2D ultrasonic guided wave propagation", Proceedings of the SPIE, Volume 9064, DOI: 10.1117/12.2044798.

Shi, Z. Y., Law, S. S., & Zhang, L. M. (2000), "Optimum sensor placement for damage detection", Journal of Engineering Mechanics, Volume 126 (11), 1173-1179.

Shull, P. J. (2002), "Nondestructive Evaluation-Theory, Techniques and Applications", Marcel Dekker Inc., New York, USA.

Slawinski, M. A. (1996), "On elastic wave propagation in anisotropic media :Reflection / Refraction Laws, raytracing and traveltime Inversion", Doctoral Thesis, University of Calgary, Alberta, Canada.

Solodov, I. Y., Krohn, N., & Busse, G. (2002), "CAN: an example of nonclassical nonlinearity in solids", Ultrasonics, Volume 40, 621-625.

Spies, M. (2004), "Analytical methods for modeling of ultrasonic nondestructive testing of anisotropic media", Ultrasonics, Volume 42, 213-219.

Spies, M., & Jager, W. (2003), "Synthetic Aperture Focusing for defect reconstruction in anisotropic media", Ultrasonics, Volume 41, 125-131.

Sridaran Venkat, R., Boller, C., & Bulavinov, A. (2009), "Mountain bike frames as an example for structural health monitoring and additional challenges with composite materials", Proceedings on "Fahrrad Workshop" conducted by D.V.M, Berlin, Germany.

Sridaran Venkat, R., Boller, C., Ravi, N. B., Mahapatra, D. R., & Steckel, M. (2015), "Establishing a simulation platform for acoustics based SHM system configuration", 7th International Symposium on NDT in Aerospace, Bremen, Germany.

Sridaran Venkat, R., Bulavinov, A., Pudovikov, S., & Boller, C. (2010), "Quantitative non-destructive evaluation of CFRP components by Sampling Phased Array", 2nd International Symposium on NDT in Aerospace , Hamburg, Germany.

Sridaran Venkat, R., Starke, P., & Boller, C. (2018), "Acoustics Based Assessment of a Composite Material Under Very High Cycle Fatigue Loading", In: Fatigue of Materials at Very High Numbers of Loading Cycles: Experimental Techniques, Mechanisms, Modeling and Fatigue Life Assessment, Edited by Christ, H, J., 463-485, Springer-Verlag, Berlin.

Srivatsava, A. (2010), "Quantitative structural health monitoring by ultrasonic guided waves", Journal of Engineering Mechanics, Volume 136 (8), 937-944.

Staszewski, W., & Worden, K. (2003) , "An overview of optimal sensor location methods for damage detection", Proceedings of the SPIE, Volume 4326, 179-187.

Stepinski, T., Uhl, T., & Staszewski, W. (2013), "Advanced Structural Damage Detection: From Theory to Engineering Applications", John Wiley & Sons, Chichester, U.K.

Stopin, A. (2000), "Bending, ray tracing and reflection tomography for T.I medium", 9th International Workshop on Seismic Anisotropy, Volume 66 (4), Texas Geosciences, The University of Texas and Austin, Texas, USA.

Su, Z., & Ye, L. (2009), "Identification of Damage Using Lamb waves: From Fundamentals to Applications", Springer-Verlag, London.

Talreja, R., & Duke, J. C. (1988), "Application of Acousto-Ultrasonics to Quality Control and Damage Assessment of Composites", In Acousto-Ultrasonics: Theory and Applications, Edited by Duke, J. C.,177-190, Springer Science, New York.

Taltavull, A., Sridaran Venkat, R., Boller, C., & Dürager, C. (2017), "Simulation, realization and validation of guided wave SHM system solutions for aircraft metallic structural repairs", 11th International Workshop on SHM (IWSHM), Stanford University, DEStech Publications, Inc., USA.

Tomblin, J., & Salah, L. (2010), "Aging effects evaluation of a beechcraft starship main wing", 6th Annual Technical Review Meeting of FAA Joint Advanced Materials & Structures (JAMS) Center of Excellence, New Jersey, USA.

Wandowski, T., Malinowski, P. H., & Ostachowicz, W. (2016), "Circular sensing networks for guided waves based structural health monitoring", Journal on Mechanical Systems and Signal Processing, Volume 66-67, 248-267.

www.skybrary.aero,"Ageing aircraft structural failure", www.skybrary.aero (last visited on February 2019).

Zepeda Nunez, L. (2017) , "Time-stepping beyond CFL- a locally one-dimensional scheme for acoustic wave propagation", www.math.mit.edu (last visited 26/02/2019), Department of Mathematics and Earth Source Lab, Massachusetts Institute of Technology, USA.